A FINAL REPORT
For the Period
23 December 1965 to 17 February 1967


√ BEHAVIOR OF VARIOUS ADSORBATES
ON METAL SUBSTRATES


by

C. J. Bennette
R. W. Strayer
L. W. Swanson
E. C. Cooper


prepared for


NATIONAL AERONAUTICS AND SPACE ADMINISTRATION

Lewis Research Center


25 April 1967


CONTRACT NAS3-8900

Technical Management
NASA Lewis Research Center
Cleveland, Ohio
Electric Propulsion Office
John Ferrante


FIELD EMISSION CORPORATION
Melrose Avenue at Linke Street
McMinnville, Oregon

# TABLE OF CONTENTS

TABLE OF CONTENTS

TABLE OF CONTENTS (Cont'd)

LIST OF ILLUSTRATIONS

LIST OF ILLUSTRATIONS (Cont'd)

## LIST OF ILLUSTRATIONS (Cont'd)

LIST OF TABLES

# INTRODUCTION

## OBJECTIVES AND DESCRIPTION OF WORK

This report describes work performed at Field Emission Corporation under the sponsorship of the Electric Propulsion Office of Lewis Research Center, National Aeronautics and Space Administration. The general objective of the work was to apply field emission and retarding potential techniques to certain physical phenomena occurring on bombardment thruster electrodes and cathode surfaces, so that an improved design of the thruster could be obtained. The work was divided into three general areas: (1) field emission and retarding potential studies of the work function changes and surface kinetics of cesium and oxygen adsorbates on selected non-refractory metals and of the activation, poisoning and sputtering phenomena for oxide cathodes; (2) field ion and field emission microscope investigations of noble gas and cesium ion sputtering of refractory metals; and (3) field emission investigation of the interaction of low energy electrons with cesium or mercury adsorbates on clean and oxygen-covered tungsten.

## SUMMARY OF RESULTS

Some of the problems listed above have been studied under previous contracts and the results reported in the final reports for contracts NASr-19, NASw-458, NAS3-2596, and NAS3-5902. The latter two reports also appear under NASA CR-54106 and NASA CR-54704. The results obtained under the present contract are listed below.

### Cs Adsorbed on Clean and Oxygenated Metal Substrates

Field emission microscope (FEM) and thermionic retarding potential triode (RPT) techniques were used to obtain the work function versus coverage characteristics of Cs on the following metal substrates: the (110) plane of W; the (221) plane of Al; the $(10\bar{1}0)$ plane of Ti; heavily oxygenated W;

and clean Ni. The resulting curves for all of these systems have similar shapes; the principal difference is that the maximum work function change due to $C_s$ adsorption is less for Al and Ti than for the other metals.

The average work function minimum is higher for $C_s$ on a heavily oxygen-covered W field emitter than it is when the underlying oxygen coverage is lower. ( $\phi_m$ = 1.41 eV for $\phi_{OW}$ = 6.40 eV while $\phi_m$ = 1.10 eV for $\phi_{OW}$ = 5.16 eV). A curve of $\phi_m$ as a function of underlying oxygen coverage goes through a minimum when the average work function of the underlying OW surface is about 5.1 eV. The average work function for clean W is 4.52 eV.

A very brief look at the characteristics of Hg adsorption on an OW surface showed that the adsorption of Hg on a surface in which $\phi_{OW}$ = 5.2 eV resulted in an average work function maximum which is slightly lower than the 4.9 eV maximum for Hg on clean W and a minimum of 4.3 eV, which is lower than for Hg on clean W.

Desorption energies for $C_s$ neutrals from Ni and Ti ($10\bar{1}0$) and for $C_s$ ions from Ni were measured. The $C_s$-Ni work was performed at very low coverage and a plot of desorption energy as a function of coverage could be extrapolated to give the zero coverage values for both neutrals $E_a^o$ and ions $E_p^o$.

The significant experimental results obtained under this contract for $C_s$ adsorbed on various clean and oxygenated substrates are listed in Table I.

TABLE I

Summary of Significant Experimental Results

| System | $\phi$ (eV) substrate | $\Delta\phi_m$ (eV) | $\phi_m$ (eV) | $E_a^o$ (eV) | $E_p^o$ (eV) | $T_d$ (°K) (desorption) | Method |
|---|---|---|---|---|---|---|---|
| $C_s$-OW | 6.40 | 4.99 | 1.41 | | | | FEM |
| $C_s$-Ni | | 3.66 | 1.37 | 3.30 | 2.40 | 1011 | FEM |
| $C_s$-W(110) | | 3.34 | | | | | RPT |
| $C_s$-Al | | 3.15 | | | | 870 | RPT |
| $C_s$-Ti($10\bar{1}0$) | 4.42 | 2.92 | | 2.20 | | 865 | RPT |
| Hg-OW | 5.20 | .990 | 4.30 | | | 300 | FEM |

## Oxide Cathode Studies

The effect of $O_2$ and $H_2$ on the emission characteristics of Ni based BaO surfaces was studied. Maximum emission obtained was 300 $mA/cm^2$, the limitation being due to space charge and the circuitry of the experiment, but not due to the cathode itself. Emission could be restored by heating following $O_2$ poisoning, therefore no significant irreversible chemical changes take place.

The ion sputtering of the oxide cathode was also studied. Emission dropped as a result of $He^+$ bombardment and was only partially restored by heating, indicating that sputtering caused permanent damage, probably partial removal of the oxide coating.

## Electron Desorption Studies

Using FEM techniques and analyzing work function changes, cross-sections were obtained for the desorption of oxygen from W at three different electron energies. The results are as follows: $6.34 \times 10^{-20}$ $cm^2$ at 250 volts; $9.1 \times 10^{-20}$ $cm^2$ at 200 volts; and $3.1 \times 10^{-19}$ $cm^2$ at 100 volts. The maximum value of cross-section for removal of the loosely bound O state showed a maximum at 100 volts.

Cross-sections were determined for the desorption of Cs by 250 volt electrons on five different underlying oxygen coverages corresponding to work functions of $5.38 \pm .01$, $5.53 \pm .02$, $6.03 \pm .03$, $6.42 \pm .02$, and $6.50 \pm .04$ eV. The impingement of low energy electrons on this composite surface causes cesium to be removed without disturbing the underlying O layer. Cross-sections are negligible at low Cs coverages, regardless of underlying O coverage, increasing with Cs coverage to $8 \times 10^{-20} cm^2$.

Electron induced desorption of Hg on W and on OW at $77^\circ K$ was studied with 250 volt electrons over the entire coverage range of Hg. The results showed that no electron induced desorption or rearrangement of the Hg layer occurred. Cross-sections for electron induced desorption of Hg by 250 volt electrons must be less than the sensitivity limit of these experiments, which

3

was less than $1 \times 10^{-20} cm^2$.

## Sputtering Studies

Sputtering of clean W by He ions has been investigated by field ion microscopy for ion energies between 500 and 4000 eV and for ion densities up to $3.5 \times 10^{14}$ ions/$cm^2$. The number of sputtering events (displaced or missing atoms) increased with increasing ion energy or density. Most of the sputtering events occurred on the beam-incident side of the target for all He ion energies investigated; a few events were also found on the opposite side of the target. For 1000 eV bombardment, the density of sputtering events varied only about a factor of two over the various crystallographic regions of the target; these regions ranked in order of decreasing sputtering event density in the following order: $\{100\}$, $\{211\}$, $\{111\}$, $\{110\}$. The depth of damage increased with increasing ion energy. Ion image sequences at constant energy indicate that the sputtering process is in some cases a multistep process.

Sputtering of clean W by Cs ions has been studied by FEM techniques for ion energies between 100 and 3800 eV and for ion densities up to $7 \times 10^{14}$ ions/$cm^2$. The amount of roughening caused by ion bombardment increased with Cs ion density and with increasing ion energy. The amount of surface damage obtained under these conditions was completely removed by heating the target to $800^{\circ}$K. The amount of roughening decreased with increasing target temperature, due to annealing of the target at elevated temperatures.

## PAPERS AND MEETINGS

The following papers covering portions of work performed under past and present contracts are in various stages of publication:

" Electrical Breakdown between Metal Electrodes in High Vacuum. I.
Theory", by Francis M. Charbonnier, Carol J. Bennette, and
Lyn Swanson, Journal of Applied Physics 38, 627 (1967).

" Electrical Breakdown between Metal Electrodes in High Vacuum. II.
Experimental", by Carol J. Bennette, Lyn W. Swanson, Francis M.
Charbonnier, Journal of Applied Physics 38, 634 (1967).

"Desorption, Mobility and Work Function Change of Hg on W and Mo Substrates", by L. W. Swanson, R. W. Strayer and L. Davis (to be published).

"Field Electron Microscopy Studies of Cesium Layers on Various Refractory Metals:  Work Function Change", by L. W. Swanson and R. W. Strayer (to be published).

Papers were also presented at the following professional meeting:

Second International Symposium on Insulation of High Voltages in Vacuum, Massachusetts Institute of Technology, Cambridge, Mass., 7-8 Sept. 1966.

## CESIUM ADSORBED ON VARIOUS METAL SUBSTRATES

An understanding of the basic mechanisms involved in the adsorption and desorption of Cs on both clean and oxygenated metal surfaces is essential to the development of long-life, stable Cs ion propulsion systems.  In addition, the information gained from studying Cs adsorption extends our general knowledge of the physical processes associated with surface binding.  Earlier experimental work performed here[1-4] was concerned with the behavior of Cs on the refractory metals, tungsten, molybdenum, and rhenium.  During the past year a broader range of substrates have been studied, including non-refractory metals and metals with different crystal structures.

Titanium was chosen as a substrate for adsorption studies for several reasons, among which are its gettering properties and its change in crystalline structure from a hcp at low temperatures to bcc above $1150^{\circ}K$[5]. These properties make it a difficult material from which to obtain a clean surface whose crystal orientation is well-defined.

The metal crystals used in previous work were either bcc (W and Mo) or hcp (Re). To extend our knowledge of surface binding, it is interesting to examine the influence, if any, of the substrate crystal structure. Although it is very difficult to obtain a clean Al surface, the fcc Al crystal was chosen because of its widespread practical importance. Ni is also an appropriate metal to choose. It also exhibits a fcc crystal structure; its lattice constant is similar to that of W; it has a relatively high average work function; and clean, well-defined surfaces may be obtained by standard techniques.

## METHOD OF APPROACH

The measurements of interest are the changes in work function $\Delta\phi$ with Cs coverage $\sigma$ and the binding energy of Cs on various substrates. Both of these measurements can be made using one of two approaches. The first approach allows measurements to be made under conditions of equilibrium Cs pressure; the second allows kinetic measurements to be made at zero pressure. To obtain $\Delta\phi$ vs $\sigma$ data in an equilibrium Cs pressure, the substrate is flashed clean of Cs, quenched rapidly to a known temperature, and $\Delta\phi$ is measured as a function of time. Assuming unity sticking coefficient, the time scale can be readily converted to absolute or relative coverage.

The first approach also allows one to determine the binding energy of Cs on various substrates from measurements of equilibrium heats of adsorption obtained from coverage versus temperature data at various equilibrium pressures. The Clausius-Clapeyron equation at constant coverage may be used in the form

$$\frac{d\,(\ln P)}{d\,(1/T)} = -\frac{H}{k} \tag{1}$$

where H is the isoteric heat of adsorption and P the equilibrium pressure. One can readily observe that, since the kinetic impingement rate $\mu_P$ is proportional to P, the slope of a plot of log $\mu_P$ versus $1/T$ yields the adsorption energy H at a constant value of $\sigma$. It should be pointed out that Equation (1) is strictly true in the thermodynamic sense when the gas and substrate are isothermal.

This was not the case in our work, except at low substrate temperatures; therefore, it is more appropriate to view the system from steady state rather than thermodynamic equilibrium considerations. Letting the desorption rate

$$- \frac{d}{dt} = \nu \, \sigma \, \exp \left( - E_a / kT \right) \qquad (2)$$

and the kinetic impingement rate

$$\mu_P = \frac{a_s \, P}{\sqrt{2\pi MkT}} \qquad (3)$$

equal each other, where $a_s$ is the sticking coefficient and $E_a$ is the activation energy of desorption, k is Boltzmann's constant, and M is the particle mass:

$$\ln P = \ln \left[ \nu \, \sigma \, (2\pi \, Mk \, T)^{1/2} \Big/ a_s \right] - E_a / kT. \qquad (4)$$

Implicit in the derivation of Equation (4) is the assumption of zero activation energy for adsorption. This seems reasonable in view of Langmuir's [6] contention that $a_s$ equal one throughout the monolayer coverage range. If we ignore the variation with temperature of the first term on the right side of Equation (4) in comparison with the second, we obtain the approximate expression (within 2% at 1000° K):

$$\left[ \frac{d \, (\ln P)}{d \, (1/T)} \right]_\sigma \cong - E_a / k \qquad (5)$$

Since $E_a$ is equal to H for zero activation energy of adsorption, it is readily observed that the slope of ln P versus 1/T at constant $\sigma$ also gives, within the above approximations, the value of H for steady state conditions.

The second approach allows kinetic activation energies to be measured by monitoring changes in $C_S$ coverage with time in zero pressure conditions. One can integrate Equation (2) over a coverage increment $\sigma_i$ to $\sigma_f$ to yield

$$\ln t = \ln \left[ \ln \left( \sigma_i / \sigma_P \right) \right] - \ln \nu + E_a / kT \qquad (6)$$

7

where $\sigma_i$ is the coverage at $t = 0$ and $\sigma_f$ is the coverage at a later time t. At zero final coverage $\sigma_f = 0$, $\Delta \sigma \sim \sigma$ and Equation (6) does not apply. However, for this case, $\Delta \sigma/\sigma \sim 1$ and $\Delta t \sim t$ respectively, the differential expression, Equation (2) leads directly to the working equation for the case of zero final coverage;

$$\ln t = -\ln \mathcal{V} + E_a'/kT \tag{7}$$

By measuring the time it takes to desorb a particular coverage interval at various temperatures, and plotting the results in the form log t vs 1/T, the value of $E_a$ at a constant coverage can be obtained from the slope of the resulting straight line.

The zero pressure approach can also be used to obtain direct measurement of $\Delta \emptyset$ vs $\sigma$ by measuring work function changes associated with successive deposits of known amounts of Cs on the surface.

Field emission microscopy has been used extensively in the study of surfaces. Measurements of the field emission current I as a function of applied voltage V enables one to obtain information about the adsorbate-coated surface through the Fowler-Nordheim equation for field emission, which can be written

$$I/V^2 = A \exp (2.3 \times 10^4 \, m/V) \tag{8}$$

Plotting the data in the form log $I/V^2$ vs $10^4/V$ results in a straight line of slope m which intercepts the vertical axis at log A when $10^4/V = 0$. From the Fowler-Nordheim law of field emission this slope is:

$$m = \frac{-2.83 \times 10^3 \, \emptyset^{3/2}}{\beta} \tag{9}$$

where $\beta$ is the geometrical ratio of the electric field F at the emitter surface and the applied voltage. Equation (9) can be used to determine either changes in work function or changes in surface geometry. When the work function of the clean surface $\emptyset_1$ is used as a reference, the work function of the coated surface can be determined from the slopes of the corresponding Fowler-Nordheim plots, assuming that $\beta$ remains constant:

$$\emptyset = \emptyset_1 \, (m/m_1)^{2/3} \tag{10}$$

Since $\beta$ is a function of electrode geometry only and depends mainly on emitter shape, changes in the geometry of a clean tip caused, for example, by sputtering, can be detected in terms of changes in $\beta$. However, field emission methods do not allow one to distinguish between work function changes and geometrical changes associated with rearrangement of the adsorbate.

Inasmuch as experimental measurements of work function and desorption energy derived their most fundamental meaning when performed on single crystal faces, we have used field emission probe methods in the past[1-3] for such measurements. A disadvantage of this approach is that the small hemispherical point of the emitter exposes a variety of crystal faces so that coverage anisotropies occur under conditions of mobile adsorption, due to preferential binding of cesium on certain crystal faces. Also, some substrates of interest such as aluminum are difficult to fabricate into emitters that are amenable to cleaning.

To circumvent the above mentioned problems, a thermionic retarding potential[7] method (RPT) was used in which the electrodes were single crystal disks. This technique has been discussed in detail in a previous report[3]; therefore, only a brief discussion of the method will be presented. The embodiment consists of two single crystal disks, a thermionic emitter with uniform work function and a collector with a work function $\emptyset$ parallel to one another and to a central apertured disk. The electron beam is confined in a magnetic field to a small, definable area of the collector crystal.

One can readily show a relationship between collector current density $J_c$ and temperature for this triode of the following form:

$$J_c = CT^2 \exp\left[(V_b - \emptyset_c)/kT\right] = J_e \exp\left[(\emptyset_e - \emptyset_c + V_b)/kT\right] \tag{11}$$

where C is a constant theoretically equal to 120 A/cm$^2$deg$^2$, $J_e$ is the emitter current density and $\emptyset_e$ and $\emptyset_c$ are the emitter and collector work functions

respectively. At a constant emitter to collector bias voltage $V_b$ (where $V_b$ is the positive voltage on the emitter) Equation (11) shows that a plot of log $J_c/T^2$ vs $1/T$ at constant $V_b$ yields the value of $\phi_c$, provided that $V_b < (\phi_e - \phi_c)$. Also plots of log $J_{cc}$ versus $V_b$ at constant T yield straight lines, such as those shown in Figure 1, of slope $1/kT$, which form a "knee" at $V_b = (\phi_c - \phi_e)$. Thus the absolute work function of the collector can be determined as well as the contact potential. The latter is determined from the position of the knee on the voltage scale. Changes in work function of the collector due to adsorption or desorption of Cs are easily monitored as changes in $V_b$ at a constant $J_c$ where $V_b < (\phi_e - \phi_c)$.

To summarize, two approaches and two experimental techniques are employed to obtain measurements of the binding energies of Cs to various metal substrates and to monitor changes of work function with Cs coverage. The kinetic approach in which measurements are made under zero pressure conditions was a more successful approach than the equilibrium approach in which measurements are made under equilibrium pressure conditions. The latter approach was not entirely successful due to artifacts of our particular experimental arrangement, rather than to any basic difficulty associated with this technique.

The retarding potential triode (RPT) offers certain advantages where the field emission microscope (FEM) is impracticable. First, the RPT allows measurements to be made under equilibrium pressure conditions. Second, it is possible to obtain absolute work functions of the various substrates with the RPT. Finally, and perhaps most significant, by using magnetic confinement of the electron beam in the RPT, one can sample a small (compared to crystal dimensions), definable area of a macroscopic crystal surface. This eliminates edge effects and ensures that the contact potentials so obtained are associated with only a single crystal face.
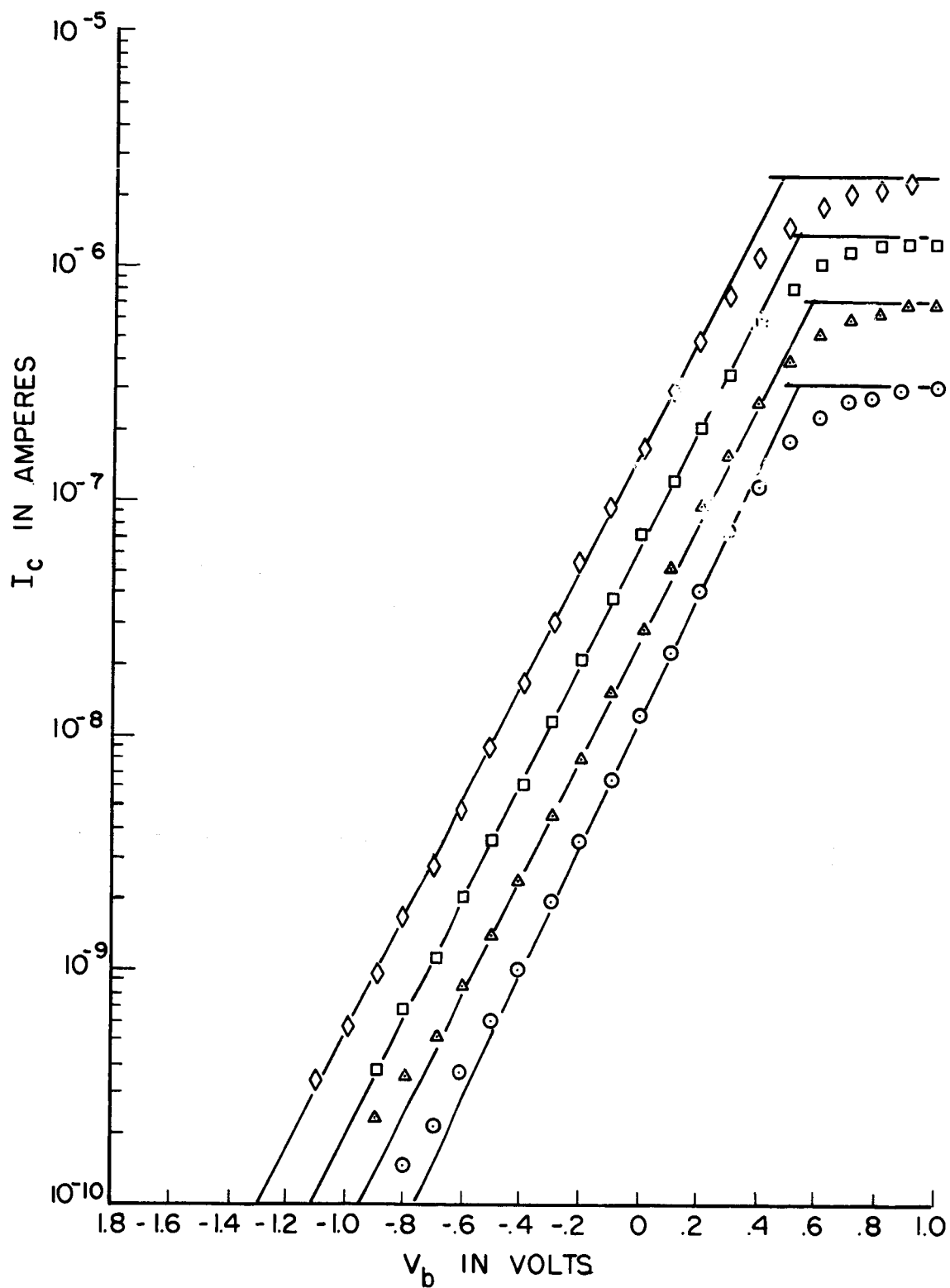
Figure 1.   Typical plots of collected current versus bias voltage for
clean W(110) at four temperatures.  The temperature is
obtained from the slope of the semilogarithmic portion
of the curve.

11

## EXPERIMENTAL PROCEDURES

Five different systems were studied in this work, including three single crystal RPT studies of Cs on W(110), Al(221), and Ti(10$\bar{1}$0), and two FEM studies of Cs on Ni and on oxygenated W.

### Field Emission Microscopy

The FEM construction, discussed in detail elsewhere,[1] allowed the adsorbate, O and/or Cs, to be deposited at a controllable and measurable rate onto a field emitter made of the desired substrate. The temperatures of the emitter and of the source were accurately controlled by an electronic servo-circuit described elsewhere.[4] The oxygen source used for coadsorption studies consisted of "in situ" formed copper oxide contained inside a heatable platinum bucket. Resistively heating the bucket to 720$^{\circ}$K allowed pure oxygen to be liberated.

<u>Cesium on Nickel.</u> - The general procedure for cleaning field emission tips in the FEM has been to heat for short periods of time at successively higher temperatures. For example, heating a W field emitter for several seconds above 2200$^{\circ}$K will generally produce a clean surface. Applying this method to Ni emitters resulted in very dull tips that required excessive voltages ($\sim$ 20kV) to draw measurable emission current. Emitters were successfully cleaned by flashing to approximately 1500$^{\circ}$K for very short periods of time.

Work function vs coverage measurements were obtained in the FEM by the following previously discussed procedure:[1] 1) a Fowler-Nordheim plot was made of the clean surface I-V data; 2) a fixed amount of Cs (approximately 0.1 monolayer) was deposited onto the tip; 3) Cs was spread evenly across the emitter surface by heating the tip at a temperature $T_{eq}$ until a symmetrical field emission pattern was obtained and until further heating produced no further changes in emission current at a constant applied voltage; 4) a value of $\emptyset$ was obtained from the Fowler-Nordheim plot of the I-V

characteristics of the surface; 5) dose reproducibility was established by removing the Cs and repeating the above procedure several times; 6) deposition, equilibration, and determination of $\emptyset$ was repeated for a cumulation of success- ive doses until a total coverage of more than one monolayer was obtained.

Terminal neutral $E_a$ and ionic $E_p$ desorption energies were measured in a manner similar to that of Gomer and Schmidt.[8] Because of the variation of both neutral and ionic desorption energies with adsorbate coverage, measure- ments were confined to a small $\Delta\sigma$, thereby localizing the values of $E_a$ and $E_p$ to a given coverage or work function. The coverage increment over which the measurements were made corresponded to approximately 10 percent change in $\emptyset$, with the clean Ni surface used as the end point.

A heavy Cs dose was deposited at $77^\circ$K, spread by heating to $250^\circ$K, then desorbed by heating to the coverage chosen for the initial point of the desorption study. During neutral desorption a negative field of 3. 5 MV/cm was applied to prevent ions from leaving the tip. Similarly, a positive bias of 22. 5 volts at the tip kept ions from returning when ion desorption measurements were being made. The temperature range required for ion desorption was sufficiently below that required for neutral desorption (in similar coverage intervals) so that concomitant neutral desorption could be neglected. Periodically during the desorption the temperature was reduced to $77^\circ$K, and the voltage required to maintain a constant current was plotted as a function of time. In the coverage range of interest a voltage interval can be related directly to a coverage interval; therefore, this data was used to calculate desorption energies for several coverage intervals.

Cesium on Oxygen-Coated Tungsten. -Measurements of the work function vs coverage for Cs on OW have been reported previously[1,2] for underlying oxygen coverages $\sigma_{OW}$ corresponding to $\emptyset_{OW} \leq 5.65$ eV. The present work was done with underlying oxygen coverages corresponding to $\emptyset_{OW} > 6.0$ eV.

The clean tip was first covered with oxygen, then heated to $522^\circ$K, a temperature known to be higher than that required $T_{eq}$ to spread subsequent

13

$C_s$ doses, and a work function was recorded for $\emptyset_{OW}$. Heating above $T_{eq}$ makes unlikely any thermally induced rearrangement of the O layer. This does not, of course, preclude any chemically induced rearrangement of the O layer due to the presence of the $C_s$.

The $C_s$ dose size and reproducibility were established on the clean W substrate before oxygen was admitted onto the tip. The absolute amount of $C_s$ deposited onto the W tip could be determined from the known $\emptyset$ vs $\sigma$ relationship for $C_s$ on clean W. The $C_s$ dose was deposited unilaterally onto the O-covered tip, and heated at $T_{eq}$ to migrate $C_s$ across the tip. After each $C_s$ dose, the tip was cooled to $77^{O}K$ and the work function was determined. The procedure was the same as that reported above for Cs on Ni.

### Thermionic Retarding Potential Triode

Two different versions of the RPT were used. Figure 2 shows a diagram of the triode tube used for the Al and the W work, in which both the emitter and the collector were single crystal disks. This design featured a resistively-heated emitter, an accelerating electrode in the form of a disk with a .015 inch diameter, beam defining aperture, and magnetic confinement of the electron beam. This configuration permitted measurement of absolute work functions from data such as that shown in Figure 1, by the method described in an earlier section of this report. Unfortunately, the range of current densities $J_c$ was too limited to provide accurate values of emitter temperature to be calculated. Also, the tube geometry was such that accurate pyrometric measurements could not be made; therefore, our measurements were of contact potentials between emitter and collector.

Crystallographic directions for all crystals used were determined from the back-scattered Laué patterns shown in Figure 3. The emitters for the W and the Al triodes were $\left[ < 142 > \right]$ oriented Mo crystals. This particular crystal direction was chosen because of its low work function surface, which maximizes the collector current at given emitter temperature. For example, sufficient collector current was obtained at an emitter temperature of $2000^{O}K$.
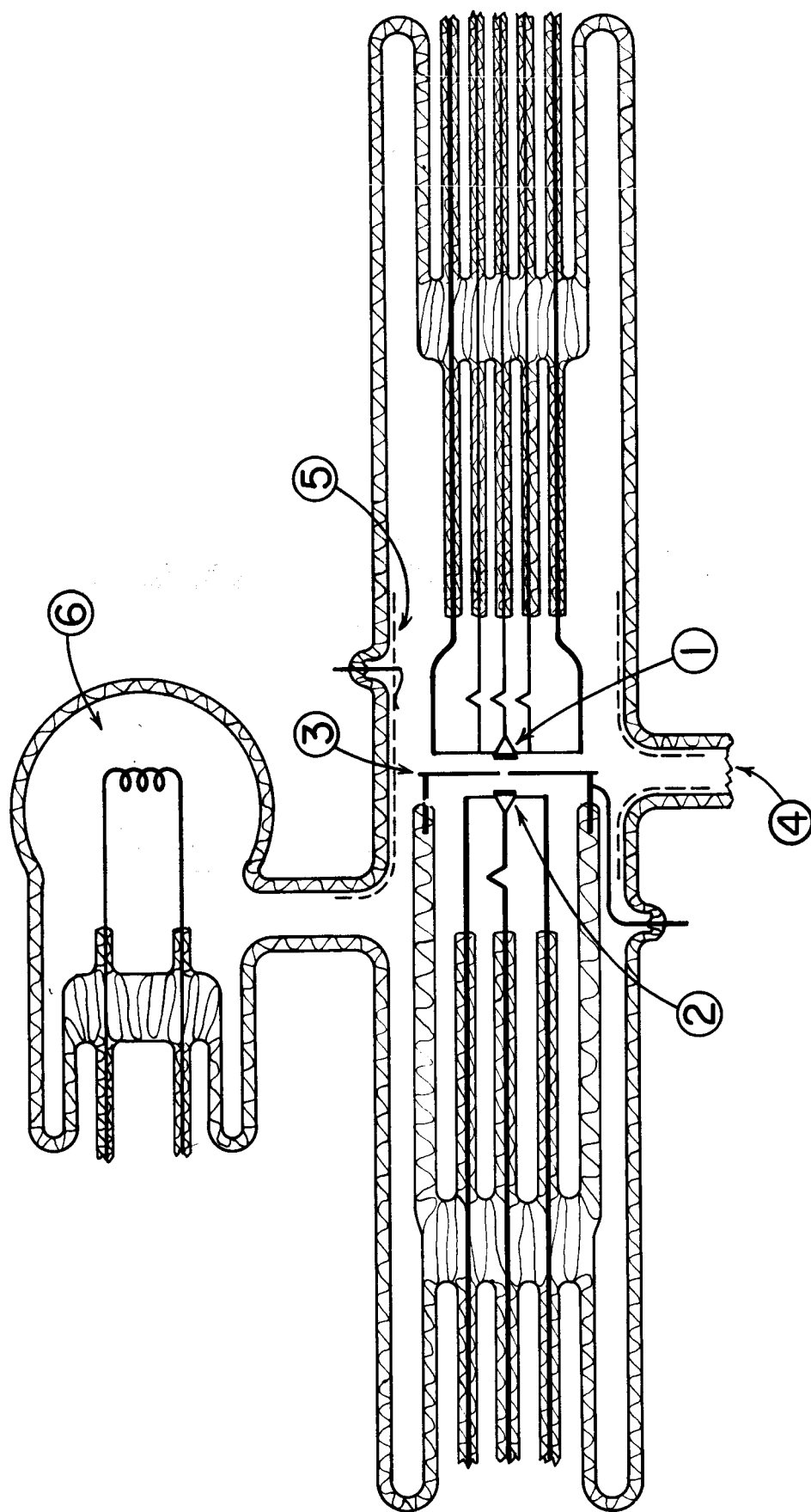
Figure 2.  Retarding potential triode for studying Cs adsorption on various single crystal metals.  1) collector, 2) ⟨142⟩ oriented Mo emitter,  3) accelerating electrode,  4) to Cs reservoir,  5) stannous oxide coating, 6) Ti-Ta getter.
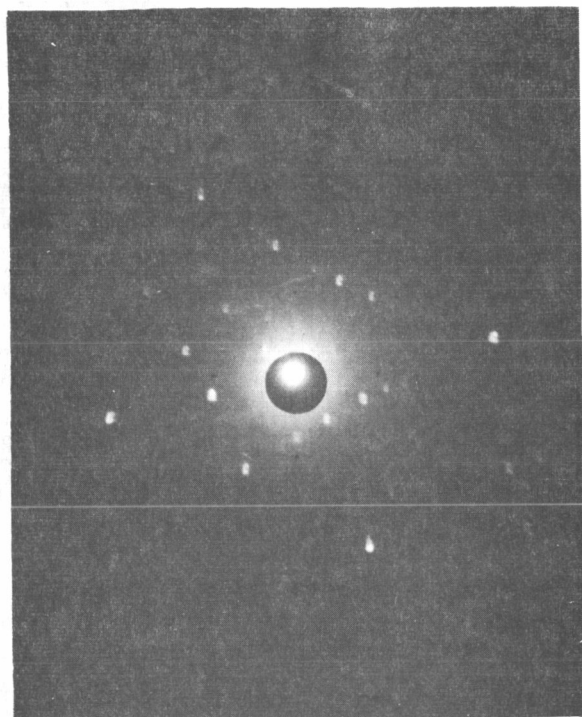
(a)

[221] oriented Aℓ
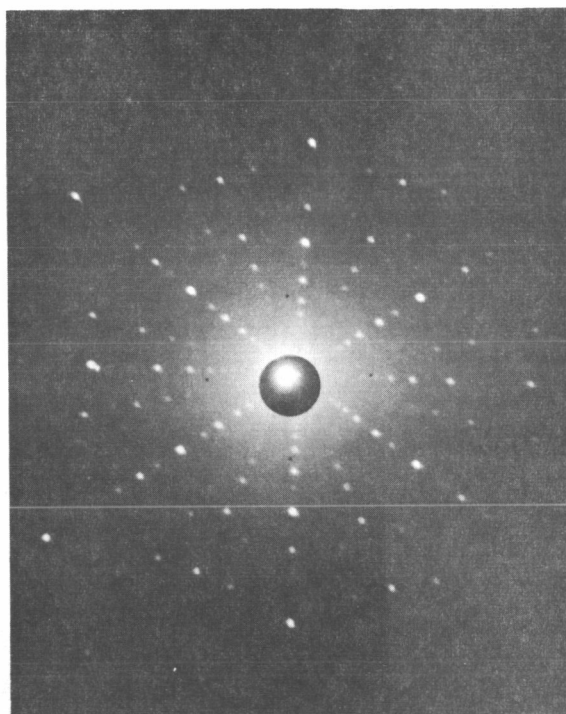
(b)

[110] oriented W
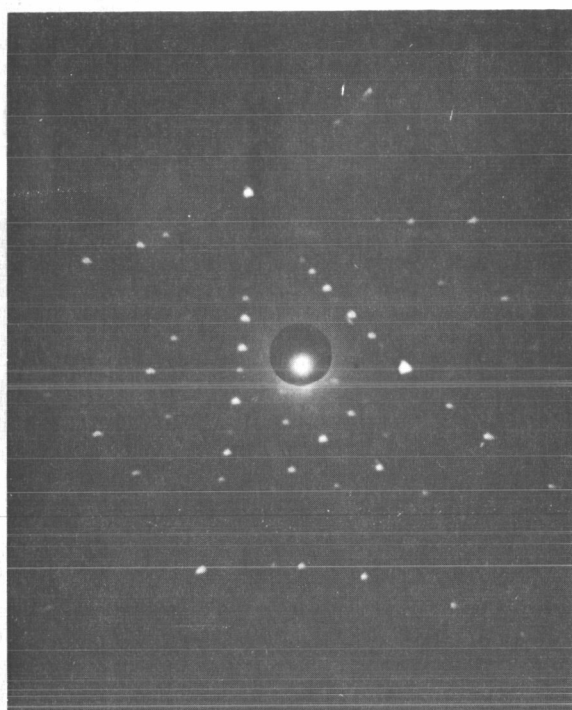
(c)

[142] oriented Mo

(d)
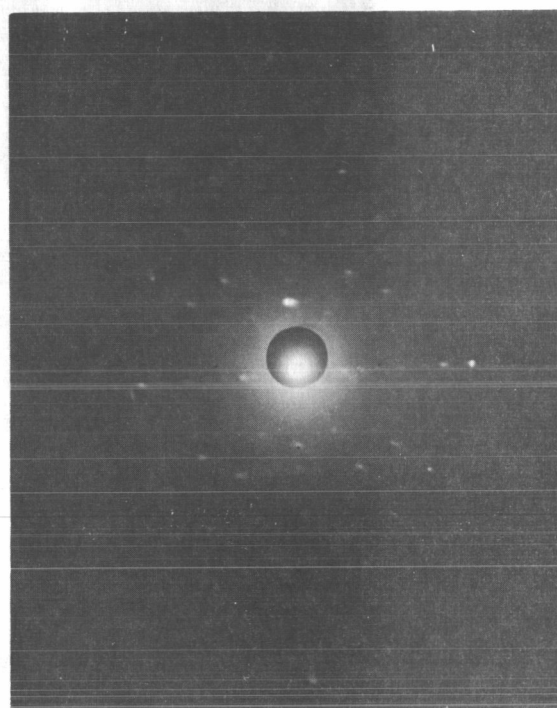
[10Ī0] oriented Ti

Figure 3.    Laué patterns of the various crystals used in the retarding potential triode.

Cesium on Tungsten (110). -The triode shown in Figure 2 was used for this work. The cesium reservoir, shown in detail in Figure 4, was wrapped in a heating coil, in which chromel-alumel thermocouples were imbedded, and encased in a larger glass jacket. Immersing the entire appendage in liquid nitrogen at $77^{\circ}$K allowed the Cs reservoir to be maintained at a constant temperature, thus establishing an equilibrium Cs pressure in the tube. Constant temperature was assured by evacuating the glass jacket to minimize heat conduction losses. Rapid temperature changes were effected by leaving the glass jacket open and utilizing the heat conduction properties of air for cooling the reservoir. The single crystal collector was cut from a .100 inch diameter W zone-melted rod whose orientation was such that the $\{100\}$ direction lay along the axis. The collector cut from this rod had an orientation within $1^{\circ}$ of a (110) plane, the most densely packed plane in the bcc crystal system. Electrochemical machining with a solution of sodium hydroxide reduced the thickness of the crystal to .020 inch, which was sufficient to remove all work damage.

Work function vs coverage data was obtained in an equilibrium pressure of approximately $10^{-8}$ torr. The W crystal was flashed clean of Cs, quenched quickly to a desired temperature, and the change in $V_b$ vs time at a constant collector current was measured under conditions where $V_b < (\phi_e - \phi_c)$. At constant current, $\Delta V_b = \Delta\phi$, and if one assumes a sticking coefficient of unity, $\Delta t$ is proportional to coverage; thus $\Delta V_b$ vs t data was converted directly to $\Delta\phi$ vs $\sigma$.

Equilibrium coverage-temperature data was obtained by adjusting the Cs reservoir temperature in order to establish a constant value of $\mu_p$, then measuring $\Delta\phi$ vs $\sigma$ at $300^{\circ}$K. Next, the collector was raised to a specified temperature until equilibrium was established, quenched rapidly to $300^{\circ}$K, and the time required to reach a specified point on the $\Delta\phi$ vs t curve was measured. By repeating this procedure at other collector temperatures, a curve $\sigma$ vs T at constant $\mu_p$ was constructed. From a family of such curves at different $\mu_p$, it is possible to use Equation (5) to calculate $E_a$. Unfortunately,

17
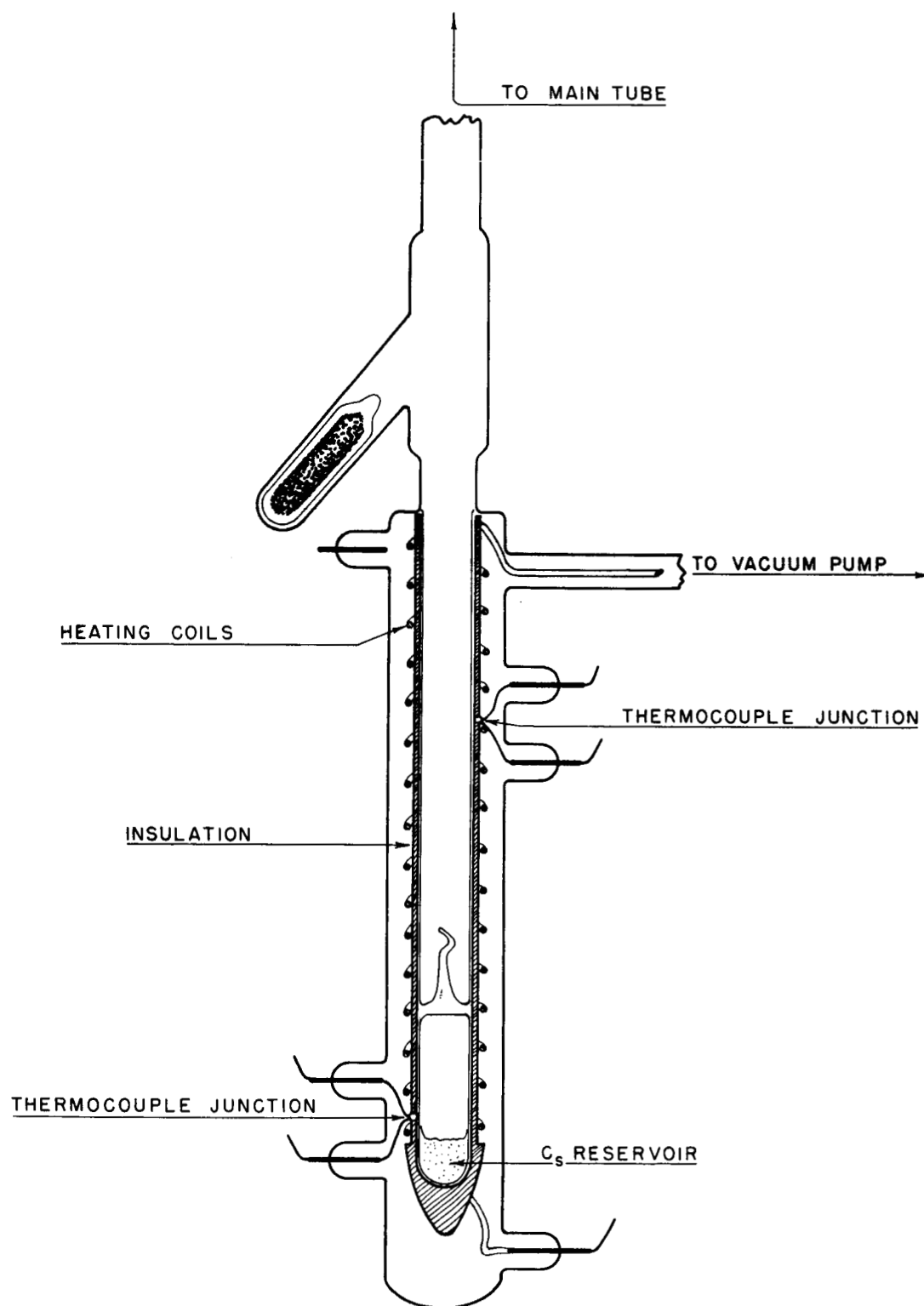
Figure 4.   Cs reservoir used in the triode.

it was impracticable in this tube to vary the Cs pressure over a sufficient range of $\mu_p$ to permit such calculations to be made.

Cesium on Aluminum. - The triode used was of the type shown in Figure 2. The collector crystal was cut from a 0.5 inch diameter cylinder of .99995 pure Al. The usual crystal mounting technique in which the lower edge of the crystal is welded to the supporting wire filament was not suitable for mounting the Al crystal. Drilling a .015 inch diameter hole, inserting the W filament, and crimping the crystal to it proved to be the most successful mounting method.

Considerable work damage introduced into the crystal by the mounting procedure was eliminated by electropolishing with a solution of ortho-phosphoric acid, alcohol, and distilled water. Approximately .010 inch was removed from the surface before all work damage was gone. The resulting crystal was much thicker (.100 inch) than those used in the other triodes. To counteract the effect of the increased surface area of other crystal faces exposed on the thick edges, the crystal was cut so that its diameter was .200 inch, approximately twice the diameter of the other crystals used. Imbedded in the crystal was a Pt-Ni thermocouple by which the temperature of the resistively heated Al crystal was accurately determined. The Laué pattern shown in Figure 3 was made after the Al crystal had been mounted on the W filament and the thermocouple had been inserted.

It is very difficult to obtain clean Al surfaces because of a tenacious oxide layer that forms despite careful handling. Although the procedure followed here did not lead to a clean surface, one can assume that the oxide layer on the surface after the tube was evacuated was less than 50 A in thickness. The procedure was as follows: 1) The crystal was chemically cleaned; 2) it was immediately sealed into the tube in an inert atmosphere; and 3) the tube was evacuated.

There are several ways of obtaining atomically clean surfaces in vacuum. The usual method of heating a metal surface at some temperature sufficient to desorb surface contaminants is not suitable for Al because of its relatively

low melting point. Another technique, sputtering the surface with noble gas ions, was impracticable in our experimental arrangement. The well-known phenomenon of desorption of electronegative gases by bombarding gas-covered metal surfaces with low energy electrons (approximately 100 eV)[9,10,11] was used in an attempt to clean the Al surface. With a residual pressure of $10^{-9}$ torr, the surface was bombarded first with 100 volt, then with 300 volt electrons. No change in work function of the surface was detected; however, this result does not necessarily mean that electron induced desorption did not occur. At room temperature, an oxygen layer would be quite mobile; thus, if oxygen were desorbed from the small area of the crystal where the electrons impinge, diffusion from the surrounding highly oxygenated surfaces of the crystal would make desorption difficult to detect.

The curve of $\Delta\emptyset$ vs $\sigma$ was obtained by heating the crystal to $610^{\circ}K$, maintaining a constant temperature in the reservoir shown in Figure 4, (thereby establishing a constant flux of Cs atoms), cooling the crystal rapidly to $300^{\circ}K$, and recording $\Delta V_b$ as a function of time at constant collector current. Although an undetermined but constant impingement rate allows equilibrium $\Delta\emptyset$ vs $\sigma$ data to be obtained, it does not permit absolute coverage measurements to be made.

Thermal desorption activation energy measurements were attempted under zero pressure conditions. The beam of Cs atoms was directed at the crystal which was kept at a constant temperature between $720^{\circ}K$ and $870^{\circ}K$ in the way described above, until it was assumed that the coverage was uniform over the crystal surface. The Cs source was shut off by quenching the reservoir rapidly to $77^{\circ}K$. The change in $V_b$ required to maintain a constant current was measured as a function of time over a particular coverage interval and for several different temperatures. After making corrections for the temperature dependence of the work function, Arrhenius plots of log t vs 1/T were made of the time-temperature data for a particular coverage interval. Desorption energies can be determined by using Equation (7).

Cesium on Titanium. - A modified version of the RPT with small over-
all dimensions ( .750 inch diameter and 6 inches long) was designed to operate
inside a liquid nitrogen filled dewar positioned between the poles of a
4200 ± 200 gauss magnet.

The Ti crystal was made of one-pass zone-refined material obtained
from Materials Research Corporation. The following is a typical analysis:
metallic impurities less than 130 ppm, gaseous impurities less than 75 ppm,
carbon 78 ppm, and other impurities less than 5 ppm. Work damage intro-
duced when the crystal was cut was removed by electrolytic machining in a
solution of dilute hydrofluoric acid. Approximately .007 inch was removed
from either side of the crystal leaving a smooth disk .020 inch thick of single
crystal Ti oriented along one of the more densely packed hcp planes, the
$(10\bar{1}0)$.

Cs was deposited uniformly and in known amounts from a $C_S$ ion source
placed directly opposite the Ti target. This ion source[12] consisted of a sodium
aluminosilicate molecular sieve powder (Linde Type A zeolite) which had
undergone an ion exchange reaction with $C_S$. A Pt filament was coated
with this material, then heated to $1600^{\circ}$ K in vacuum. Subsequent heating to
$1100^{\circ}$ K caused emission of $C_S$ ions with no neutral content and an impurity
content of less than 0.5%.

Biasing the Ti collector 22.5 volts negative with respect to all other ele-
ments in the tube deposited Cs on the target only. The total collected charge
is a measure of the exact amount of Cs deposited. The accumulated charge
corresponds to a relative coverage; thus a direct measure of $\Delta\phi$ vs $\sigma$ was
made for the unequilibrated surface.

The emitter in this triode tube was a .020 diameter W hairpin filament
etched to .005 inch at the apex. This emitter design was not only easier to
fabricate, but also, by proper positioning of the filament with respect to the
aperture hole, more current was collected at the target. Although this design
did not permit absolute work function determination, contact potentials were

easily measured on a macroscopic single crystal. A rounding of the "knee" of the retarding potential plots resulted from the electric field inhomogeniety; however this had no effect on the contact potential measurements.

## RESULTS AND DISCUSSION

### Work Function Changes with Cesium Coverage

<u>Cesium on Nickel (FEM)</u>. - Considerable difficulty was encountered in obtaining the Ni results because of frequent emitter tip rupture and cleaning problems. It was therefore not possible to obtain absolute coverage data for Ni, although a $\phi$ vs relative coverage curve is given in Figure 5 for what was believed to be a clean Ni substrate. The reported value of the work function of clean Ni $\phi_s$ ranges from 4.5 to 5.2 eV. In order to use Equation (10) to determine the work function for the Cs dosed tip, we have arbitrarily chosen a compromise value of 5.0 eV which lies between the 4.74 and 5.27 eV values recently reported by Riviere[13] and Holscher[14] respectively.

The characteristic FEM pattern changes are shown in Figure 6. The low density (112) plane emits most strongly in a limited low coverage range. Examination of the $\{112\}$ regions of a fcc crystal structure reveals that the (112) consists of slowly undulating rows of close-packed $\langle 110 \rangle$ chains,[15] therefore, a much higher substrate atom density results if the somewhat recessed $\langle 110 \rangle$ chains are also counted. At Cs coverages consistent with $\phi < 3.0$ eV the usual reversal of emission[1-3] begins to occur with strong emission from the vicinals of the high density (111) and (100) planes, reaching a maximum reversal at $\phi_m \sim 1.38$ eV (Figure 6e). Similar to the bcc and hcp substrates studied in the past,[1-3] the pattern reverts to a pseudo-clean emission distribution just beyond $\sigma_m$ as shown in Figure 6f. A further interesting difference in the fcc substrate is the lack of strong emission at any coverage from the third most densely packed (110) plane, whereas the third most densely packed plane of the bcc and hcp structures emits strongly.

22
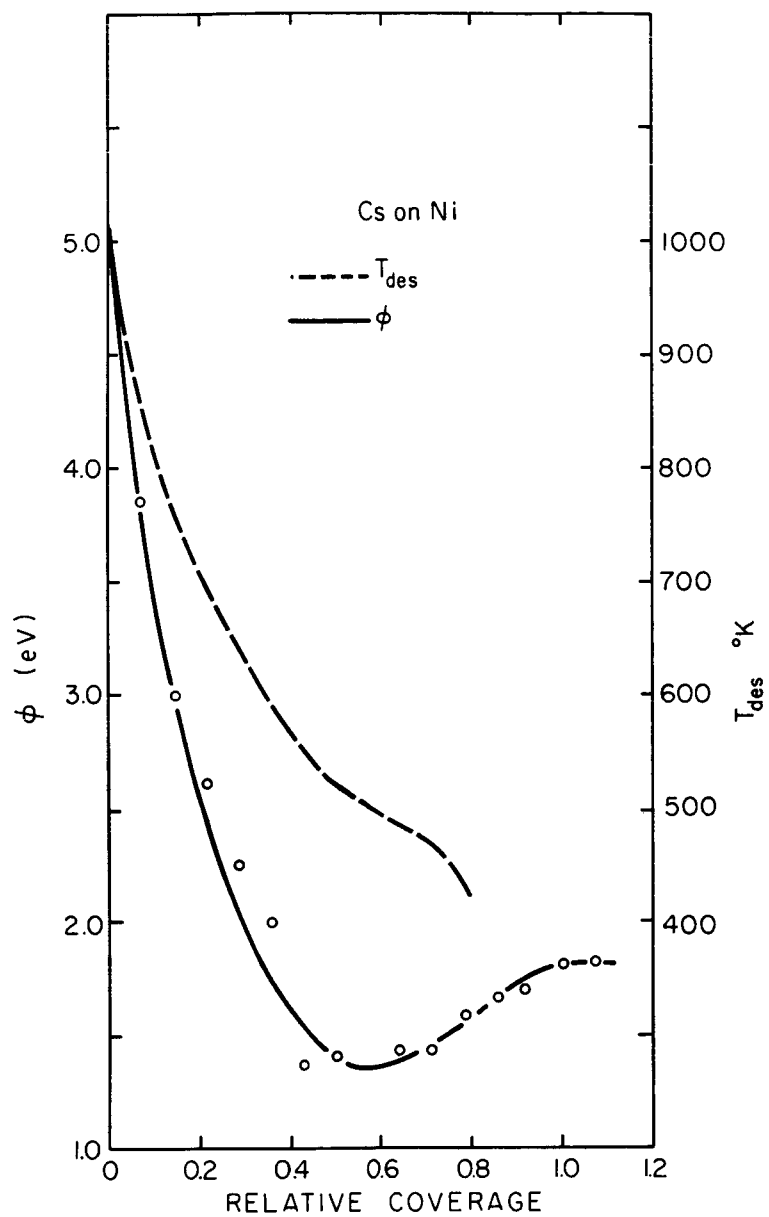
Figure 5.  Work function $\phi$ and desorption temperature $T_d$ as a function of relative Cs coverage for the Cs-Ni system.
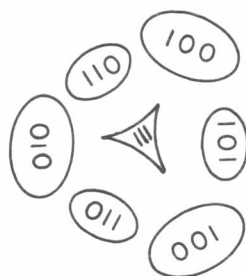
(a)

Principal planes of the
(111) oriented face center-
ed cubic structure belong-
ing to (b).
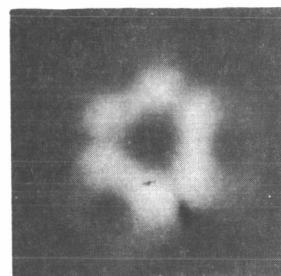
(b)

∅ = 5.00 eV
Clean Ni
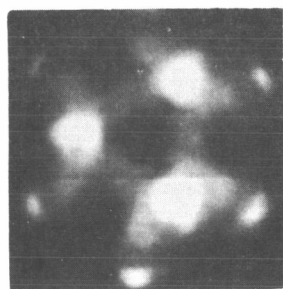
(c)

∅ = 3.86 eV
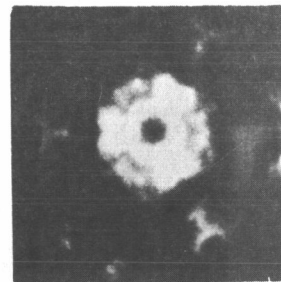
(d)

∅ = 2.21 eV
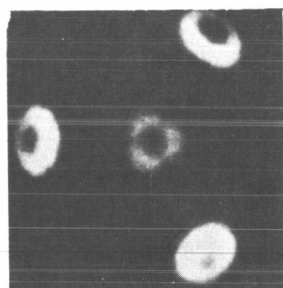
(e)

∅ = 1.38 eV
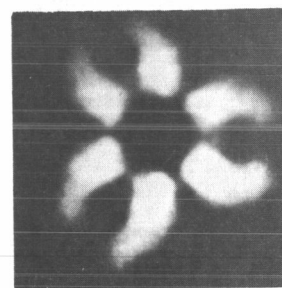
(f)

∅ = 1.43 eV

Figure 6.   Principal pattern changes for Cs on Ni;  heating time,
60 seconds.

The fact that work function lowering is generally greatest on the high density planes for $\sigma < \sigma_m$ is strong evidence that local substrate work function is a more important factor than substrate geometry in determining $\Delta\emptyset$ on various planes for a given average coverage. This implies that local coverage and/or dipole moment per adatom is increased by increasing $\emptyset_s$. In a following section of this report, a general discussion of work function change with $C_s$ coverage for the five different systems studied will disclose that both the local coverage and the dipole moment per adatom increase with $\emptyset_s$.

Cesium on Oxygen-Covered Tungsten (FEM). - In earlier work[1,2] we have shown that various amounts of underlying chemisorbed O greatly alter the $\emptyset$ vs $\sigma$ relationship. The experimentally observed shift in the minimum work function $\emptyset_m$ as a function of underlying oxygen coverage $\sigma_{OW}$ for Cs on the OW surface is shown in Figure 7. The values of $\sigma_{OW}$ were obtained from a $\emptyset$ vs $\sigma$ curve published by George and Steir[16]. Although the effect of O on the $\emptyset$ vs $\sigma$ relationship does not alter the overall shape of the curves from that of the clean $C_s$-W curve, our results show that $\emptyset_m$ goes through a much lower minimum of 1.1 eV as compared with the 1.5 eV minimum for $C_s$ on the clean W surface.

Our earlier results were limited to a maximum $\emptyset_{OW}$ of 5.65 eV. In work described in a later section of this report we were interested in studying the interaction of low energy electrons with coadsorbed O and $C_s$ on a surface where $\emptyset_{OW} > 6.0$ eV. The work function changes with $C_s$ coverage shown in Figure 8 are for an underlying oxygen coverage of $\emptyset_{OW} = 6.3$ eV. The shape of the curve for $\sigma < \sigma_m$ indicates incomplete equilibration of the initial $C_s$ dose; also, the dose size changed during the course of the adsorption experiment. The data shown in Figure 8 has been adjusted to compensate for the change in dose size, however, no adjustment has been made to counteract the effect of incomplete initial dose equilibration. Our past experience has shown that incomplete equilibration leads to higher values of $\sigma$ for a given value of $\emptyset$ for $\sigma < \sigma_m$. This means that the curve shown in Figure 8
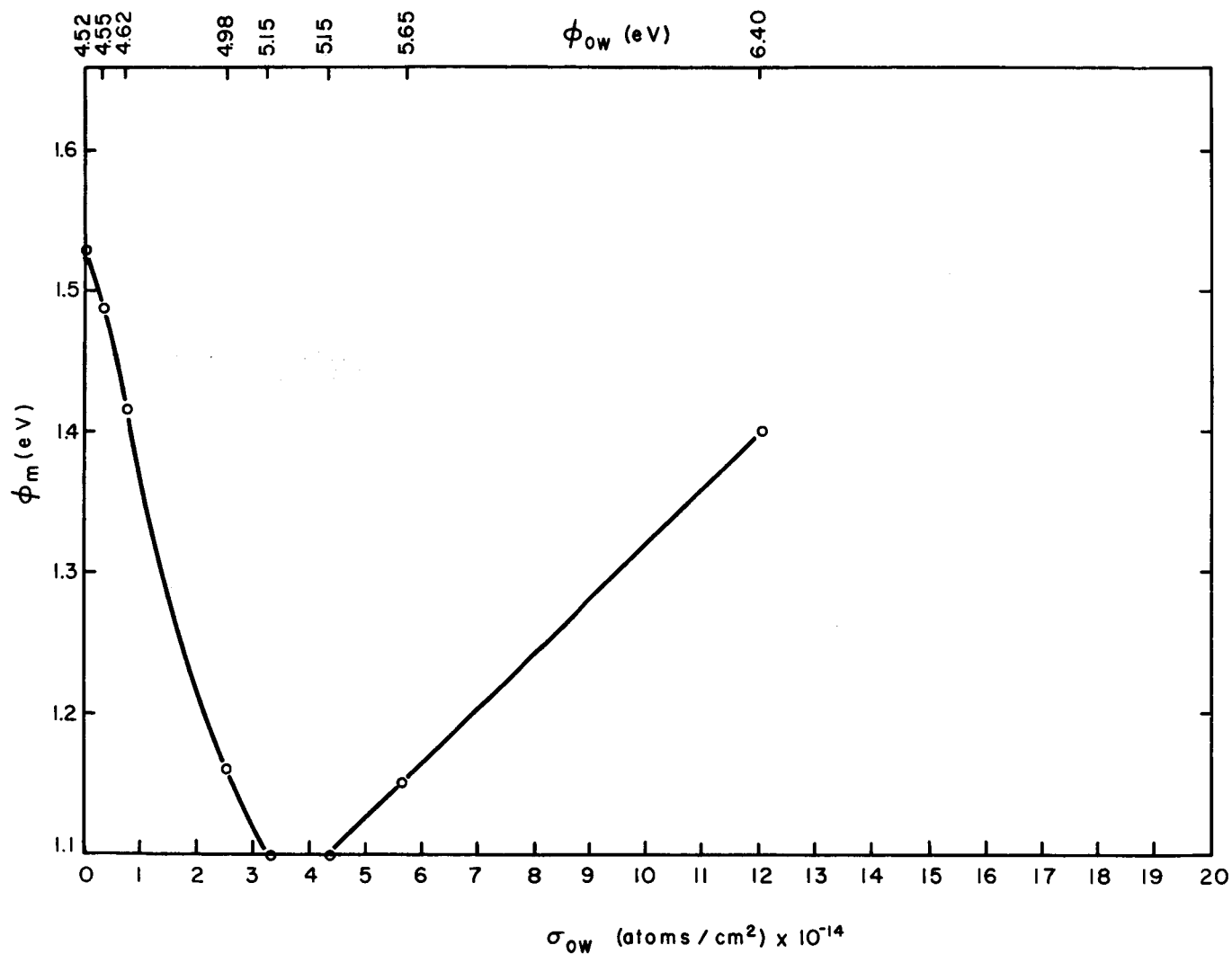
Figure 7. Work function minimum $\phi_m$ as a function of underlying oxygen coverage for Cs on OW. The values of $\phi_{OW}$ are also given at the top of the figure.
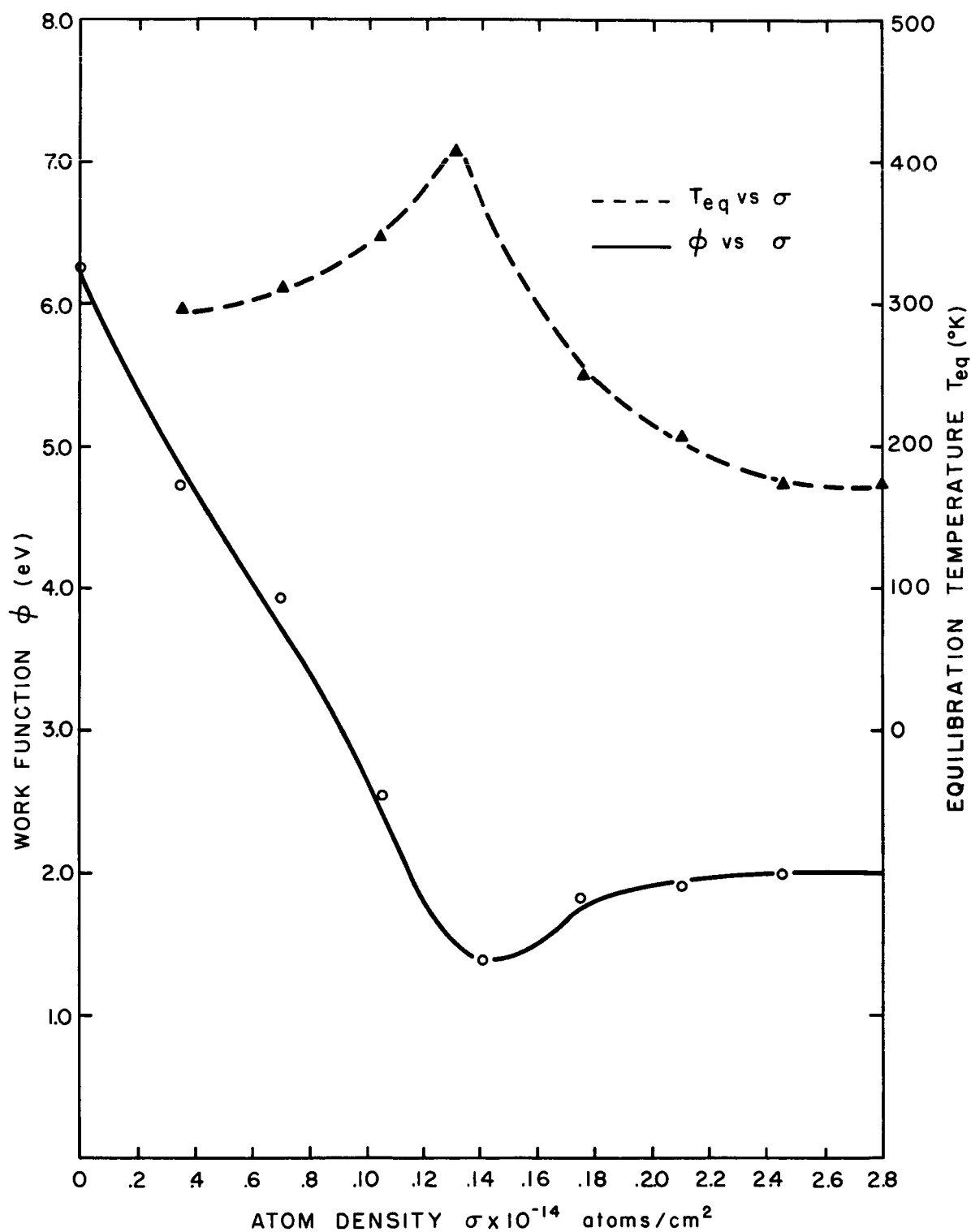
Figure 8. Work function - coverage relationship for Cs on OW for an underlying oxygen coverage corresponding to $\phi_{0W} = 6.3$ eV.

should be shifted to the left so that $\emptyset_m$ occurs at a lower value of $\sigma_m$.

Although our tube configuration did not permit photographing the FEM pattern changes, they were observed to be similar to those obtained in earlier work[2] and shown in Figure 9 for an underlying $\emptyset_{OW}$ = 5.65 eV. A comparison of these pattern changes with those obtained[2] for Cs on clean W shows that the OW surface causes enhanced emission from the $\{112\}$ planes relative to the $\{110\}$ planes for $\sigma < \sigma_m$ whereas for $\sigma > \sigma_m$ the pseudo-clean W emission distribution is obtained as before. Also, relative emission from the (110) plane is reduced by the presence of O.

As in the case of the clean substrate, pseudo-clean substrate patterns are obtained at the near monolayer Cs coverage regardless of the underlying O coverage. This result, coupled with the fact that the work function for the Cs-OW surface approaches a constant value of $\sim 1.8$ eV at $\sigma > \sigma_m$ independent of $\sigma_{OW}$, implies a screening of the OW dipole contribution by the Cs layer and a near uniform value of $\Delta\emptyset$ over the polycrystal face surface of the emitter.

Cesium on the (110) Plane of Tungsten (RPT). - With the Cs reservoir in the RPT held at 273°K for sufficient time to establish an equilibrium pressure, the $\Delta\emptyset$ vs $\sigma$ curve of Figure 10 was obtained. Heating of the center electrode by the emitter resulted in uncontrolled pressure gradients in the interelectrode gap. Reproducible results were obtained by allowing the emitter to cool between the data points and operating the emitter only when making each measurement. Thus, measurements were made under steady state, but not equilibrium conditions; hence the absolute Cs impingement rate could not be established from the reservoir temperature.

The coverage scale in Figure 10 was obtained by assuming the value of $\sigma_m = 1.95 \times 10^{14}$ atoms/cm$^2$ as determined earlier by field emission methods. A comparison of the curves obtained by the two methods shows several striking differences which are summarized in Table II.
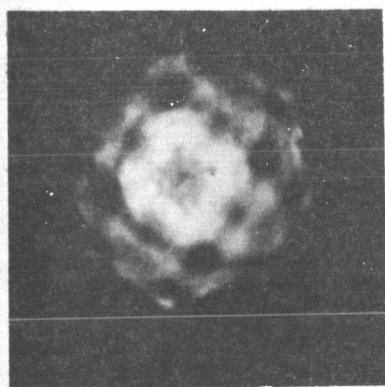
(a)

$\phi$ = 5.65 eV

Oxygen on Clean Tungsten
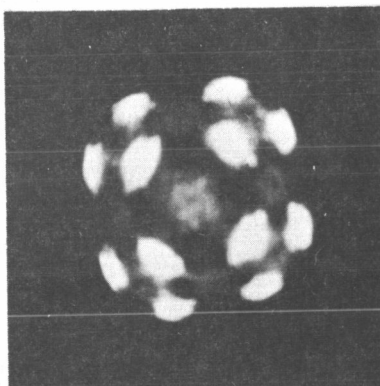
(b)

$\phi$ = 2.27 eV
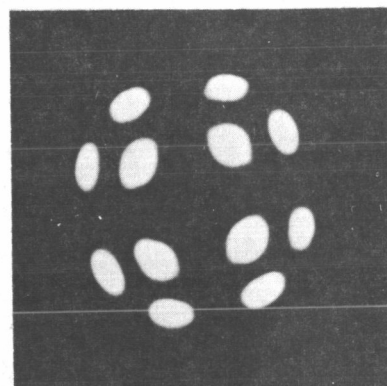
(c)

$\phi$ = 1.61 eV
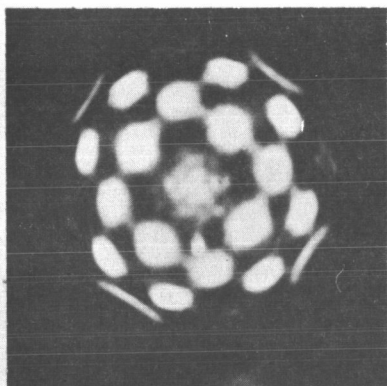
(d)

$\phi$ = 1.50 eV
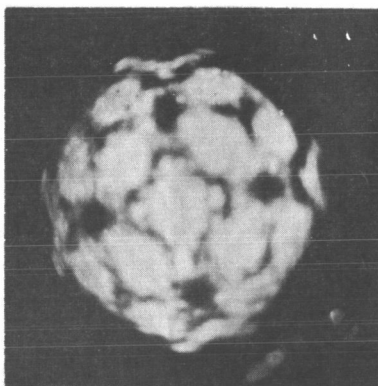
(e)

$\phi$ = 1.13 eV
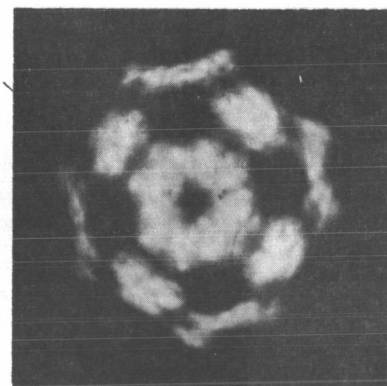
(f)

$\phi$ = 1.35 eV

Figure 9.  Principal field emission pattern changes for Cs adsorption on a ⟨100⟩ oriented W tip initially covered with a partial chemisorbed layer of oxygen.
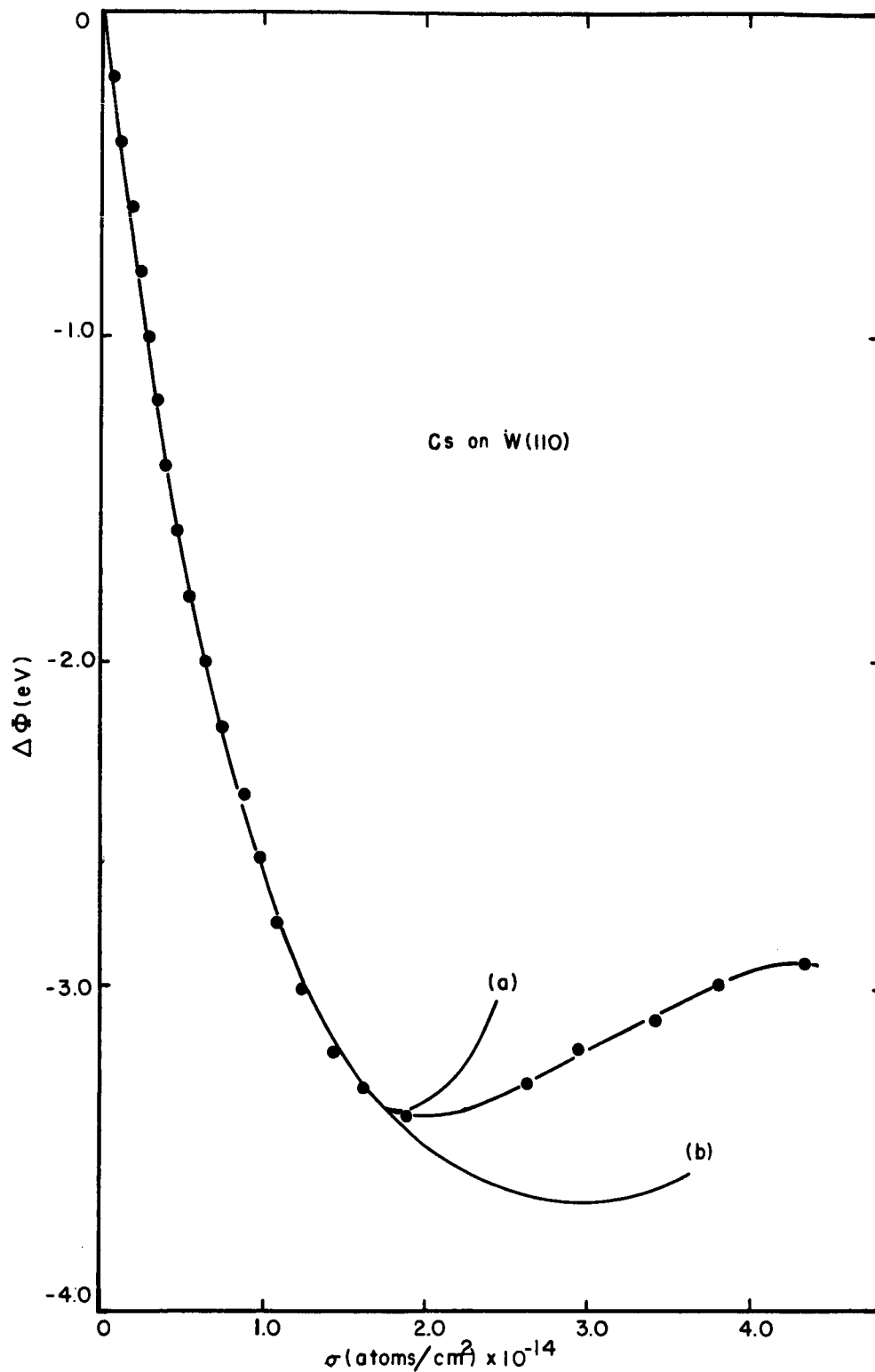
Figure 10. Data points show the work function-coverage relationship for the Cs-W(110) system at 300°K. Curve is normalized so that $\sigma_m = 1.95 \times 10^{14}$ atoms/cm$^2$. Curve (a) is best fit curve of Equation (16) and curve (b) is best fit curve of Equation (13)

30

TABLE II

Comparison of Salient Features of the $\emptyset$-$\sigma$ Relationships Determined

by Field Emission and Retarding Potential Methods

|  | $\Delta\emptyset_m$ (eV) | $\sigma_o / \sigma_m$ | $\Delta\emptyset_o / \Delta\emptyset_m$ |
|---|---|---|---|
| Field Emission | 4.45 | 1.50 | 0.86 |
| Retarding Potential | 3.40 | 2.05 | 0.83 |

Besides the smaller value of $\Delta\emptyset_m$, the retarding potential method gives a much larger value of $\sigma_o$, i.e., the coverage where $\Delta\emptyset$ becomes independent of $\sigma$. A probable explanation for the different values of $\emptyset_o$ by the two methods is the possible occurrence of simultaneous Cs desorption at coverages above $\sigma_m$. Earlier studies[1] of Cs desorption indicate that perceptible desorption begins at $\sigma > 2.3 \times 10^{14}$ atoms/cm$^2$ for T = 300°K. This means that for $\sigma \gtrsim \sigma_m$ the data points should be shifted to the left in the $\Delta\emptyset$-$\sigma$ relationship shown in Figure 10. To confirm this possibility one may examine the shape of the $\Delta\emptyset$-$\sigma$ curve as the substrate temperature is lowered below 200°K where desorption in the monolayer region is negligible. By immersing the collector leads in liquid $N_2$ we were only able to lower the collector temperature to 275°K where no change in the shape of the $\Delta\emptyset$-$\sigma$ curve was observed.

The 3.4 eV maximum work function change $\Delta\emptyset_m$ on Cs adsorption permits an estimate of $\emptyset_{W(110)}$, the clean work function of the (110) plane. Using the results of earlier field emission studies[2] which showed that $\emptyset_m$ = 1.5 eV, one can calculate the substrate work function from the relationship:

$$\emptyset_s = \emptyset_m + \Delta\emptyset_m \qquad (12)$$

Using Equation (12), $\emptyset_{W(110)}$ = 4.9 eV. This value is approximately 1.0 eV below the $\emptyset_{W(110)}$ value normally obtained by field emission techniques.

The reason for this large discrepancy between the values of $\phi_{W(110)}$ determined by the two methods is not clear at this time. One possible explanation is the fact that macroscopic (110) crystal faces are sufficiently rough, regardless of careful smoothing, that contributions from other low $\phi$ crystal faces lower the value of $\phi_{(110)}$ to the observed value.

Cesium on Aluminum (RPT). - The changes in work function with Cs coverage at $300^\circ$K on the (221) plane of Al are shown in Figure 11. These results were also obtained under steady state conditions, therefore the coverage scale in Figure 11 could not be made absolute. The curve of Figure 11 is normalized so that $\phi_m$ occurs at $\theta = 0.67$. The shape of the curve is similar to that obtained for Cs on the other substrates for $\theta < \theta_m$, however that portion of the curve $\theta > \theta_m$ is similar to that shown in the (110) W results. This suggests that with Al, as with W, desorption is taking place at $300^\circ$K for $\theta > \theta_m$.

The most striking difference between the Al curve and that of the Ni, OW, and W(110) curves is the very low value of $\Delta\phi_m = 3.15$ eV. This result is not surprising because the Al substrate has a much lower clean $\phi_s$ than any of those listed above. All substrates studied for which accurate values of $\phi_m$ could be determined have approximately the same value of $\phi_m = 1.5$ eV, the exact value being slightly lower for the high $\phi$ substrates and slightly higher for the low $\phi$ substrates. Using this value, one can use Equation (12) to calculate the clean $\phi_{Al(221)} = 4.65$ eV. One would expect that a densely packed plane such as the (221) would be a high $\phi$ plane; therefore the value of 4.65 eV appears reasonable compared with the generally accepted[17] average $\phi \sim 4.2$ eV.

Cesium on Titanium (10$\bar{1}$0)(RPT). - Ti changes from a hcp crystalline structure at room temperature to a bcc structure at temperatures above $1150^\circ$K.[5] To avoid changing the crystal structure most of the heating of the Ti target in the RPT, either during evacuation or in subsequent experiments, was done below this temperature, with only a few flashes to higher temperature being done on the vacuum system for outgassing purposes. A concurrent FEM study of Ti revealed that a clean surface could not be obtained at any temperature
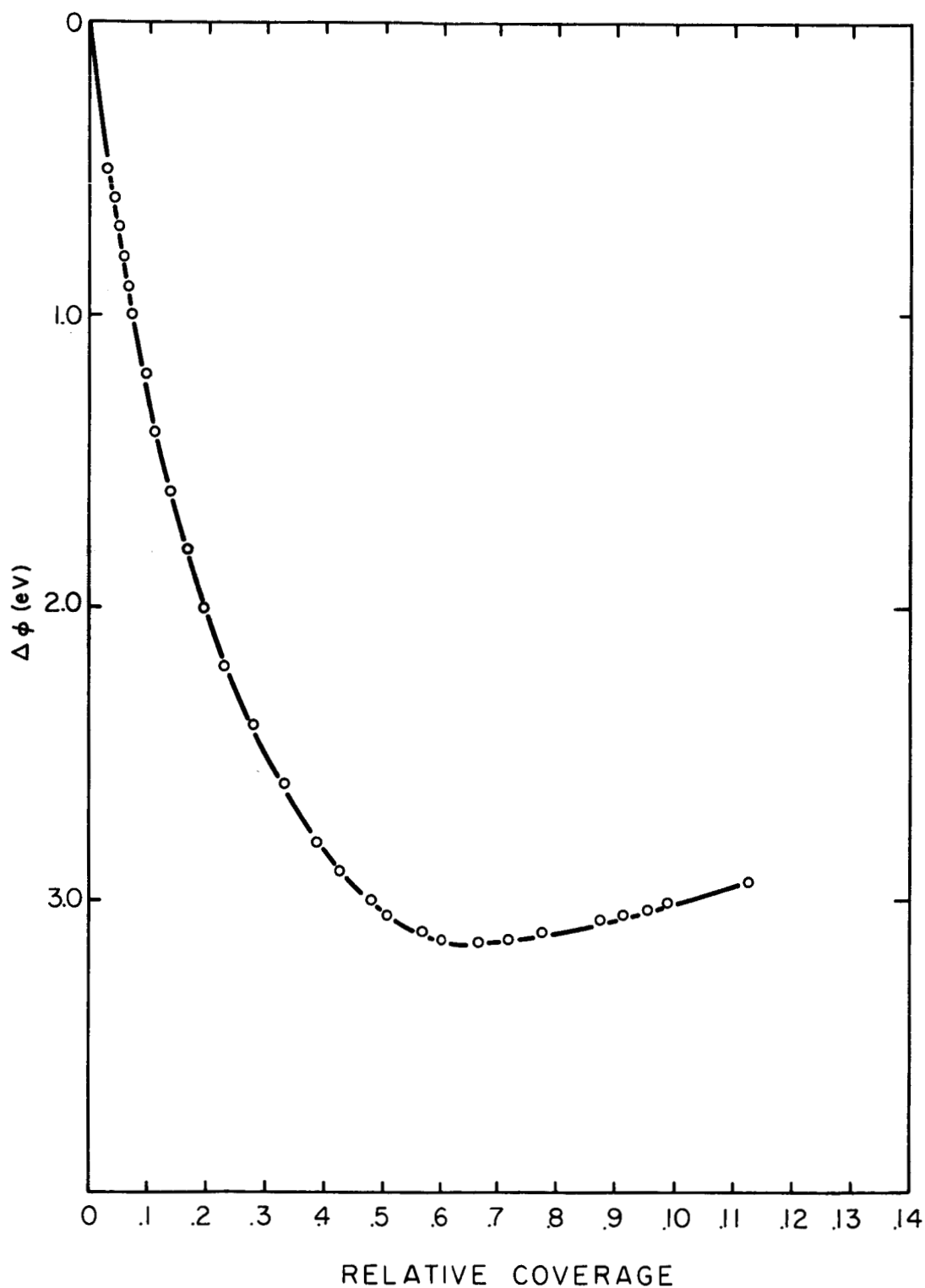
Figure 11. Work function change with Cs coverage for the Cs-A$\ell$(221) system. The relative coverage is normalized so that $\Delta\phi_m$ occurs at a relative coverage of 0.67.

below the melting point; also, the Ti FEM patterns failed to show the symmetry expected of a single crystal. Brock[18] has shown that heating for as much as 200 hours below the transformation temperature does not change the crystalline structure. Thus the target surface in the present work was probably a partially contaminated $\langle 10\bar{1}0 \rangle$-oriented hcp Ti, the contaminant probably being oxygen. The retarding potential characteristic of this surface was stable and reproducible.

Figure 12 shows the curve of $\Delta\phi$ vs $\theta$ obtained by accumulating unequilibrated doses of Cs on the Ti crystal at $77^{\circ}$K from the Cs ion source. For this curve, the monolayer is arbitrarily chosen as that coverage at which no further change in $\phi$ occurs with increasing coverage. It is interesting to compare the curve for the unequilibrated Ti surface (Figure 12) with the curve for the equilibrated Ni substrate (Figure 5). Both curves were obtained at $77^{\circ}$K where thermal desorption and diffusion are negligible. The most significant feature of such a comparison is the similarity in the shapes of the curves throughout the entire coverage range.

The relatively low value of $\Delta\phi_m$ = 2. 92 eV for Ti suggests that the $(10\bar{1}0)$ plane of Ti possesses a fairly low clean $\phi$. Using Equation (12) and the 1. 5 eV value for $\phi_m$ as before, one can assign the clean Ti $(10\bar{1}0)$ surface a work function of 4. 42 eV. The recommended value[19] for the average $\phi$ for clean Ti is 3. 95 eV, therefore our suggested value for the densely packed, high work function $(10\bar{1}0)$ plane is reasonable.

### General Discussion of Work Function vs Coverage

Comparison With Theory. - The applicability of various theories of work function coverage can be evaluated from the results shown in Figures 5, 8, 10-12. We have examined two $\Delta\phi$-$\sigma$ relationships for each of these curves. The first of these is the point dipole depolarization model of Topping which can be described in terms of $\mu_o$, the zero coverage dipole moment, and $\alpha$, the effective adsorbate polarizability by the general equation:
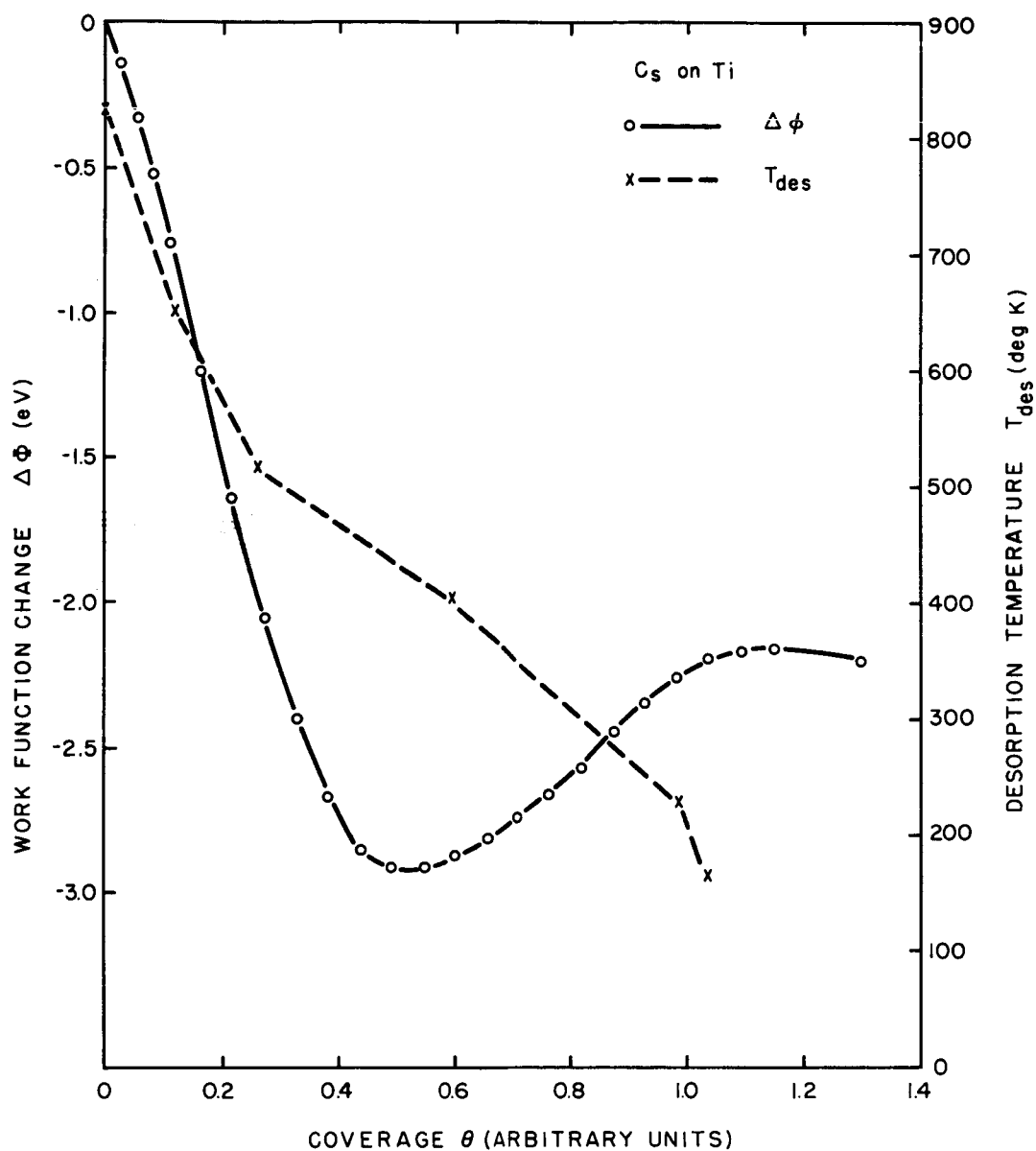
Figure 12. Work function change $\Delta\emptyset$ and desorption temperature $T_o$ as functions of relative Cs coverage $\theta$. The curve is normalized so that unit relative coverage occurs when $\emptyset$ reaches $\emptyset_o$.

$$\Delta\emptyset = \frac{C_1 \theta}{1 + C_2 \theta^{3/2}} \tag{13}$$

where $C_1 = 2 \pi \mu_o \sigma_o$ and $C_2 = 9 a \sigma_o^{3/2}$. From the condition for a minimum in $\Delta\emptyset$ one can deduce the following relationship from Equation (12):

$$C_1 = \frac{3 \Delta\emptyset_m}{\theta_m} = 4 \pi \mu_o \sigma_o \tag{14}$$

and

$$C_2 = \frac{2}{\theta_m^{2/3}} = 9 a \sigma_o^{3/2} \tag{15}$$

From the above relationships one can ascertain values of $C_1$ and $C_2$ which will allow matching of experiment and theory at $\theta_m$. Table III lists the estimated value of $\mu_o$ and $\sigma_o$ for the four systems studied based on the values of $C_1$ and $C_2$ obtained from Equation (13) assuming that $a$ is the same for all systems as it is for the W(110) ($a = 43 \, \text{Å}^3$).

TABLE III

Estimated values of zero coverage dipole moment $\mu_o$ and $\sigma_o$, the coverage at which $\Delta\emptyset$ is independent of $\sigma$, for the various substrates studied. Calculations are based on Equation (13) and assuming $a = 43 \, \text{Å}^3$ is the effective adsorbate polarizability. Also listed are substrate work function $\emptyset_s$ calculated from Equation (12).

| Substrate | $\emptyset_s$ | $\mu_o \times 10^{18}$ esu | $\sigma_o \times 10^{-14}$ atoms/cm$^2$ |
|---|---|---|---|
| Ni (Average) | 5.0 | 19.3 | 4.82 |
| W (110) | 4.90 | 19.4 | 2.92 |
| Al (221) | 4.65 | 16.8 | 4.19 |
| Ti (10$\bar{1}$0) | 4.42 | 17.7 | 2.96 |

Equation (13) fit the Al data throughout the coverage range; however, for the other systems studied, Equation (13) could be fit to the data only in the coverage range $0 < \theta < \theta_m$. In an earlier report[3] field emission $\Delta\phi$-$\sigma$ data could be more readily described by a quadratic relation of the form:

$$\Delta\phi = C_3\theta - C_4\theta^2 \tag{16}$$

If one looks at the limit as $\theta \to 0$ of the derivatives of both Equations (13) and (16) one can see that $C_1 = C_3$. Using identical values of these two constants and appropriate values of $C_2$ and $C_4$ one finds complete overlap between Equations (13) and (16) in the coverage range $\theta < \theta_m$ as shown in Figure 10. This only serves to underscore the difficulty in deciding upon the validity of the Topping model throughout the coverage range as opposed to some other model which might lead to a quadratic dependence, such as Equation (16).

There now exists some evidence[1,20] that in the coverage range $\sigma > \sigma_m$ a restructuring of the adlayer takes place to form a more condensed two-dimensional layer which is not particularly influenced by substrate structure. This may account for the breakdown of the Topping model at $\sigma > \sigma_m$, since this model is based on a square or hexagonal array of adatoms contracting uniformly with increasing coverage. It is in the coverage range $\sigma > \sigma_m$ that the most rigorous test of the Topping model occurs. The results shown in Figure 10 demonstrate that for mobilely adsorbed Cs on the (110) plane of W, the Topping model is seriously inadequate. A similar analysis of immobilely adsorbed Cs on the $(10\bar{1}0)$ plane of Ti leads to the same conclusion.

<u>Comparison Between Systems.</u> - The examination of these results along with those obtained earlier for other systems show that there is a definite relationship between substrate work function $\phi_s$ and the maximum work function change with Cs adsorption $\Delta\phi_m$. Our studies have shown that there is a slightly smaller value of $\phi_m$ for the higher $\phi_s$.

In Figure 13 a plot of $\Delta\phi_m$ vs $\phi_s$ for Cs on various substrates shows that
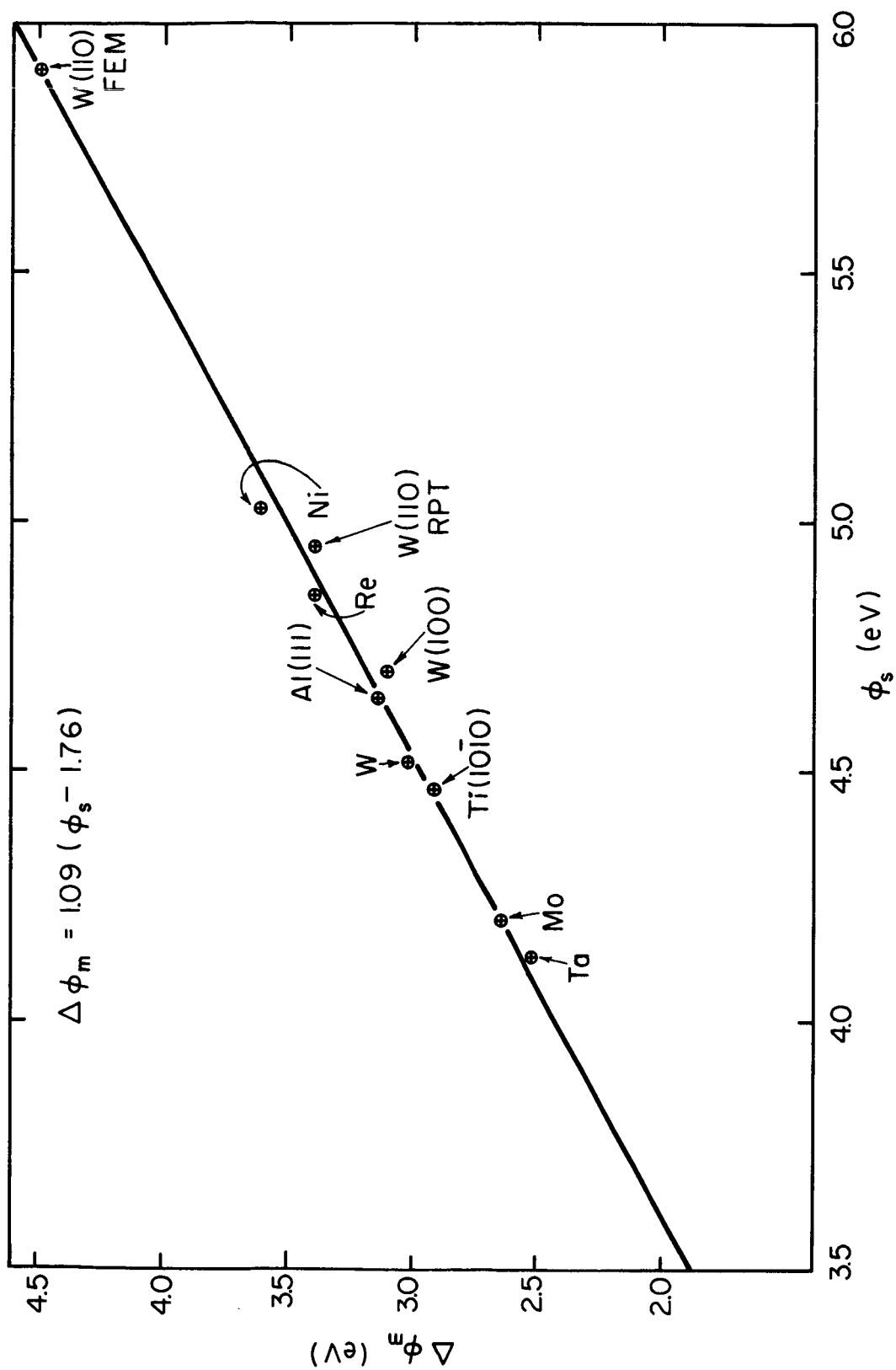
Figure 13. Maximum work function change on Cs adsorption $\Delta \phi_m$ as a function of substrate work function $\phi_s$ for several metal substrates.

$$\Delta \phi_m = 1.09 \, (\phi_s - 1.76)$$

a linear relationship exists of the following form:

$$\Delta \emptyset_m = 1.09 \, (\emptyset_s - 1.78) \text{ eV} \qquad (17)$$

This relationship indicates that $\emptyset_s$ is a fundamental substrate parameter governing $\Delta \emptyset_m$. The single plane values of $\emptyset_s$ for Ti and Al were calculated using Equation (12) and assuming $\emptyset_m = 1.5$ eV. Using both single crystal face and average values of $\Delta \emptyset_m$, the results plotted in Figure 13 indicate good agreement with the empirical Equation (17). The relationship Equation (17) can be extended[21] by noting that the ionization potential $I_a$ is the fundamental adsorbate parameter governing $\Delta \emptyset_m$. A review of existing experimental results suggests that a more generalized form of the empirical relationship Equation (17) will fit most of the Group IA and IIA adsorbates on various metals

$$\Delta \emptyset_m = k_1 (\emptyset_s - k_2 I_a) \qquad (18)$$

This provides a potentially useful empirical means of calculating $\Delta \emptyset_m$ for Group IA and IIA adsorbates on various metallic surfaces; in addition, it provides further insight as to the significance of various adsorbate and substrate parameters in establishing $\Delta \emptyset_m$.

Binding Energy of Cesium to Various Substrates

Cesium on Nickel (FEM). - The temperature required to desorb Cs in 60 second heating intervals is plotted as a function of coverage in Figure 5. Actual desorption times required for the construction of Arrhenius plots were much longer, ranging from 30-1200 seconds. In Figure 14 and 15, the voltage V required to maintain a constant field emitted current is plotted as a function of time at various temperatures for low coverage ionic and neutral desorption respectively. The $\Delta \emptyset$ vs $\sigma$ results reported in the preceding section show that, in the low coverage range $\emptyset$ is proportional to $\sigma$. Through the Fowler-Nordheim relationship (Equations (8), (9)) $\emptyset$ is proportional to $V^{2/3}$,
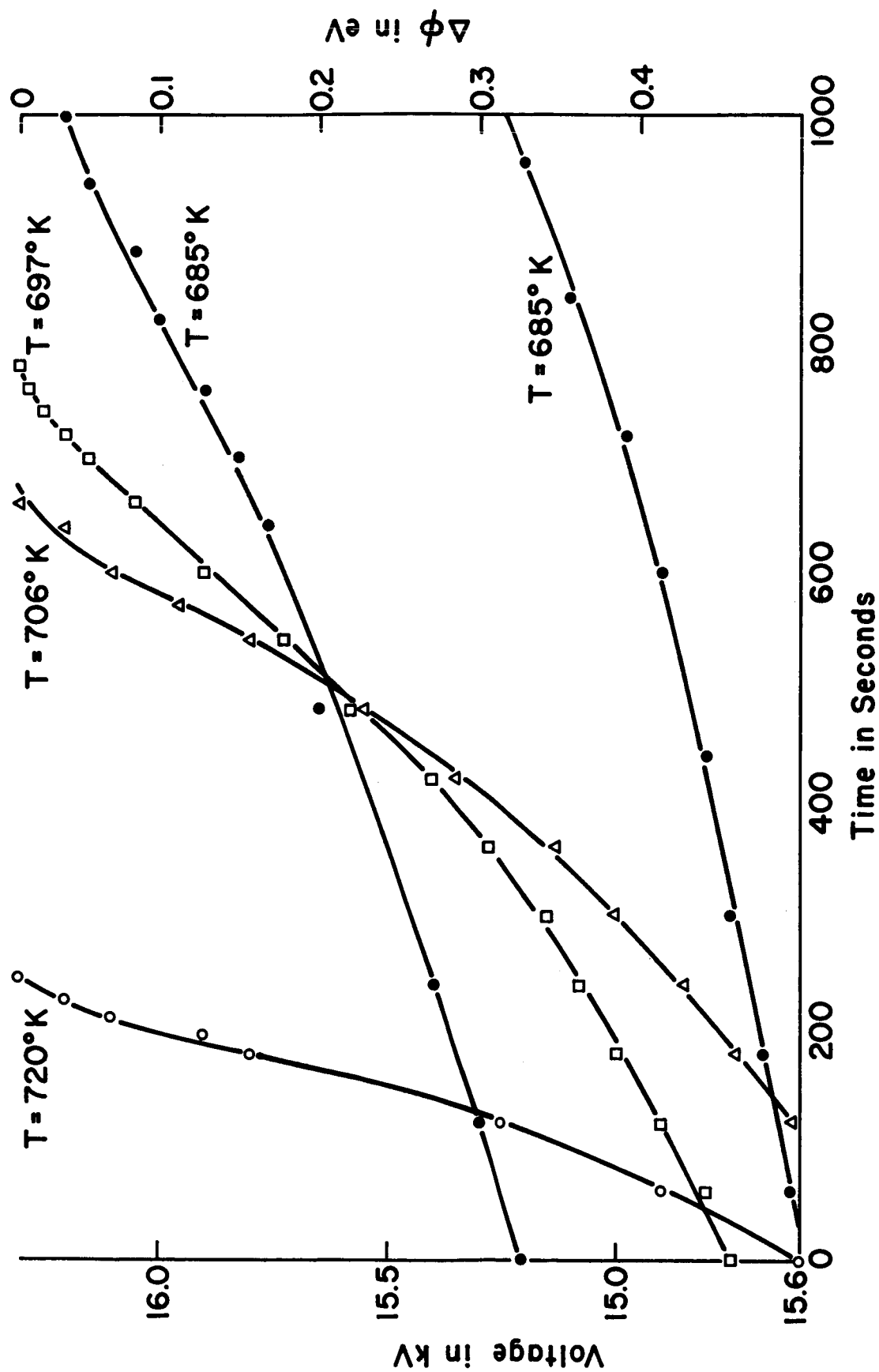
Figure 14. Voltage vs time at constant emission current for low coverage Cs ion desorption from Ni at various temperatures.
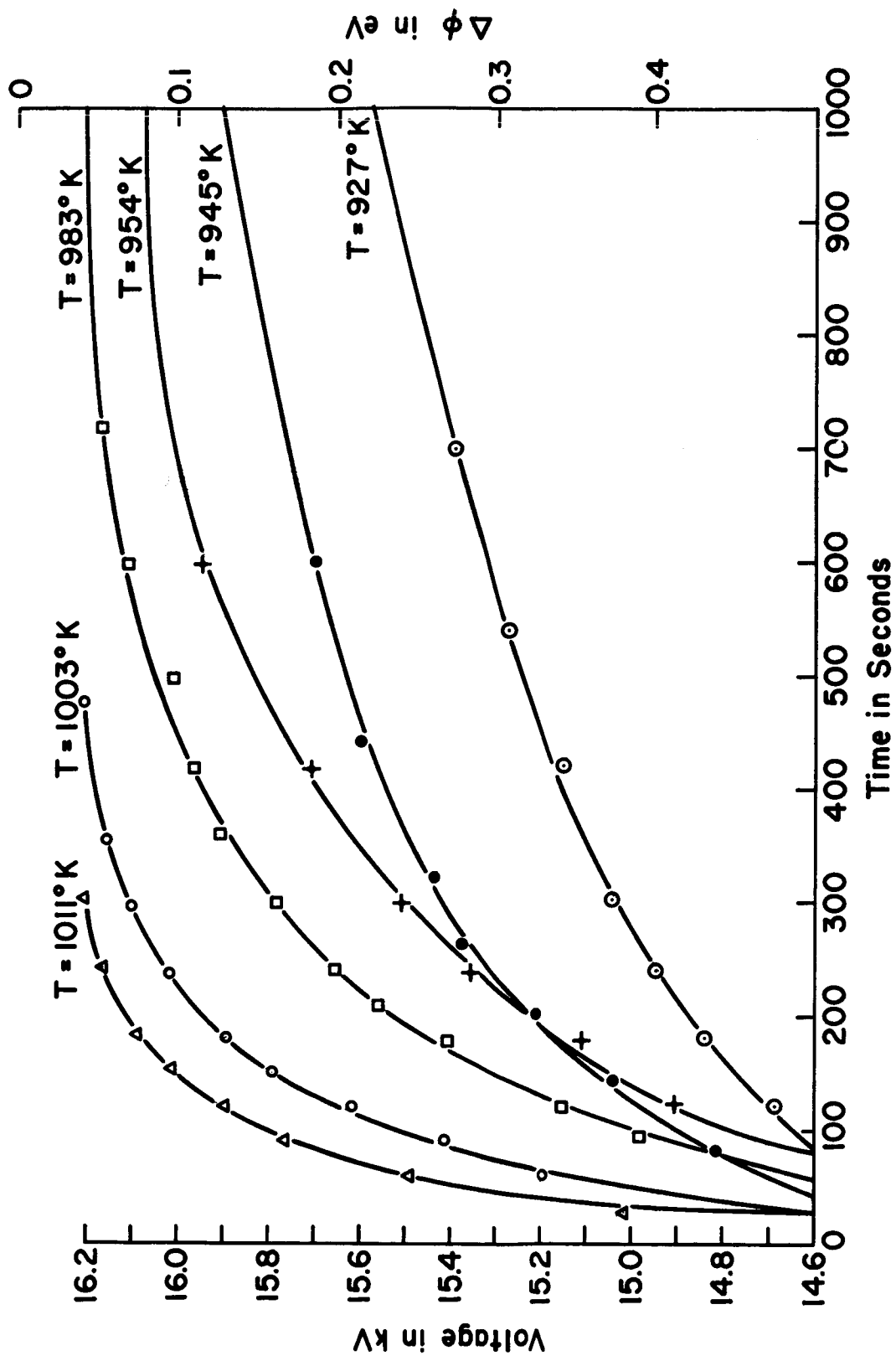
Figure 15. Voltage vs time at constant emission current for low coverage desorption of Cs atoms from Ni at various temperatures.

41

therefore one can relate a voltage interval directly to a coverage interval.

Activation energies for neutral and ionic desorption, $E_a$ and $E_p$, and the average frequency factor $\nu$ were determined for several coverage intervals from Arrhenius plots constructed from the data of Figures 14 and 15. These values were obtained by dividing the coverage interval between $\theta = 0$ and $\theta = .05$ (corresponding to a total $\Delta\emptyset = 0.5$ eV) into five equal coverage intervals each correspondong to a coverage change $\Delta\theta = .01$. The resulting activation energies and average frequency factors are shown in Figure 16. Extrapolating this data, the activation energy for zero coverage desorption of neutrals and ions are $E_a = 3.1 \pm .20$ eV and $E_p = 2.20 \pm .20$ eV.

The activation energies obtained over a finite coverage interval from a polycrystal face surface are weighted averages. In a kinetic measurement such as ours, the measured activation energy depends upon whether equilibrium is maintained during desorption. If equilibrium is maintained during desorption, by surface diffusion, both $E_a$ and $E_p$ will be weighted towards the most tightly bound sites that are contributing significantly to the desorption. It is important to note that the regions from which ionic desorption occurs are not necessarily the same as those from which neutral desorption is taking place. Under conditions of surface equilibrium, one can write an effective work function, corresponding to those regions of the substrate from which ionic desorption is taking place.

$$\emptyset_{eff} = E_a - E_p + I_a \tag{19}$$

The values of $\emptyset_{eff}$ obtained from Equation (19) are plotted in Figure 16 as a function of $\emptyset$. Terminal ionic desorption occurs on the high work function planes where desorption rates are high and corresponding values of $E_p$ are low. In contrast, zero coverage neutral desorption rates are generally low and $E_a$ is high, thus one would expect $\emptyset_{eff}$ to be higher at zero coverage than the average work function. The fact that the value of $\emptyset_{eff} = 4.77 \pm 0.30$ eV calculated here is slightly low compared to the generally accepted value of
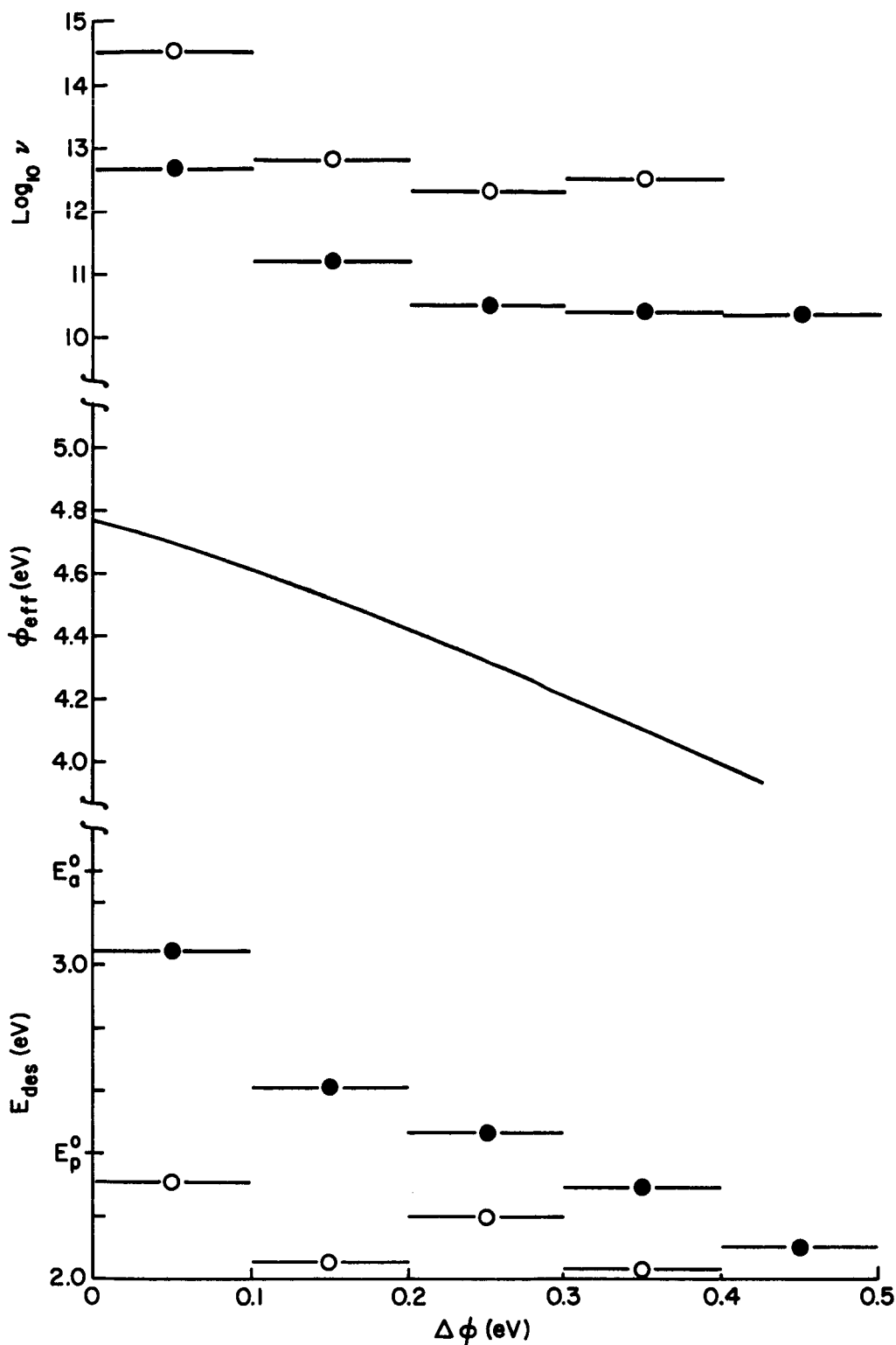
Figure 16. Desorption activation energies $E_{des}$ and average frequency factors $\nu$ for Cs ions (open circles) and neutrals (solid circles) from Ni plotted as a function of work function change $\Delta\phi$. The solid bars correspond to the coverage interval over which the measurements were made. Also shown is $\phi_{eff}$ calculated from Equation (19).

the average clean $\phi \sim 5.0$ eV for Ni suggests that neutral desorption energy measurements are obtained from a different region of the surface than that from which $E_p$ is obtained.

Cesium on the (110) Plane of Tungsten (RPT). - The equilibrium Cs coverage vs temperature results for various impingement rates are shown in Figure 17. These results show that $\sigma$ varies in the expected direction with T and $\mu_P$. Normalizing Langmuir's[6] value of $\sigma_m$ to match our value of $\sigma_m = 1.95 \times 10^{14}$ atoms/cm$^2$, one can compare his curve for a polycrystalline wire with our single plane (110) results. Figure 17 shows that for identical values of $\mu_P$ and T the (110) plane has a higher coverage than the polycrystalline wire. This result, which indicates an enhanced binding of Cs to the (110) plane is not unexpected since earlier field emission studies[3] had shown that the (110) plane possessed a higher binding energy and hence, a larger than average local coverage particularly in the low coverage region.

From the data of the sort shown in Figure 17, one may employ Equation (5) at constant coverage to obtain isoteric heats of adsorption H. Because of the limited range of $\mu_P$ (or P) accessible in our experimental arrangement, we were unable to employ Equation (5) to obtain meaningful values of H. However, the data generated indicates that this method of measuring single crystal heats of adsorption is feasible provided that the pressure is sufficiently low to eliminate scattering of the electron beam and also, in the case of metallic vapors, to prevent tube shorting.

Cesium on the (221) Plane of Aluminum (RPT). -Thermal desorption activation energy measurements for the the Cs-Al (221) system were attempted under zero pressure conditions in the RPT. The melting point of Al ($933^\circ$K) limited the temperature range over which the measurements could be made to the interval $720^\circ$K - $870^\circ$K. In this temperature range, Cs was not completely removed from the crystal, therefore the lowest coverage for which measurements were made corresponded to $\theta_f = .15$ (obtained from Figure 11). The activation energy obtained from the slope of the Arrhenius plots was 0.907 eV, and the value of the intercept, $\log \mathcal{V}$ was 3.22. These values are considerably

44
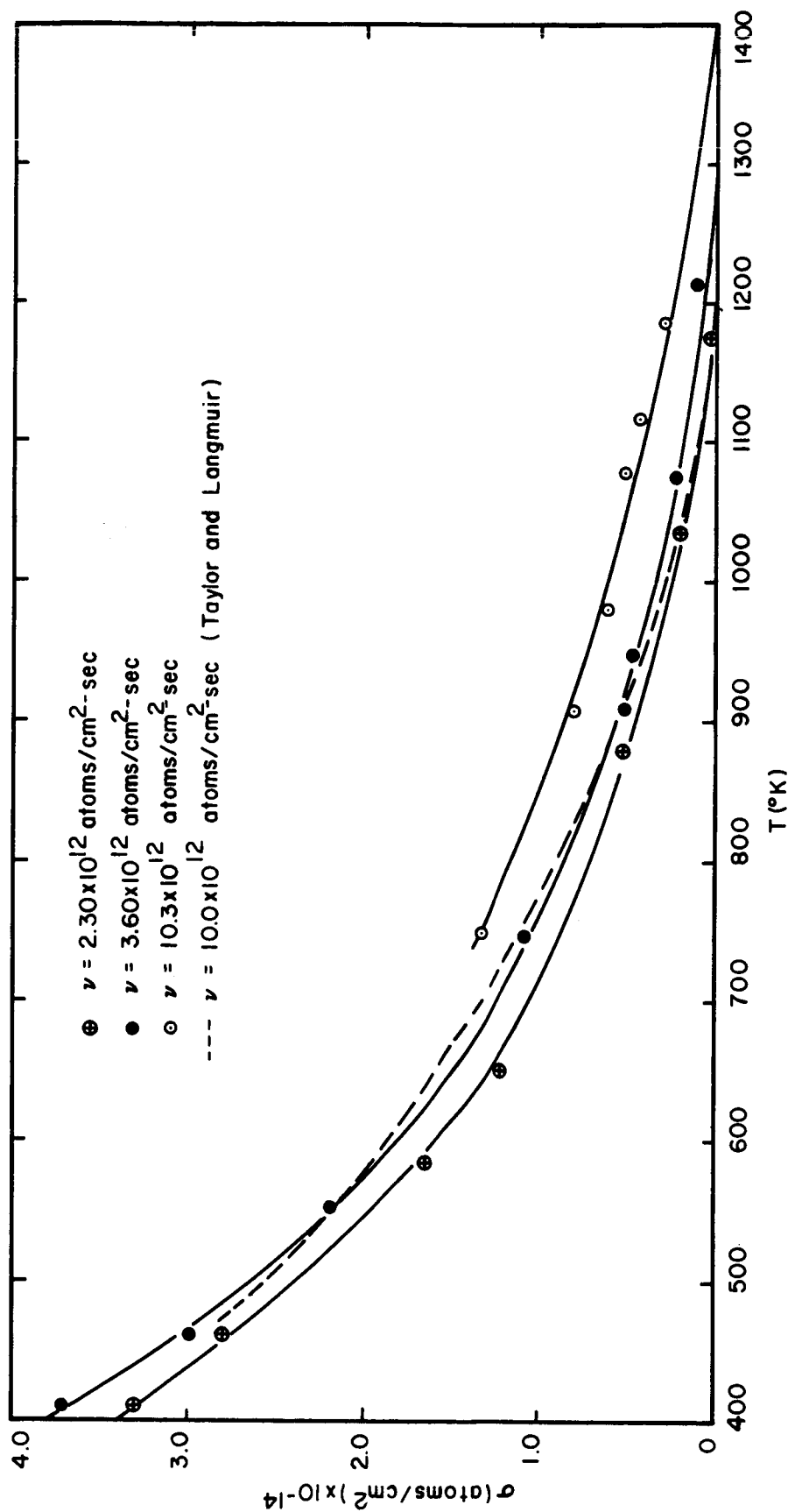
Figure 17. Experimental curves showing Cs coverage versus substrate tempera-
ture for the Cs-W(110) system at various steady state impingement
rates. Dashed line is obtained from Taylor and Langmuir's results
for polycrystalline W.

45

lower than the corresponding values for desorption energies for other substrates.

One possible explanation for the low values of energy is that diffusion from unequilibrated portions of the crystal complicates the measurements of desorption energy. Our procedure infers that no net diffusion of Cs out of the region being measured takes place during the desorption times, therefore, the entire crystal surface (not just the front side) must be equilibrated. To verify this assumption for our case, one must determine the concentration distribution on the back side of the crystal as a function of time.

Assume that the dosing arrangement is such that impinging Cs atoms establish a constant concentration on the front face and along the crystal edges. In cylindrical coordinates, diffusion takes place in planes perpendicular to the axis and the lines of flow are radial. The concentration distribution across the back side of the crystal may be obtained from the diffusion equation:

$$\frac{\partial \sigma}{\partial t} = D \left[ \frac{\partial^2 \sigma}{\partial r^2} + \frac{1}{r} \frac{\partial \sigma}{\partial r} \right] \tag{20}$$

where $\sigma$ is the concentration as a function of radius and time $t$, and $D$ is the diffusion coefficient. Assume that at $t = 0$, the concentration of Cs on the back side of the crystal is zero while the concentration at the edge $r = r_o$ is maintained at some constant value $\sigma_c$ for $t > 0$. Applying these boundary conditions leads to a solution in terms of Bessel functions of the first kind of order zero and one:

$$\frac{\sigma}{\sigma_c} = 1 - \frac{2}{r_o} \sum_{n=1}^{\infty} \exp(-D a_n^2 t) \frac{J_o(r a_n)}{a_n J_1(r_o a_n)} \tag{21}$$

where $a_n$ are the positive roots of $J_o(a r_o) = 0$. A plot of $\sigma/\sigma_c$ vs $r/r_o$ for various values of $Dt/r_o^2$ shows that $\sigma/\sigma_c \geq 0.98$ for all values of $r/r_o$ when $Dt/r_o^2 = 0.8$. Using the temperature and coverage dependent diffusion

46

coefficient $D = D_o \exp(-E_d/kT)$ one can express the equilibration time as a function of temperature:

$$\log t = E_d/2.3kT + \log(0.8r_o^2) - \log D_o \qquad (22)$$

The values of diffusion energy, $E_d$ and $D_o$ for the Cs-W system have been determined experimentally[3] and when used in Equation (22) result in the curves shown in Figure 18. It is readily apparent from Figure 18 that even at very low coverage, equilibration time ranges from $10^3$ to $10^5$ seconds in the temperature range of interest ($750-900^\circ$K).

The above analysis shows that the equilibration times are excessively long, thus the energy calculated from the Arrhenius plots, $E_d = 0.907$ eV corresponds to a diffusion energy rather than a desorption energy.

Cesium on the (10$\overline{1}$0) Plane of Titanium. - Although the Ti crystal was half the diameter of the Al crystal, one can apply the same arguments as above to show that equilibration difficulty and accompanying concomitant diffusion and desorption make it difficult to measure desorption energies. Surface equilibration effects were determined by depositing a small amount of Cs ($\theta = 0.11$) onto the Ti crystal at $77^\circ$K then heating below the desorption temperature at successively higher temperatures and monitoring the work function changes. One would expect $\Delta\emptyset$ to decrease uniformly when the front face of the crystal is equilibrated and diffusion is occurring only on the back side of the crystal. The fact that $\Delta\emptyset$ increased from 0.8 eV at $77^\circ$K to 1.37 eV at $340^\circ$K shows that the front face of the crystal is not equilibrated at temperatures below $340^\circ$K. Increasing the temperature further caused $\Delta\emptyset$ to decrease in the expected way until complete equilibration of the back side of the crystal had taken place. Although the long equilibration times made it difficult to obtain desorption energies from Arrhenius plots, it was possible to get an estimate of the desorption energies from the temperatures $T_d$ required to desorb a given coverage from an equilibrated surface in ten second heating times. The plot of $T_d$ vs $\theta$ is shown in Figure 12. The $T_d$ curve shows the large range of desorption

47
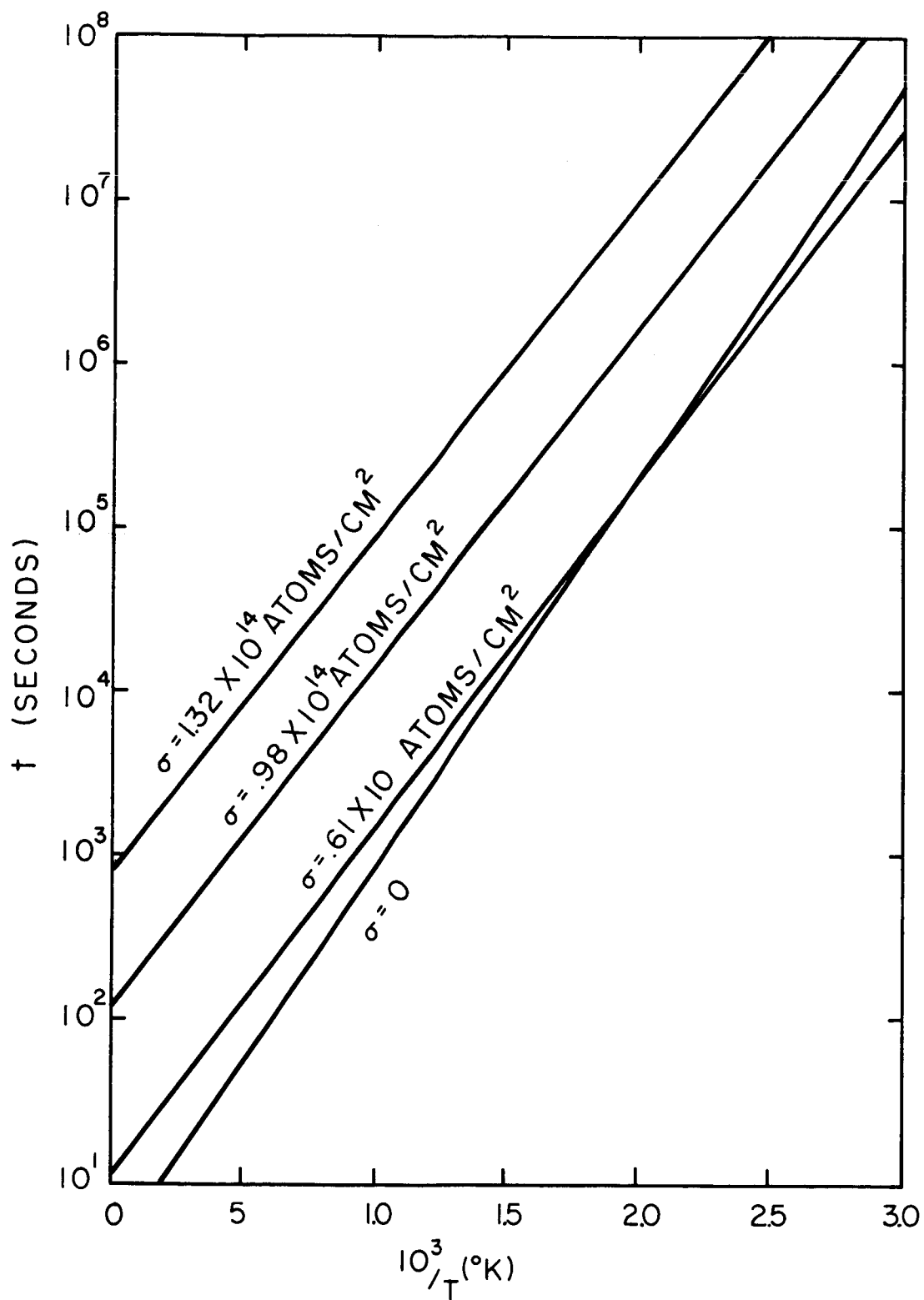
Figure 18. Equilibration time as a function of temperature for a .200 inch diameter disk for various degrees of Cs coverage.

temperatures associated with Cs on Ti in the monolayer region; this behavior is similar to that of Cs on other substrates. Assuming that the desorption activation energy is proportional to the desorption temperature yields a variation in desorption energy from 2.2 eV for terminal desorption to 0.7 eV at monolayer coverage. No bias was applied to the collector to return ions, during the desorption; therefore $E_a$ is the terminal desorption energy measured.

In previous work[2] it was shown that thermal desorption energies of Cs at zero coverage for several substrates followed an empirical relationship between activation energy of neutral desorption and average substrate work function $\emptyset_s$ of the form:

$$E_a = 2\emptyset_s - 6.0 \text{ eV} \qquad (23)$$

Substituting into empirical relationship, Equation (23), it is possible to obtain a value $\emptyset_s = 4.1$ eV for the $(10\bar{1}0)$ plane of Ti. This value is low when compared with the 4.42 eV value obtained from the analysis of the $\emptyset$ vs $\sigma$ data. Although the retarding potential characteristics of this surface were stable and reproducible, it should be re-emphasized that the surface was probably contaminated with oxygen; therefore, the values of $\emptyset_s$ obtained here are not necessarily for a clean Ti $(10\bar{1}0)$ surface.

## OXIDE CATHODE STUDIES

### INTRODUCTION

Although the oxide cathode was discovered over 60 years ago,[23] there are many facets of its operation that are not yet completely understood. For example, the influence of residual gases upon oxide cathode emission was recognized early,[24] yet even quite recently agreement upon whether certain gases increase[25, 26] or decrease[27] emission had not been reached. Other facets, such as sputtering of the oxide cathode,[28] are perhaps better understood but have not been investigated quantitatively. The present work was

49

undertaken to investigate certain phenomena in the two areas mentioned above, namely, the activation or deactivation of the oxide cathode by such gases as $O_2$ and $H_2$, and the sputtering of the oxide cathode by rare gas ions.

In recent years a number of studies have indicated that a hydrogen atmosphere may be beneficial to the operation of oxide cathodes. A study by MacNair[29] showed that both gas evolution was less and the emission properties were better for various types of oxide cathodes processed in an atmosphere of $H_2$ instead of vacuum. Garbe[30] examined the effect of ambient gases upon the emission properties of oxide cathodes in commercial tubes and found that exposure to hydrogen at $10^{-5}$ torr reduced noise and slightly improved emission. In the present investigation the effect of hydrogen on cathodes poisoned by oxygen was investigated.

## EXPERIMENTAL PROCEDURES AND RESULTS

The experimental tube for this study has an electrode configuration identical to that of the RPT design used in the Cs adsorption studies (see Figure 2), with a zone-melted Mo single-crystal emitter and a zone-melted polycrystalline Ni collector upon which alkaline earth carbonates were coated to form the oxide-coated cathode. The Mo block was mounted on a W filament so that it could be heated conductively; the Ni block (0.140 in D) was mounted on a four-wire Ni filament so that its temperature could be calibrated (with the aid of an optical pyrometer) as a function of filament resistance. In a preliminary experiment the tube was first evacuated and the tube elements were well outgassed without the oxide coating so that the heating and emission characteristics of the clean electrodes could be obtained.

The coating composition used is known commercially as C-10, which according to Sandor[31] is one of the more stable emitters. In this composition the mixing ratio of the three carbonate components is, when expressed in percent of weight:[31]

$BaCO_3$ . . . . . . . . . . . . . . . 57. 2%p. w.

$SrCO_3$ . . . . . . . . . . . . . . 38. 8%p. w.

$CaCO_3$ . . . . . . . . . . . . . . 4. 0%p. w.

The carbonates were obtained from Electro-Space Products, Inc. , and contained less than 100 ppm impurities. The dry carbonate powder was mixed with the binder and carrying solution in the following proportions:

1. 0 gm . . . . . . . . . . . . . C-10 powder

1. 4 m$\ell$ . . . . . . . . . . . . . amyl acetate

1. 0 m$\ell$ . . . . . . . . . . . . . . nitrocellulose in amyl acetate

The mixture was painted with a fine camel's hair brush directly onto the Ni substrate, resulting in a coating about 2. 5 mils in thickness and that looked very smooth and regular under x 10 magnification. No ball-milling of the mixture nor baking in air was done at any stage.

The experimental work was performed with the experimental tube attached to a vacuum system (Figure 19) so that pressure changes could be monitored and gases added at will. The vacuum system was equipped with a Varian Model 974-0035 Partial Pressure Gauge, a ground glass valve, and $O_2$ and $H_2$ sources. The partial pressure gauge monitored changes in the environment of the cathode during the activation and poisoning procedures, although unfortunately it could not be arranged in direct line of sight of the oxide coating. The ground glass valve separated the manifold from the mercury diffusion pump so that a given pressure could be maintained. The $O_2$ source was a thin silver tube which admitted oxygen into the vacuum when heated. The hydrogen source consisted of Pd and Zr filaments that had been loaded with $H_2$ in a hydrogen bell jar before installation on the vacuum system.
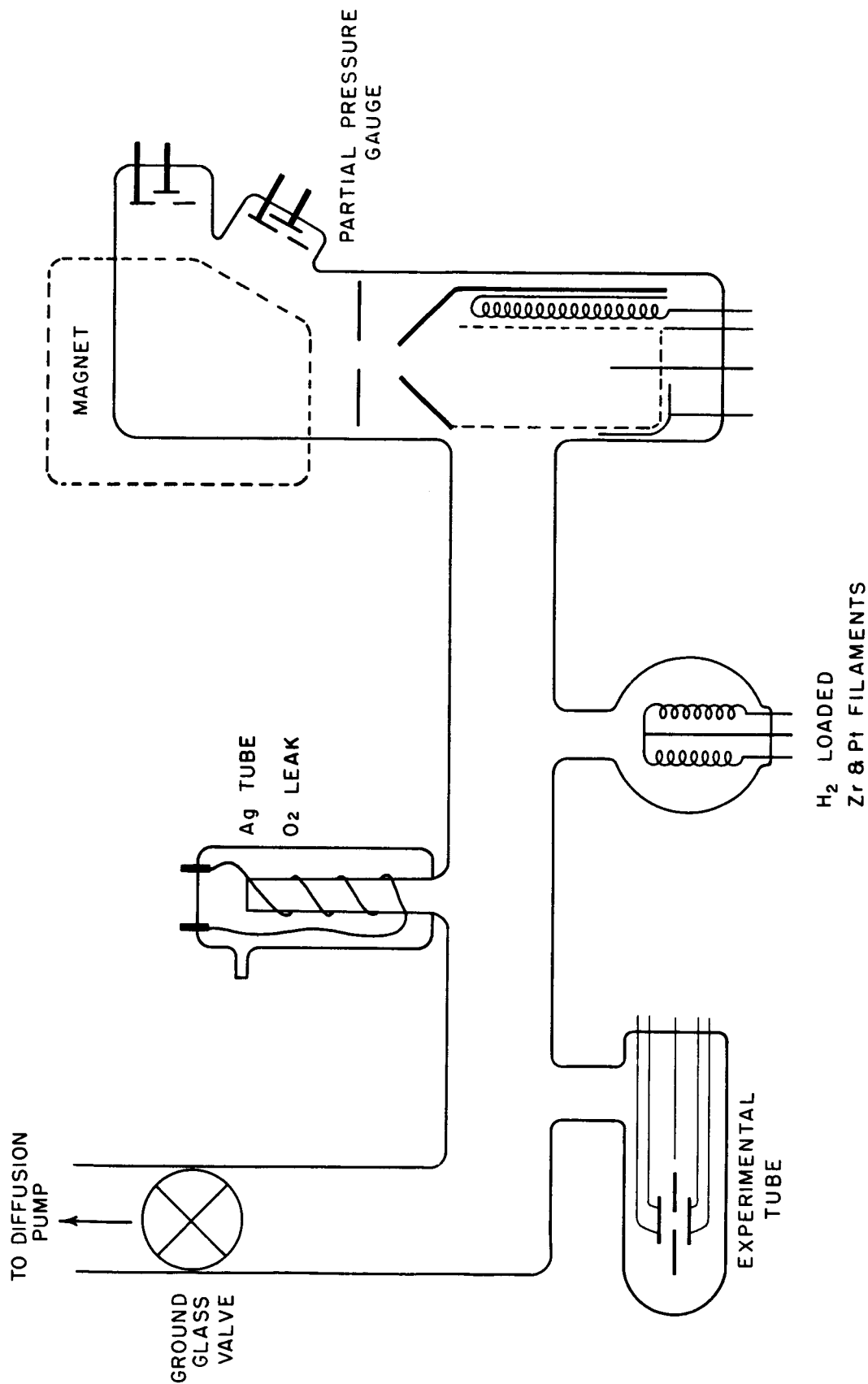
Figure 19.  Schematic diagram of the experimental arrangement on the vacuum system for the oxide cathode studies.

Activation Procedure and Results. - After application of the carbonate coating the experimental tube was evacuated and baked at $400^{\circ}C$ to obtain a background pressure of $3 \times 10^{-10}$ torr. The activation of the cathode was performed by heating the cathode to increasingly higher temperatures while keeping the tube pressure below $10^{-6}$ torr. A positive voltage of 120 volts was applied to the anode during the activation so that electron emission was drawn at the higher temperatures, which according to Nottingham[32] inhibits the loss of the electropositive elements and increases their concentration within the coating. The activation schedule followed is given in Table IV; the short times involved are indicative of a relatively quick conversion from the carbonates to the oxides. The major constituent causing the pressure increase throughout the activation period was CO.

TABLE IV

Activation Schedule for C-10 Composition
Oxide Cathode

| Time | Temperature | Total Pressure | Emission Current |
|---|---|---|---|
| 0 min | $835^{\circ}K$ | $2 \times 10^{-7}$ torr | $10^{-9}$ A |
| 30 | 835<br>865 | $1 \times 10^{-7}$<br>$7 \times 10^{-7}$ | |
| 80 | 865<br>950 | $5 \times 10^{-8}$<br>$2 \times 10^{-7}$ | |
| 100 | 950<br>1235 | $1.5 \times 10^{-8}$<br>$8 \times 10^{-7}$ | $5 \times 10^{-7}$ |
| 102 | 1235 | $4 \times 10^{-7}$ | $5 \times 10^{-6}$ |
| 104 | 1235 | $2 \times 10^{-7}$ | $1.6 \times 10^{-4}$ |
| 106 | 1235 | $5 \times 10^{-8}$ | $2.3 \times 10^{-4}$ |
| 110 | 1235<br>1286 | $5 \times 10^{-8}$<br>$1.4 \times 10^{-7}$ | $3.9 \times 10^{-4}$ |
| 113 | 1286 | $1.5 \times 10^{-7}$ | $2 \times 10^{-3}$ |
| 115 | 1286 | $1.5 \times 10^{-7}$ | $6 \times 10^{-3}$ |
| 119 | 1286<br>1306 | $1.5 \times 10^{-7}$<br>$2.0 \times 10^{-7}$ | $1.3 \times 10^{-2}$ |
| 128 | 1306 | $1.2 \times 10^{-7}$ | $1.34 \times 10^{-2}$ |

A Richardson plot for the activated cathode (Figure 20) yields a work function of 1.4 eV and a preexponential term of 0.035 $A/cm^2 deg^2$. Stable emission was drawn repeatedly at the 300 $mA/cm^2$ level, the limitation being due to space charge and the circuitry of the experiment but not due to the cathode itself.

Discussion of activation. - The ultrapure Ni (less than 40 ppm metallic impurities) used as the substrate in the present work is considered a passive base, since it has none of the impurities (such as Mn, Si, Ti or Mg) normally used as reducing agents.[32] However, the 400°C bake decomposes the nitro-cellulose binder, leaving some finely dispersed carbon which can reduce a small amount of the BaO to provide some free Ba (likewise for Sr).[32] The carbon also reacts with $CO_2$ to form CO, which is the primary constituent in the pressure rise during activation. Except for the above reaction, the activation of the cathode is due to temperature alone and thus does not require the long times necessary for chemical activation.

Recent studies of vacuum-activated pure Ni-based oxide cathodes have reported emission levels below 250 $mA/cm^2$ as the maximum obtainable,[29] and a limited life of 300-500 hours[29,33] due to depletion of the carbon activator.[33] The emission obtained from the cathode described here was slightly better (300 $mA/cm^2$); no attempt was made to measure its life.

RPT operation. - An attempt was made to use the retarding potential method to determine the work function of the oxide coating independently of its electron emission. First, the Mo block was used as the electron emitter, and the oxide-coated Ni block was used as the electron collector. When the oxide-coated Ni was at room temperature, the collected current at a given collector voltage kept changing with time, indicating a change in the surface potential of the oxide coating. This is caused by the low conductivity of the oxide coating at low temperatures.[32] At higher temperatures electron emission from the oxide coating prevented accurate measurement of the collected current. Thus the work function of the oxide coating could not be determined directly by the retarding potential technique.

54
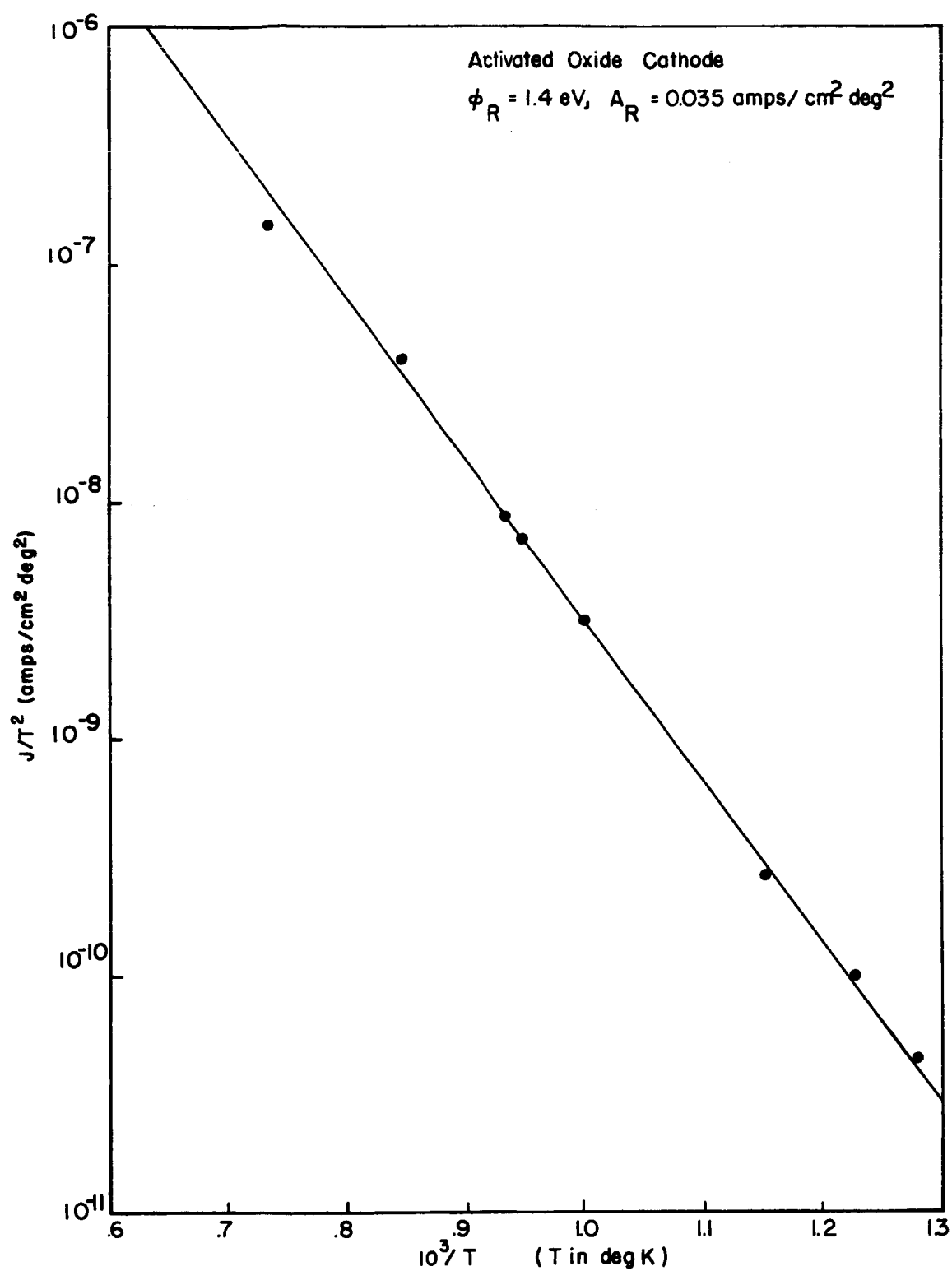
Figure 20. Richardson plot of electron emission from the activated oxide cathode as a function of temperature.

The connections to the triode were then reversed, making the oxide-coated Ni the electron emitter and the Mo block the collector, in an attempt to obtain the work function of the oxide coating from the potential difference between the two as indicated by the knee of a retarding potential curve. However, the Ni filament on which the Ni block was mounted had a long thermal time lag which interacted with the emission regulator circuit to cause a cyclic temperature change of the cathode and thus a cyclic emission change that prevented accurate measurements. Thus the tube was subsequently operated simply as a diode and changes in emission as functions of gas pressure or temperature noted.

Oxygen poisoning. -The effects of $O_2$ upon the electron emission of the oxide cathode has been examined as a function of cathode temperature and total pressure; the data in Figure 21 for $970^{\circ}$K are typical of the results obtained. When $O_2$ was admitted to the system by closing the glass valve and heating the oxygen leak, the emission current dropped to zero (i. e. , below $1 \times 10^{-9}$ A) as the total pressure rose above $10^{-6}$ torr. After the oxygen leak was turned off, the emission began to recover somewhat (to a level about three decades below its initial level), even though the total pressure remained high. During the beginning of this period, the partial pressure gauge showed a rapid disappearance of the $O_2$ peak, indicating a displacement of other gases from the electrodes and tube walls by $O_2$. At this point the original emission could be restored completely by heating the cathode to about $1350^{\circ}$K for approximately 2 minutes. This general behavior was observed at emission currents up to 2 mA (cathode temperatures up to $1130^{\circ}$K) and for pressures between $10^{-6}$ and $10^{-4}$ torr. At higher temperatures some reactivation occurred; at lower pressures oxygen had negligible effect.

Hydrogen was admitted to the system to investigate its effect on the $O_2$-poisoned oxide cathode. The second part of Figure 21 shows the effect of $H_2$ on the partially recovered emission obtained after the $O_2$ leak had been turned off; the emission again drops to zero and again recovers partially after the $H_2$ filament is turned off. (Heating the cathode to $1350^{\circ}$K restores

56
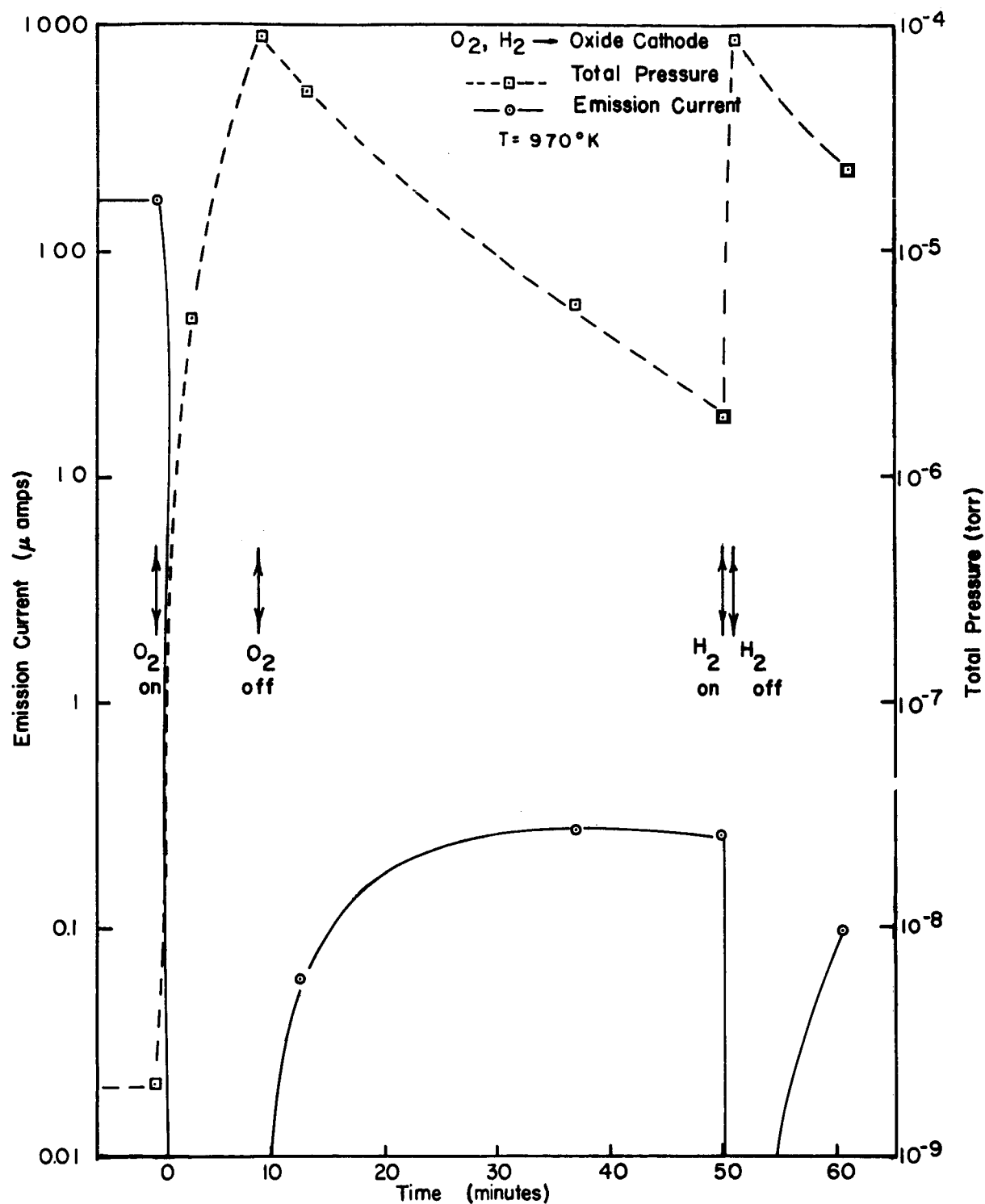
Figure 21. Electron emission and total pressure as functions of time, illustrating the effects of adding $O_2$ or $H_2$ to the system.

completely the original emission level.) In general, the addition of $O_2$ either in the presence of $H_2$ atmosphere or not, first reduced the emission level to zero, the emission recovering partially after the $O_2$ leak was turned off. These results were independent of the order or amount of $H_2$ and $O_2$ admitted to the system, within the limits noted above.

The reduction of emission due to the presence of hydrogen is somewhat surprising in view of Garbe's work with commercial tubes[30], in which he noted a slight improvement in emission. The difference may be in the type of reducing agent involved in converting the BaO to free Ba; for the pure nickel the only reducing agent is carbon from the nitrocellulose binder, whereas the commercial Ni bases contain many metallic impurities which can act as reducing agents. The fact that, following $O_2$ poisoning, the emission could be restored by heating alone suggests that the process is dominated by $O_2$ adsorption and desorption, and that effects due to irreversible chemical changes, if they exist, are small. One would expect the oxygen to interact with the carbon to produce CO; removal of carbon by this method would tend to shorten cathode life.

## Sputtering by Helium Ions

Helium was chosen as the gas to be ionized to avoid the complication of possible chemical reactions or work function changes due to adsorbates. The helium was admitted to the tube where it was ionized by electron emission from the Mo block. The maximum ion energy was determined by the difference in potential between the anode and the oxide cathode, and the effect of sputtering was determined by the change in oxide cathode emission current at constant temperature. After sputtering, the cathode was heated to $1350^{\circ}K$ to restore the emission. The data so obtained are listed in the following table.

TABLE V

Effect of $He^+$ Bombardment on C-10 Oxide Cathode Emission at $1270^{\circ}K$

| $He^+$ | | Emission | | |
|---|---|---|---|---|
| Energy | Approximate Density | Before Bombardment | After Bombardment | After Heating to $1350^{\circ}K$ |
| 170 eV | $4.5 \times 10^{15}$ ion/cm$^2$ | $3.2 \times 10^{-4}$A | $1 \times 10^{-4}$A | $2.2 \times 10^{-4}$A |
| 500 eV | $3 \times 10^{17}$ ion/cm$^2$ | $2.2 \times 10^{-4}$A | $4 \times 10^{-6}$A | $8.2 \times 10^{-5}$A |

58

At both ion energies the emission dropped as a result of $He^+$ bombardment and was only partially restored by heating. Heating to temperatures higher than $1350^{\circ}K$ decreased the emission still further. Thus there was a permanent change in the oxide coating due to $He^+$ bombardment, probably due to a removal of the oxide coating by sputtering. Unfortunately the Mo support filament burned out and prevented further measurements.

## STUDIES OF ELECTRON BOMBARDMENT
## OF ADSORBATES ON TUNGSTEN

### INTRODUCTION

There are several reasons for the recently increased interest in the interaction of low energy electrons (20-300 eV) with adsorbed layers. For example, information gained from such studies contributes significantly to our understanding of the basic physical mechanisms of adsorption. . Of more practical interest is the increased understanding of gas release in high vacuum tubes involving electron impact on glass or metal surfaces. Thus far, studies of electron interaction with adsorbed layers have been confined primarily to metal surfaces with electronegative adsorbates.[9-11, 34, 35] For these systems, electron induced desorption is thought to be caused by electron excitation of the adsorbate into an excited ionic or repulsive molecular state from which desorption can occur. The rather low cross-sections measured for electron induced desorption is attributed to the rapid electron exchange between the adsorbate and the substrate which allows transition to the ground state before desorption is complete.

Regarding electropositive adsorbates, studies of the electron induced desorption of barium[11] and cesium[3] from tungsten show that no measurable desorption occurs. This is not unexpected in view of the rapid transition of bonding electrons between the electropositive adsorbate valence level and the Fermi sea of the substrate for metallic adsorption

It is not obvious, however, from existing knowledge what one might expect from electron bombardment of a coadsorbed system containing both electro-

59

positive and electronegative elements such as cesium and oxygen. Interest in gaining more information about the surface bonding of coadsorbed species coupled with the knowledge that coadsorption particularly with oxygen is normative in many practical situations has motivated this study of electron interaction with coadsorbates on tungsten.

There are several approaches one can use for studying electron bombardment induced surface interactions. Redhead[10] and Lichtman[9,34] collected and measured the desorption products, while Menzel and Gomer[11] and Zingerman and Ishchuk[35] measured changes in the residual gas layer. Redhead bombarded an oxygen-covered molybdenum ribbon with electrons, then energy analyzed the resulting ion current. Lichtman, using a very sensitive mass spectrometer analysis, was able to detect, identify and measure both ion and neutral desorption products of carbon monoxide on molybdenum. Gomer, using field emission methods, measured the changes in the residual coverage after electron bombardment of a tungsten tip with various initial coverages of oxygen, hydrogen, barium or carbon monoxide.

Our experimental technique is similar to that of Gomer, in that a tungsten field emitter is used as the substrate. This method offers the advantage that cross-sections for desorption can be determined directly from changes in emission characteristics from a well-defined micro-surface area.

## METHOD OF APPROACH

Maximum cross-section for electron induced desorption can be determined from the following kinetic arguments.[11] For a given surface coverage $\sigma_j$ of species j, the following first order reaction for the rate of coverage change for an electron flux $N_e$ is given by

$$- d\sigma_j/dt = N_e b_j \sigma_j \qquad (23)$$

where $b_j$ is the cross-section in $cm^2$ if the units of $N_e$ are electron/$cm^2$/sec. The above equation can be integrated to yield the following expression for

the cross-section in $cm^2$:

$$b_j = \frac{3.68 \times 10^{-19}}{J} \log \left[ \frac{\sigma_j(0)}{\sigma_j(t)} \right] \qquad (24)$$

where $J$ is the current density in $A/cm^2$ and $\sigma_j(0)$ and $\sigma_j(t)$ refer to coverages of state $j$ at times $0$ and $t$ respectively. Values of work function change $\Delta\emptyset$ obtained directly from field emission I(V) data analyzed according to the Fowler-Nordheim (FN) Equation (8) may be used to determine $\sigma_j$ from previously established $\emptyset$ $(\sigma_j)$ relationships. If we assume

$$\emptyset = \emptyset_\infty + C_j \sigma_j \qquad (25)$$

where $\emptyset_\infty$ is the work function when $\sigma_j = 0$, and $C_j$ is a constant Equation (24) becomes

$$b_j = \frac{3.68 \times 10^{-19}}{J} \log \left[ \frac{\emptyset_i - \emptyset_\infty}{\emptyset_t - \emptyset_\infty} \right] \qquad (26)$$

In view of the fact that the Fowler-Nordheim preexponential $A$ varies with coverage as follows:

$$A = A_o e^{-g\sigma_j} \qquad (27)$$

where $g$ is roughly constant for adsorbates of low polarizability, it follows that Equations (24) and (27) can be combined to give

$$b_j = \frac{3.68 \times 10^{-19}}{J_t} \log \left[ \frac{\log A_i / A_\infty}{\log A_t / A_\infty} \right] \qquad (28)$$

where $A_i$, $A_t$ and $A_\infty$ are, respectively, the F-N preexponential corresponding to times $0$, $t$ and $\infty$. Calculation of cross-section by both Equations (26 and (28) can be used to provide a check on self-consistency. Since the reference value of $A$ refers to the clean substrate $A_s$, it is convenient to

61

rewrite Equation (28) as

$$b_j = \frac{3.68 \times 10^{-19}}{J} \log \left[ \frac{B_i - B_\infty}{B_t - B_\infty} \right] \qquad (29)$$

where the subscripts have the same significance as above and $B = \ln A_s/A$.

## EXPERIMENTAL PROCEDURES

The experimental tube used for this work has been reported previously[3].
Briefly, it is a dual purpose probe tube, shown in Figure 22. In this tube
design the same set of electrodes are used at different times as the beam
forming electrodes for the bombardment beam and as Faraday collection
electrodes for emission from a small portion of the emitter. A thermionic
emitter and the Faraday collector of the probe can be used along with the
suppressor electrode element as part of the lens system to focus electrons
onto the emitter. This insures that the bombarding electrons strike the
emitting portions of the tip in a nearly uniform fashion.

The work function obtained from the Fowler-Nordheim analysis of the
total current I(V) characteristics of the tip are average values heavily
weighted towards the low work function crystallographic planes; hence, if
electron induced desorption causes the work function to decrease, the effect
will be measured whether or not the incident electron beam is uniform over
the tip. However, if the electron beam is nonuniform and the work function
increases, it is necessary to analyze the region of the surface where the
change occurs. The present tube arrangement assures the beam to impinge
uniformly over the surface; hence, total current measurements can be mean-
ingfully employed. The tube shown in Figure 22 has two sources, one of which
contains the usual cupric oxide-filled platinum bucket serving as an oxygen
source and the other a platinum platform upon which either cesium or mercury
is deposited. The tube was designed to be inserted into a liquid nitrogen
cryostat where the measurements were performed. Typically, the experi-
mental procedure was as follows: 1) the tip was dosed at $77^\circ$K with oxygen,
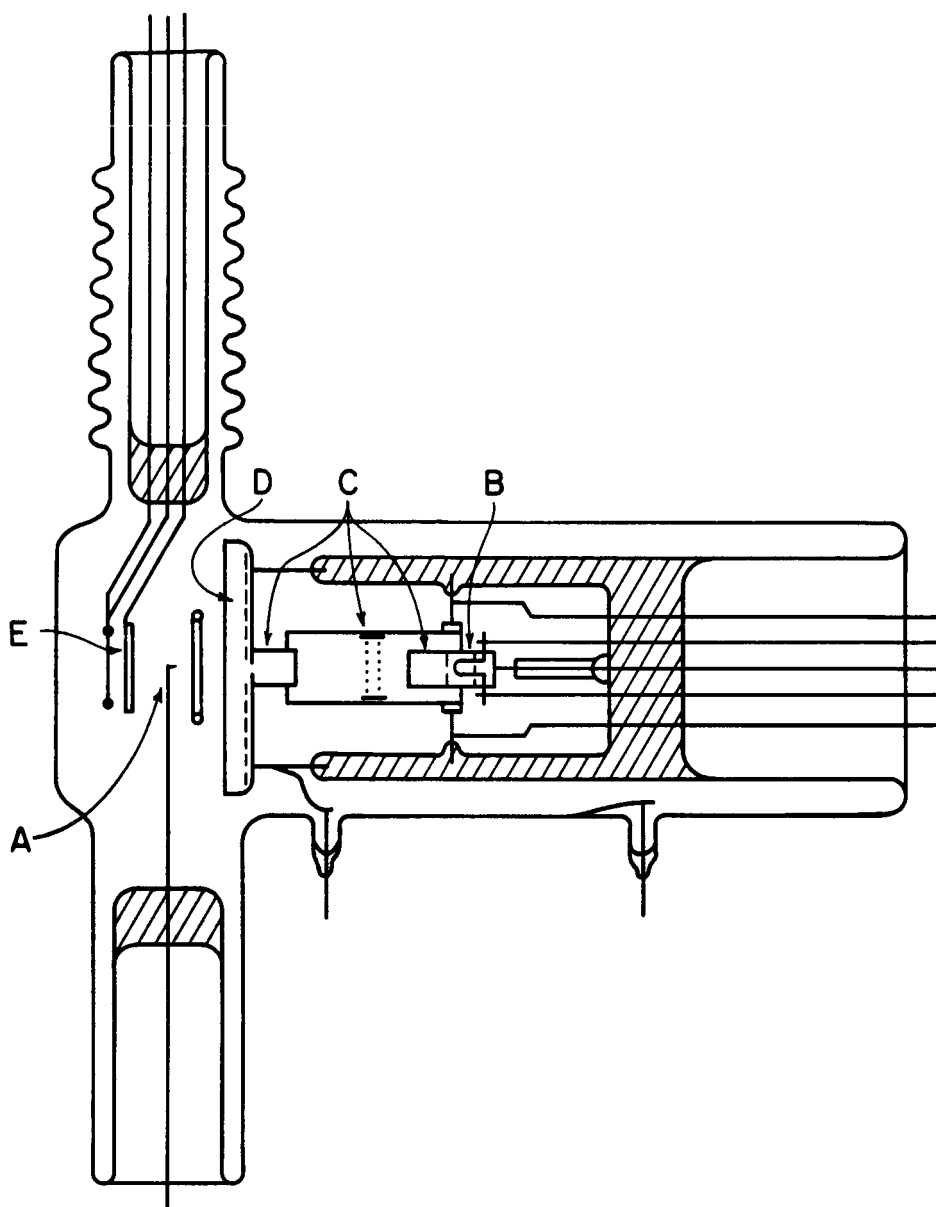
Figure 22. Electron desorption studies tube. A is a tungsten field emitter, B is a tungsten filament used as the electron source, C is a lens arrangement that can be used either to focus the electron beam or as a Faraday collector, D is a phosphor screen, and E is a collectₒ

2) the tip was then heated to thermally equilibrate the oxygen at $500^\circ$K,
3) either cesium or mercury was then deposited at $77^\circ$K and equilibrated
at 250 to $300^\circ$K, 4) the surface was bombarded with electrons with the tip
held at $77^\circ$K, 5) periodically the gun was turned off and the I(V) character-
istics of the emitter recorded.

The calibration of the electron beam at the emitter was determined for
several accelerating voltages. The tip assembly shown in Figure 22 was
replaced by a backup plate with a Faraday collector arrangement consisting
of a large plate with a 15 mil diameter aperture placed in the same position
as the emitter. Between the aperture and the Faraday collector, a plate with
a larger aperture was used as a suppressor to return secondary electrons to
the cup and the aperture plate. Knowing the total current collected and the
area of the small aperture, the current density at the same spatial position
as the emitter was obtained.

Originally the calibration was performed before the tip was inserted;[3]
subsequently, the filament of the gun had to be replaced resulting in a change
in the gun characteristics. This made it necessary to recalibrate the gun
after the electron desorption had been completed. It was then found that
current densities used for the electron desorption were lower by almost a
factor of 10 than the gun capability would allow at best focus condition. Table VI
shows the calibration of the current density at various electron energies.

TABLE VI

Relationship between the energy of the bombarding electrons and the current
density at the tip

| Bombardment energy (eV) | Current Density (ma/cm$^2$) |
|---|---|
| 250 | .605 |
| 200 | .351 |
| 150 | .176 |
| 100 | .062 |

Prior to dosing the tip, the gun was run for a slightly longer time than that required for the experiment to be performed. The contamination level of the tip due to operation of the gun alone could thus be determined. The operation time of the gun was then chosen to be sufficiently short to eliminate detectable work function change of the emitter surface due to spurious contamination. This established a minimum level of sensitivity for the detection of electron induced desorption.

## RESULTS AND DISCUSSION

### Oxygen-Tungsten System

Analyzing the work function change with time according to Equation (23), the cross-sections for the desorption of oxygen from tungsten at three different electron energies were obtained as given in Table VII.

### TABLE VII

Desorption cross-sections for oxygen on tungsten as a function of bombardment energy.

| Bombardment Energy (eV) | $\phi_i$ (eV) | Cross Section ($cm^2$) |
|---|---|---|
| 250 | 6. 43 | . 634 x $10^{-19}$ |
| 200 | 6. 34 | . 910 |
| 100 | 6. 22 | 3. 100 |

No desorption was detected for incident electrons less than 50 V because of the low current densities and a diminution of cross-section with decreasing electron energy.

A typical plot of the data according to Equations (26) and (29) is shown in Figure 23. From the slopes of such plots, cross-sections for desorption were calculated. The values of $\phi_\infty$ = 5. 72 eV and $B_\infty$ = 2. 20 were chosen to agree with previous measurements by Menzel and Gomer.[11] The values
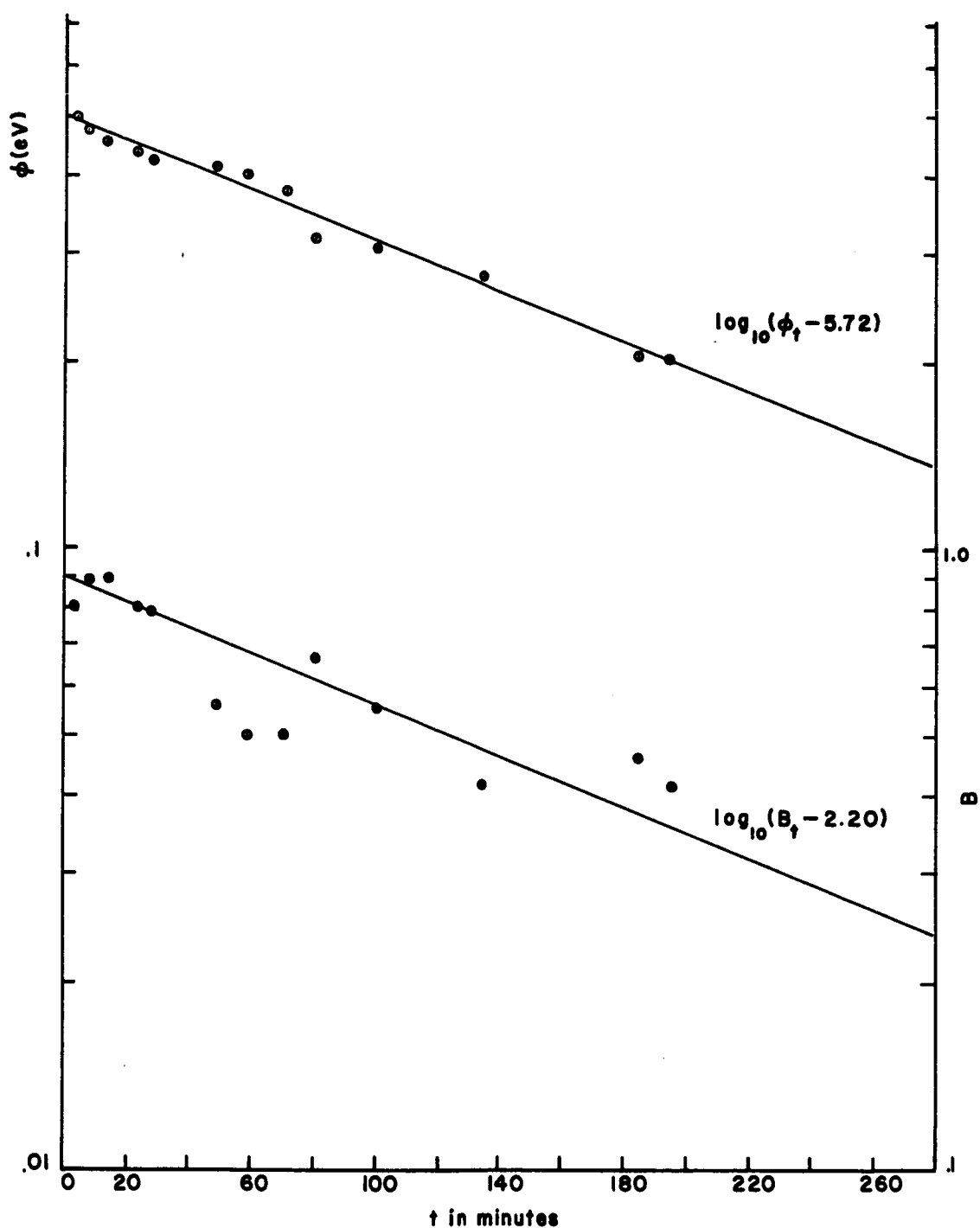
Figure 23. Work function changes and Fowler-Nordheim pre-exponential changes caused by bombarding an oxygenated W surface ($\phi_{0W}$ = 6.25 eV initially) with 100 eV electrons. The data is plotted according to Equations (26) and (29).

of $b_j$ in Table VII clearly exhibit a maximum at the primary electron energy of 100 eV in agreement with observations by Redhead[10] on the electron desorption of O from Mo. The cross-section value $b_j = 3.1 \times 10^{-19} cm^2$ for removal of the loosely bound state of O at 100 eV is in close agreement with the $4.5 \times 10^{-19} cm^2$ value obtained by Menzel and Gomer[11] for this system. For initial coverages of O corresponding to work functions less than 5.72 eV the cross-section for electron induced desorption is less than $2 \times 10^{-21} cm^2$ which, for the time scales and current densities used in this experiment, would be undetected.

Cesium-Oxygen-Tungsten System

Cross-sections were determined for the desorption of Cs by 250 V electrons on five different underlying O coverages corresponding to work functions of $5.38 \pm .01$, $5.53 \pm .02$, $6.03 \pm .03$, $6.42 \pm .02$ and $6.50 \pm .04$ eV. The results are summarized in Table VIII. The initial coverage of Cs on the various OW surfaces was established from previously[3] determined relationships.

The **results clearly show** a definite change in work function and the preexponential factor caused by the impingement of low energy electrons on this composite surface. Before proceeding further it is necessary to establish the mechanism leading to the work function change. First, it was found that heating the electron bombarded surface to the original Cs equilibration temperature did not restore the original pattern nor work function, thus ruling out a reversible change in state of the adsorbed complex. Several lines of evidence suggest that removal of O was not responsible for the work function change. First, throughout the coverage range the presence of O lowers the work function of the composite surface, hence, its removal should necessarily increase the work function. This however, was not always the case as seen by the Table VIII results. Secondly, for values of $\emptyset_{OW}$ less than 5.7 eV no perceptible desorption of O would be expected due to the exhaustion of the labile adsorbed state, yet changes in $\Delta\emptyset$ are registered for the composite system for $\emptyset_{OW} < 5.7$ eV.

## TABLE VIII

Summary of electron-induced desorption of Cs on O-W for 250 volt electrons at a current density of $6.05 \times 10^{-4}$ A/cm$^2$

| $\phi_{OW}$ (eV) | $\phi_{Cs-O-W}$ (eV) | $\Delta\phi$ (eV) | $\Delta \log A$ | Cross-Section $b_j \times 10^{20}$ (cm$^2$) | Coverage $\sigma$ (atoms/cm$^2$) $\times 10^{-14}$ |
|---|---|---|---|---|---|
| 5.38 ± .01 | 2.21 ± .01 | -.15 ± .01 | -.37 ± .03 | 1.37 ± .005 | .67 |
| 5.38 ± .01 | 1.11 ± .01 | -.01 ± .01 | .05 ± .06 | 1.18 ± .005 | 1.10 |
| 5.53 ± .02 | 3.95 ± .02 | .05 ± .02 | .03 ± .06 | .94 ± .006 | .24 |
| 5.53 ± .02 | 2.48 ± .01 | .13 ± .01 | .12 ± .04 | 1.33 ± .006 | .60 |
| 5.53 ± .02 | 1.98 ± .02 | .23 ± .02 | -.13 ± .05 | 8.63 ± .010 | 2.60 |
| 6.03 ± .03 | 5.05 ± .02 | -.06 ± .03 | -.12 ± .04 | .73 ± .002 | .30 |
| 6.03 ± .03 | 4.81 ± .02 | -.06 ± .03 | -.11 ± .05 | 1.20 ± .006 | .36 |
| 6.03 ± .03 | 1.89 ± .01 | -.25 ± .01 | -.27 ± .06 | 3.72 ± .006 | 2.00 |
| 6.42 ± .02 | 3.61 ± .02 | .07 ± .02 | -.11 ± .05 | .62 ± .006 | .72 |
| 6.42 ± .02 | 2.56 ± .01 | .09 ± .01 | -.02 ± .02 | .66 ± .004 | 1.02 |
| 6.42 ± .02 | 1.61 ± .01 | -.07 ± .01 | -.03 ± .09 | .67 ± .006 | 1.67 |
| 6.5 ± .04 | 1.97 ± .01 | -.26 ± .02 | -.37 ± .04 | 8.27 ± .008 | 2.50 |

It was found that redosing with Cs after electron desorption always re-
stored the original pattern and work function of the surface. This was found
to occur on both sides of the work function minimum where the sign of $\Delta \emptyset$
was reversed. We therefore conclude that Cs is the desorbing species re-
sponsible for the work function change during electron bombardment. The
values of $\Delta \emptyset$ were therefore converted to cross-sections for Cs electron
induced desorption by converting $\Delta \emptyset$ to $\Delta \sigma$ from the $\emptyset(\sigma)$ relationships for
the appropriate composite systems. The results show that cross-section
values for Cs desorption by 250 V electrons is negligible at low Cs cover-
ages, regardless of underlying O coverage, and increases with Cs coverage
to $8 \times 10^{-20} cm^2$. In view of the fact that no desorption of Cs was detected
for Cs on clean W throughout the coverage range, these results are rather
surprising and of considerable interest both from a practical point of view
and as they elucidate basic changes in the binding mode of Cs to the substrate.

The removal of Cs without disturbing the underlying chemisorbed O layer
parallels the behavior observed during thermal and field induced desorption.
According to the theoretical views set forth to describe electron induced
desorption,[11] electronic excitation to an excited state is followed by either
desorption or de-excitation to the ground state. Apparently the Cs-O bond
becomes electronically excited to a repulsive or unstable state in which re-
transitions to the ground state are sufficiently slow to allow desorption of
Cs.

In view of the fact that neither Cs or Ba on clean W undergo electron
induced desorption, we conclude that an important change in the character
of the surface bond of Cs is effected by the underlying O layer. The rapid
transitions of the delocalized bonding electrons for electropositive adsorbates
with small ionization potentials has been used to explain the near zero cross-
section for Ba and Cs on W. In addition, Menzel and Gomer[11] show theoret-
ically that the increased mass of Ba and Cs decrease the cross-section
relative to O for electron induced desorption by $10^3$. Thus the primary
effect of O on the binding mode of Cs must be a significant reduction of the

de-excitation transitions. It can be noted in the Table VIII results that, with only a few exceptions, the cross-section for electron desorption increases with increasing Cs coverage. Also in several cases at constant Cs coverage cross-sections are unaffected by varying the underlying O coverage. This re-enforces the conclusion that Cs is the desorbing species. One explanation of the increase in cross-section with Cs coverage is the possible lowering of the Cs binding energy which, according to Menzel and Gomer,[11] can cause an increase in $b_j$.

## The Mercury-Oxygen-Tungsten System

The high value of adsorbate ionization potential (10.2 V) for Hg may lead to a modified version of metallic adsorption in which the bonding electrons are more localized about the adsorbate. An indication of this stems from the formation of a negative dipole moment on adsorption of Hg on W[36] which results in an increase in work function. It was interesting therefore to examine the interaction of low energy electrons with the Hg/W and Hg/OW systems. The variation of work function with Hg coverage has been determined previously[36] and could be used as a measure of the amount of Hg removed by the low energy electrons.

The electron induced desorption of Hg was studied with 250 V electrons over the entire coverage range of Hg on W at 77°K. The results showed that no electron induced desorption or rearrangement of the Hg layer occurred. It could be concluded that cross-sections for electron induced desorption of Hg must be less than $1 \times 10^{-20} cm^2$.

With the presence of an underlying O layer on the W substrate, the adsorption of Hg resulted in a diminution of work function rather than an increase in work function as adsorbed on the clean substrate. In one experiment in which the initial work function of the OW surface was 5.2 eV, the adsorption of approximately 0.4 monolayer of Hg resulted in a work function decrease to 4.3 eV. The presence of an underlying O layer apparently causes a radical change in the binding of Hg to the surface and results in a positive dipole

moment. A further interesting effect of the underlying O layer was the re-duction of the temperature required to remove Hg from the surface. Whereas, for the clean surface desorption of Hg from W requires approximately $600^{\circ}$K, desorption of Hg from an OW layer whose initial work function was 5. 2 eV occurred at the low temperature of $300^{\circ}$K. These results, although very preliminary, suggest the HgOW system should be interesting for further study.

Again as in the case of the clean surface the interaction of 250 V electrons with a HgOW surface in which the initial work function was 4. 3 eV resulted in no perceptible change in work function. It was estimated, therefore, that cross-sections for rearrangement or removal of Hg by low energy electrons from a composite surface must be less than $1 \times 10^{-20}$ $cm^2$. Thus, we con-clude that Hg adsorbed on clean or oxygenated tungsten is relatively insensitive to the impingement of low energy electrons. Theoretically, overall cross-sections can be greatly reduced by increasing the mass of the adsorbate. Since Hg is a relatively high mass adsorbate, the results obtained are not totally unexpected.

## FIELD ION AND FIELD EMISSION MICROSCOPE INVESTIGATIONS OF SPUTTERING

### INTRODUCTION

The major factor presently limiting the operational lifetimes of both the contact ion thrusters and the electron bombardment thrusters is the erosion of the ion-accelerator electrodes due to sputtering by ion bombardment.[37, 38] Sputtering also plays an important role in other problems in space physics, such as the erosion of rocket nozzles, ion bombardment of missiles and satellites in the space environment, and the state of the surface of the moon due to solar wind bombardment. Sputtering is an important factor in other technical areas being emphasized at the present time; these areas include: (a) thin film physics in which sputtering is often used in the formation of thin films for electric components and circuits; (b) high energy physics, in

which sputtering is one of the mechanisms by which high energy bombardment causes radiation damage in solids; (c) plasma physics, in which sputtering is involved in the interaction of a plasma with the walls of its container; (d) surface physics, in which sputtering may be used to clean and smooth a surface as well as to roughen and contaminate it. Thus a more thorough understanding of the sputtering process would be helpful not only in the design of electron bombardment thrusters but to a number of other diverse areas.

Unfortunately, although physical sputtering is understood in a qualitative sense, the complex nature of the interaction makes quantitative prediction of results in a new situation extremely difficult.[39] Because of this, recent theoretical studies of sputtering have replaced the earlier analytical techniques[40-42] with computer simulation,[43-45] in which numerical integration of the classical laws of motion for all the atoms in a small crystal struck by a bombarding particle enable the detailed trajectories of individual atoms to be determined.[45] The results of such computer calculations can be compared with such experimental data as the yield (atoms/ion), angular and energy distributions of the sputtered particles, as determined by techniques that examine in some fashion the sputtered particles emitted by an ion bombardment target.[39,46] It should be possible to determine from the computer studies changes occurring in and on the target; these could be compared with direct examination of the target surface by field emission and field ion microscopy techniques. The high magnification and resolution of the field ion microscope permits the examination of sputtering-induced surface damage and interior defects in atomic detail. Consequently these techniques complement those in more general use.

Application of Field Ion Microscopy to Sputtering Studies

The field ion microscope, first conceived by Müller,[47] is a device of great interest and importance in the study of metal surfaces because of its ability to resolve individual atoms in a crystalline lattice. For its theory of operation and summaries of early experimental results, the reader is

referred to review articles by Müller.[48,49] Only a brief discussion of its operation will be given here.

The field ion microscope (FIM) is a diode, like the field emission microscope (FEM), but with the voltages reversed. Ions instead of electrons are used to form the image. In order to have a supply of ions, gas is introduced into the tube; the gas molecules are attracted to the neighborhood of the tip by their dipole interaction with the inhomogeneous electric field. In the high field near the tip the molecules become ionized, producing ions that travel to the phosphor screen and form an image of the surface of the point anode. Although the magnification of the field ion microscope is about the same as that of the FEM, the resolution is much greater because diffraction effects are less for ions than for electrons, and at the temperatures employed, the velocity components tangent to the surface of the point anode are less for ions. The resolution of the FIM is optimized by operation at low temperature, to reduce the transverse velocity components of the image-forming ions, and by the use of helium gas as the source of ions, since helium has the highest ionization potential of any gas and thus its ions are formed closer to the anode surface. By these means resolution of neighboring atoms 3 A apart has been attained.[48]

The FIM anode tip can be kept free of contaminants from the gas phase, if helium is used as the imaging gas, by maintaining a field of 300Mv/cm or higher on its surface; since all other gases have ionization potential less than that of helium, gas molecules other than helium will be ionized at a distance and will never reach the tip surface. At still higher fields (500 Mv/cm for tungsten) atom layers of the tip material are removed from the tip surface, permitting examination of successive underlying atom layers.[48]

Thus, the field ion microscope can be used advantageously in sputtering studies for several reasons: (1) Individual sputtering events may be examined. (2) Gross damage in the interior of the target crystal, as well as on its surface, may be examined in depth by removing atom layers from the anode tip by field evaporation. (3) The shape and structure of the target surface are known

73

in atomic detail. (4) Since the tip surface is approximately hemispherical in shape, all the crystallographic directions associated with the crystal structure of the target can be viewed in its field ion pattern; by rotating the tip about its axis different crystal faces may be exposed to the bombarding beam. (5) If a beam of neutral atoms is used as the bombarding beam, the surface of the target may be kept absolutely free of extraneous contaminants during bombardment, so that effects due to surface contamination are eliminated. The FIM also has some disadvantages associated with it, the most serious of which is the high value of mechanical stress, due to the electric field, which is exerted on the tip surface; this can affect the apparent results due to bombardment by permitting migration of some types of defects to the surface, and also limits the choice of materials from which targets can be made.

The application of the field ion microscope to studies of sputtering and radiation damage so far has been limited. We have examined Xe ion bombardment of W for energies between 100 and 1300 eV.[3, 50] Müller and Sinha[51] (also Brandon and Wald)[52] have observed surface damage resulting from bombardment of W and Pt tips with 5. 4 Mev alpha particles from a polonium source,[49] with He or A ions of energies between 25 and 300 eV,[49] and bombardment of W with 20 kev He or Hg atoms.[51] In their latter study they found that the surface damage due to He atoms consisted of vacancies, interstitials and clusters of these defects, and a disordering of the lattice in about a 50 to 100 A diameter region, with some of the damage appearing on the side of the tip opposite to the bombarding beam (tip radius of 900 A). Bombardment by Hg atoms caused even more extensive damage, permitting field evaporation of entire close-packed net planes up to 200 A in diameter.

Application of Field Electron Microscopy to Sputtering Studies

The field emission microscope, described in a previous section, has been used extensively in surface studies, because in it such pertinent parameters as substrate temperature, substrate surface electric field, and adsorbate

coverage may be varied over wide ranges. For this same reason the FEM is useful in sputtering studies even though its resolution (20 to 30 A) is not as good as that of the FIM; it may be used to investigate the effects of target temperature or of thin films upon target damage. So far little use has been made of the FEM in sputtering studies; Martin, et al. , [53] and Ehrlich and Hudda[54] have reported the sputtering of W by rare gas ions for which neither the energies nor the directions were well-defined.

## FIM STUDIES OF HE ION BOMBARDMENT OF W AND IR

An investigation in atomic detail of the surface damage and interior damage in tungsten caused by bombardment of a few Xe ions has been reported previously.[3, 50] One of the objectives of the present contract was to broaden the above study to include other rare gas ions and targets of different crystalline structure. In this section are presented the results of FIM investigations of He ion sputtering of clean tungsten and iridium.

### Experimental Tube and Techniques

Field ion microscope design. - A diagram of the field ion microscope used in this work is shown in Figure 24. The metal to be used as a target is etched in the form of a needle with a very small radius (100-500A) in order to obtain the high fields necessary for image formation at reasonable voltages (5-25 kV). The target needle is mounted by spot-welding it to a 10 mil tungsten loop, in order that the target may be heated controllably. The W loop is in turn mounted to a four-wire press so that the target temperature may be monitored. The tube envelope is fabricated from pyrex glass with a viewing screen diameter of 5 inches and a target to screen distance of 10 cm. Before applying the phosphor screen, a conducting layer of tin oxide is formed on the glass surface. The metal cone surrounding the target in the $Xe^+$-W study was found to be unnecessary and was replaced with a single loop ring, thus eliminating a possible source of contamination.
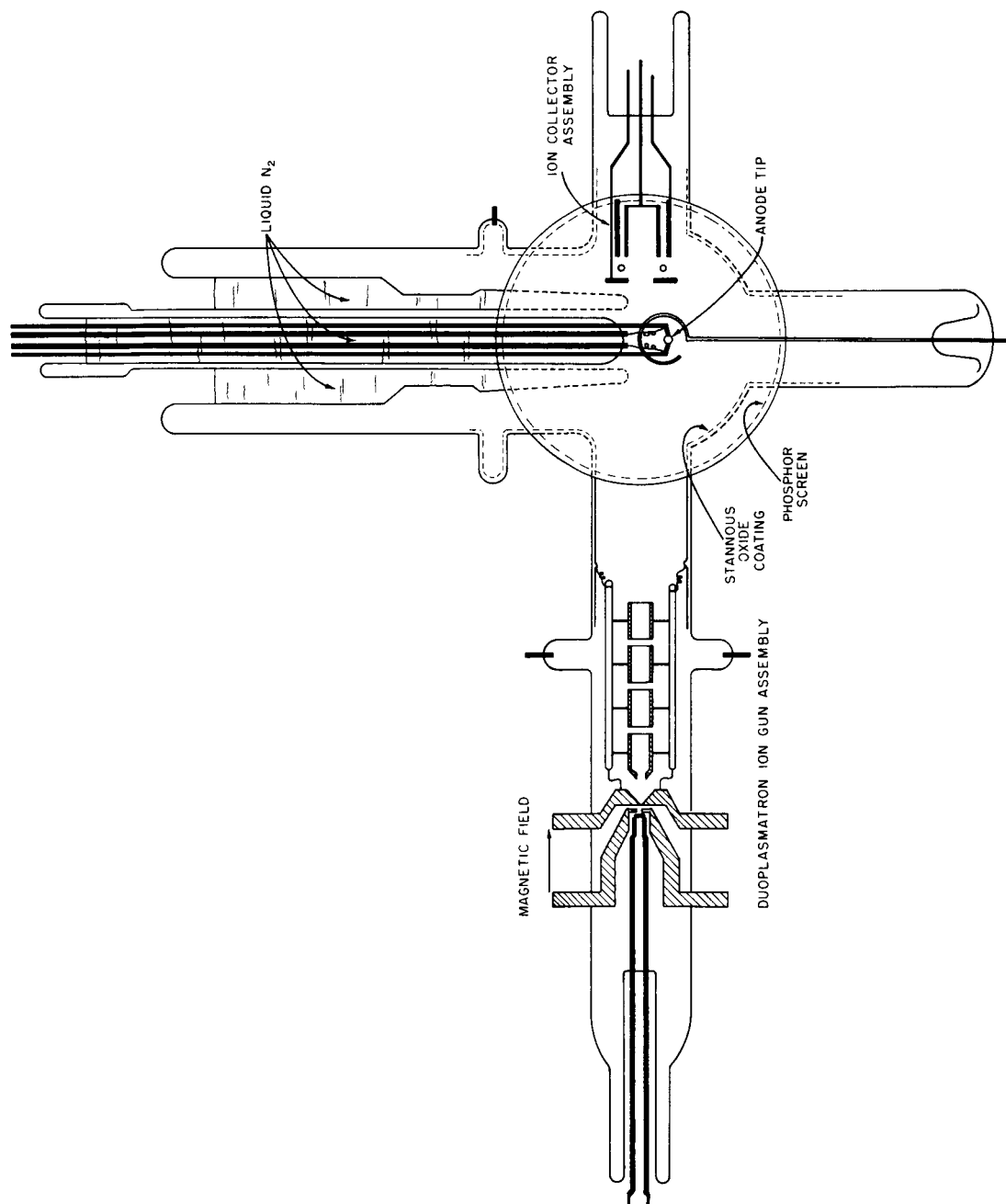
Figure 24. Schematic diagram of the field ion microscope used for helium ion sputtering studies.

Duoplasmatron ion gun design. - The ion source for the Xe ion bombard-
ment study was replaced with a new design in order to reduce some of the
contamination problems associated with the ion source operation. The new
ion source (Figure 25) is patterned after the duoplasmatron ion source de-
veloped by von Ardenne.[55] In this source a plasma is established between the
anode (C in Figure 25) and another elelctrode D by electron ionization of a gas
at relatively high pressure(30-100 $\mu$ torr). A solenoidal magnetic field between
C and D confines the plasma. An ion beam is drawn from the plasma through
a small aperture (0.005" D) in the anode by applying a high voltage (3-7 kV)
to an extractor electrode B positioned very close to the aperture. Because
of the small aperture in the anode, large pressure differential may be main-
tained between the ionizing region of the ion source and the main body of the
FIM tube, permitting the formation of an ion beam of sufficient current
density (1 $\mu$ A/cm$^2$) for our present purposes, while maintaining good vacuum
in the target area of the tube. A retarding potential analysis of a He ion beam
showed that the energy half-width of the ion beam was approximately 6 eV and
the beam potential was within 1 V of the applied potential over the range of
extraction and focusing voltages used in subsequent experiments.

Procedure. - The microscope was operated on a bakable, gas-handling,
mercury diffusion vacuum system. After sealing onto the vacuum system, the
tube was evacuated and baked overnight at 400$^o$C, resulting in a vacuum of
better than 10$^{-9}$ torr. During tube operation the target was kept at liquid N$_2$
temperature. The procedure used in these investigations was the following:

    (1) the tip of the metallic needle used as the target was first
         field desorbed in the presence of 4 $\mu$ torr of He imaging
         gas to obtain a smooth and clean W surface;

    (2) then 100 $\mu$ torr of He was admitted into the ion gun and
         the He in the FIM bulb was pumped out, while maintaining
         the high viewing field in the region of the tip to prevent
         any contamination;
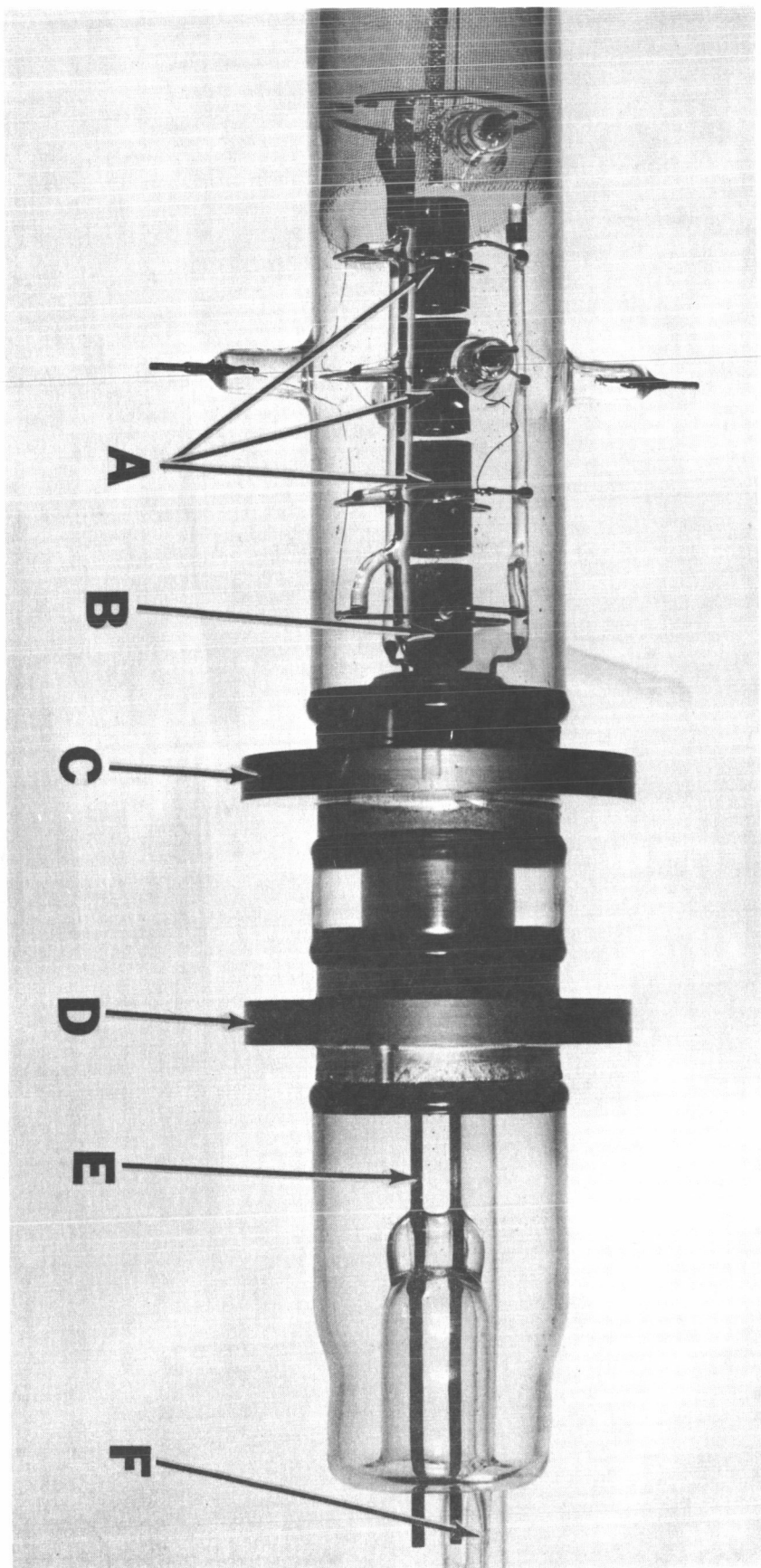
Figure 25. Duoplasmatron ion source with lens assembly:

(A) Einzel lens    (D) Intermediate electrode

(B) Extractor lens    (E) Filament leads

(C) Anode    (F) Gas inlet

(3) the field at the tip was then reduced to zero, and the
tip was sputtered for a period of 5 to 10 seconds with
a He ion beam of known energy and density, the latter
being determined by the amount of charge collected in
a Faraday cup arrangement;

(4) the viewing field was again applied to the tip, the imag-
ing gas readmitted, and the resulting field ion pattern
photographed.

One difficulty that arose with the tube design used here was that of
aligning the target tip with the ion gun and the Faraday cup; thus the number
of ions and ion density hitting the tip are known only approximately. However,
at any given ion energy the ion beam profile could be kept constant, so that
the number of ions hitting the tip was proportional to the charge collected by
the Faraday cup; thus sequential events could be followed. Also, due to the
small size of the tip, the ion beam density was uniform over its cross-section.


Results

He ion bombardment of W. - The sputtering of W by He ions has been exam-
ined for ion energies of 50 eV, 100 eV, 500 eV, 1 keV, and 4 keV as a function
of the number of ions hitting the tip. A sequence of field ion patterns illust rating
sputtering by 4 keV ions are given in Figures 26-28. Figure 26(a) is the initial
pattern before sputtering, and Figure 26(b) identifies the major planes. Figure
27(a) illustrates the amount of sputtering done by $0.4 \times 10^{14}$ ions/cm$^2$ of 4 keV
ions; Figure 27(b), by $0.8 \times 10^{14}$ ions/cm$^2$; Figure 28(a), by $1.2 \times 10^{14}$ ions/cm$^2$;
and Figure 28(b), by $1.6 \times 10^{14}$ ions/cm$^2$. For these pictures the radius of the
tip was estimated from a determination of the best image voltage to be approxi-
mately 450 Å; thus, approximately 450 ions have hit the visible portion of the
tip between successive patterns. A rough count of the displaced and missing atoms
in Figure 27(a) yields approximately 350 events; extrapolation of Rosenberg
and Wehner's data[56] for low energy bombardment would give approximately 24
sputtered atoms for the same number of 4 keV He ions. Thus most of the
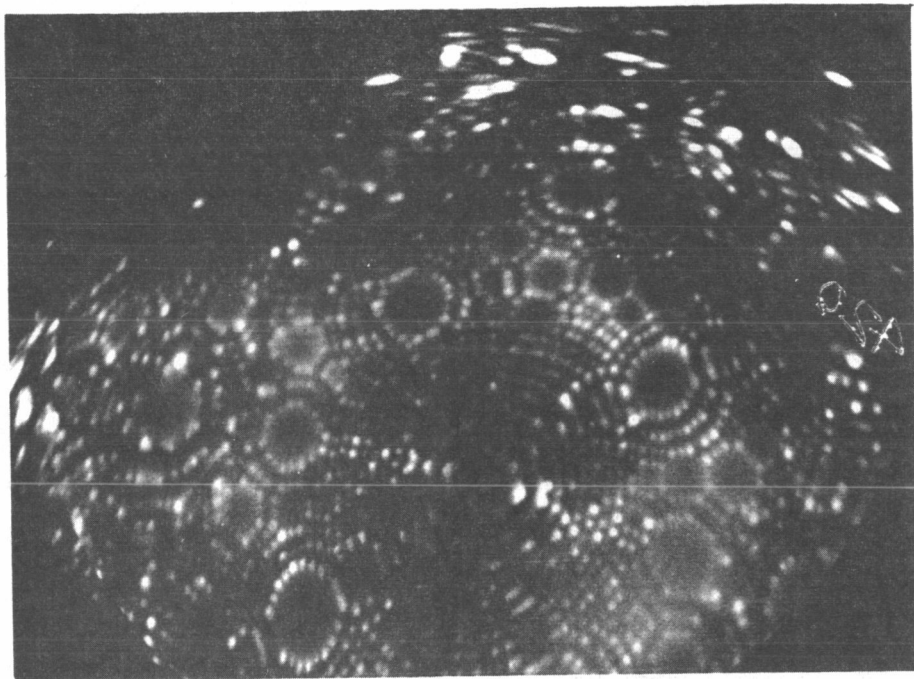
(a)
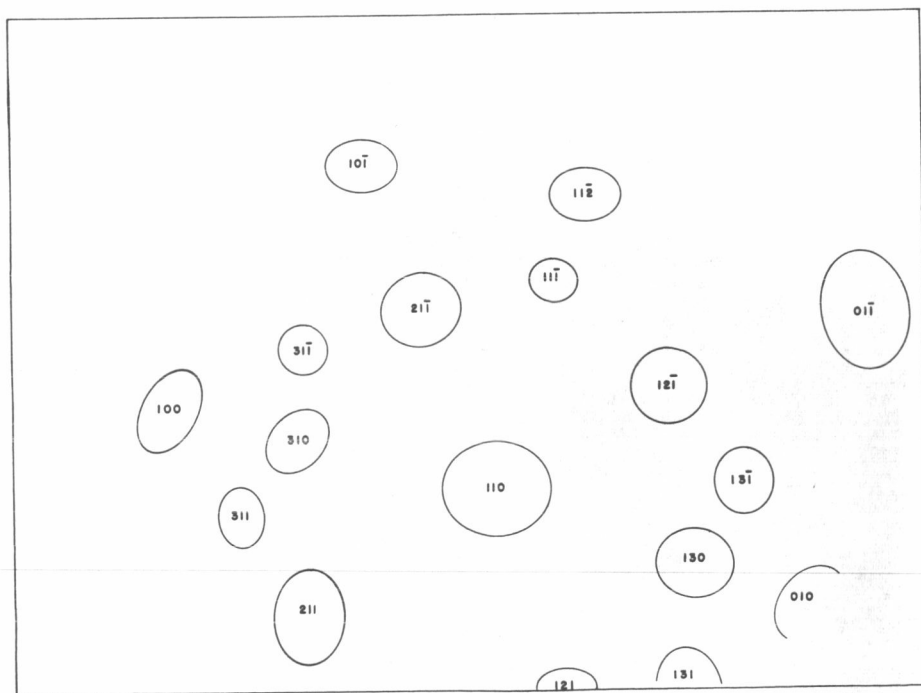


(b)

Figure 26.  (a) Initial field ion pattern of W surface before ion bombardment.
(b) Principle planes of a $[110]$ -oriented bcc crystal corresponding to (a).
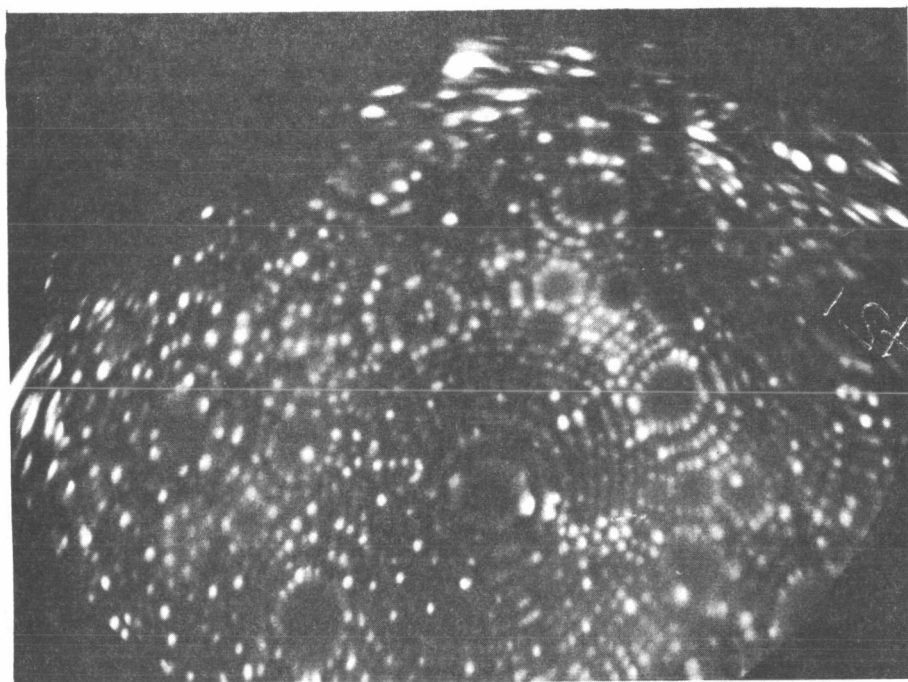
(a)
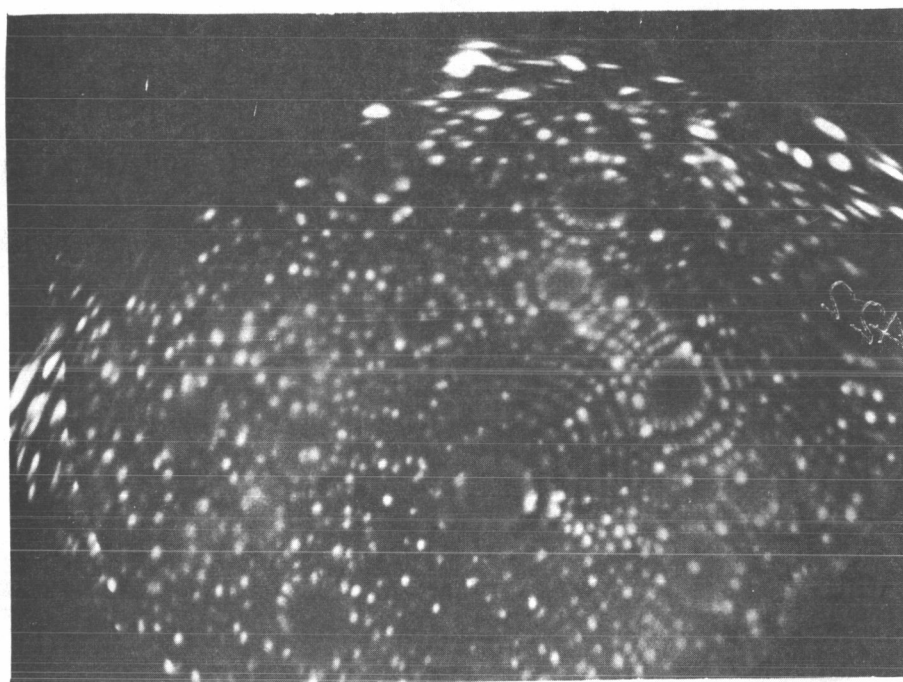


(b)

Figure 27.  The W surface of Figure 26 after bombardment by 4-keV He ions
(a) $0.4 \times 10^{14}$ ions/cm$^2$,  (b) $0.8 \times 10^{14}$ ions/cm$^2$.  The ion
beam is incident on the left.
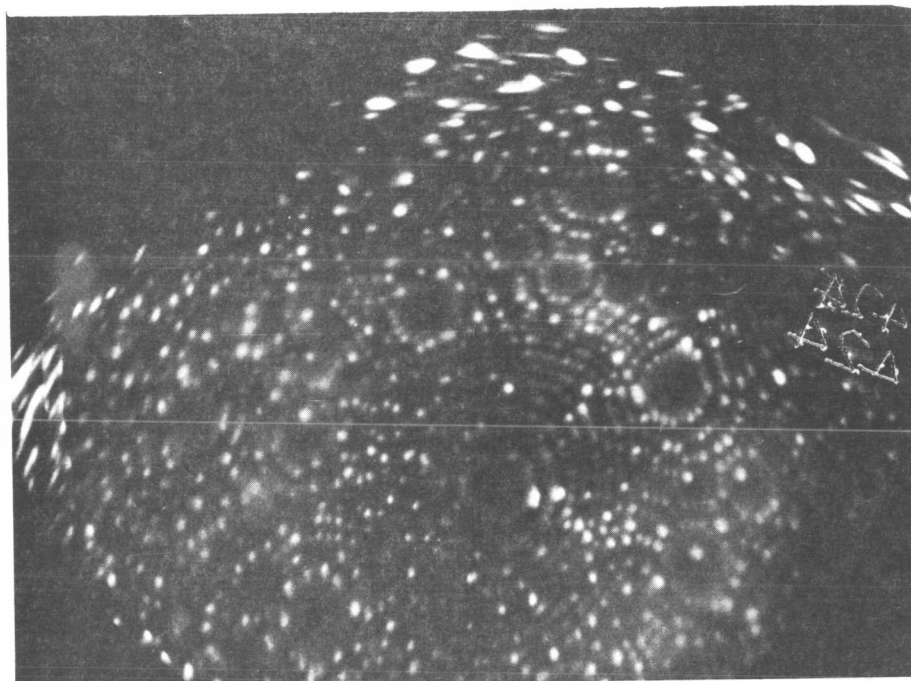
(a)
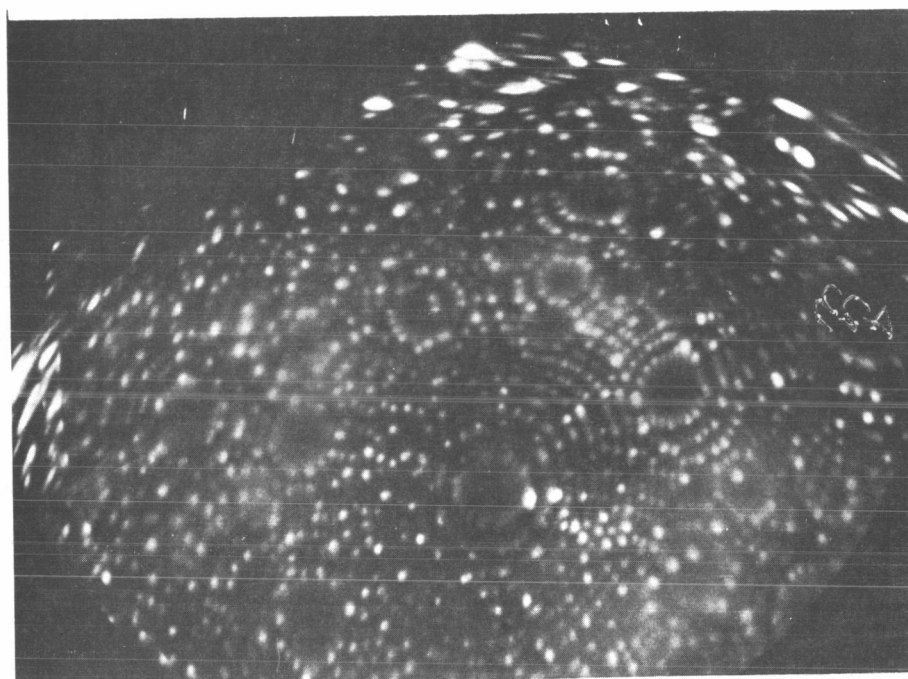


(b)

Figure 28.  The W surface of Figure 26 after bombardment by 4-keV He ions
(a) $1.2 \times 10^{14}$ ions/cm$^2$, (b) $1.6 \times 10^{14}$ ions/cm$^2$.  The ion beam
is incident on the left side.

events are rearrangement of atoms on the surface. In Figure 27(a) most of the damage can be seen to occur on the beam-incident side of the tip. Whole rows of atoms are missing from the uppermost (100) atom layer and from just to the left of the $(21\bar{1})$ plane. A few displacements and removals can be seen on the side of the tip away from the beam.

Further bombardment causes considerable additional change, as shown in Figure 27(b). Many of the displaced atoms in Figure 27(a) are missing in Figure 27(b), indicating that sputtering can be two- or multi-step process, as has been suggested by Harrison and Magnuson.[41] A sequence illustrating this clearly can be followed on the $(21\bar{1})$ plane. In Figure 27(a) three atoms, very likely displaced from the edge of the uppermost atom layer of the $(21\bar{1})$ plane, are sitting on top of it. After further bombardment in Figure 27(b) the three atoms are unchanged although changes have occurred on the edge of the supporting atom layer. In Figure 28 (a) only two atoms are left, one having been removed. In Figure 28(b) the remaining two have been removed. Similar sequences can be followed in many other portions of the pattern, thus clearly showing that sputtering can be a multi-step process, in contrast to a recent postulate.[57]

The 4 keV ions give enough energy to the tip to cause internal defects in structure. In Figure 29(a) material to a depth of one (211) layer has been removed from the tip, thus removing most but not all of the surface damage due to sputtering. Considerable disorder is left in the (100) regions and in high-index regions. The removal of one more (211) layer, as in Figure 29(b), removes most of this disorder; however, a dislocation line through the (100) plane can be seen, as well as some minor defects in other regions. The removal of four (110) layers are required to restore the tip to its initial condition.

The ion patterns of Figures 30(a), 30(b) and 31 were taken after sputtering the tip with an ion density of $0.4 \times 10^{14}$ ions/cm$^2$ at ion energies of 1 keV, 500 keV, 500 eV and 100 eV, respectively. From these patterns and the pattern in Figure 27(a) it can be seen that the number of displaced and
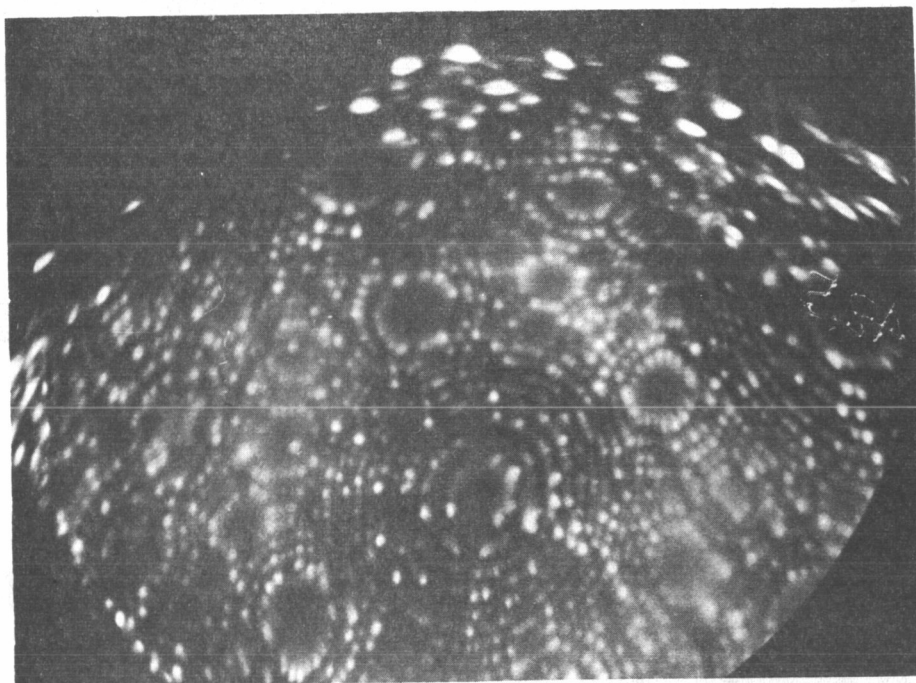
(a)
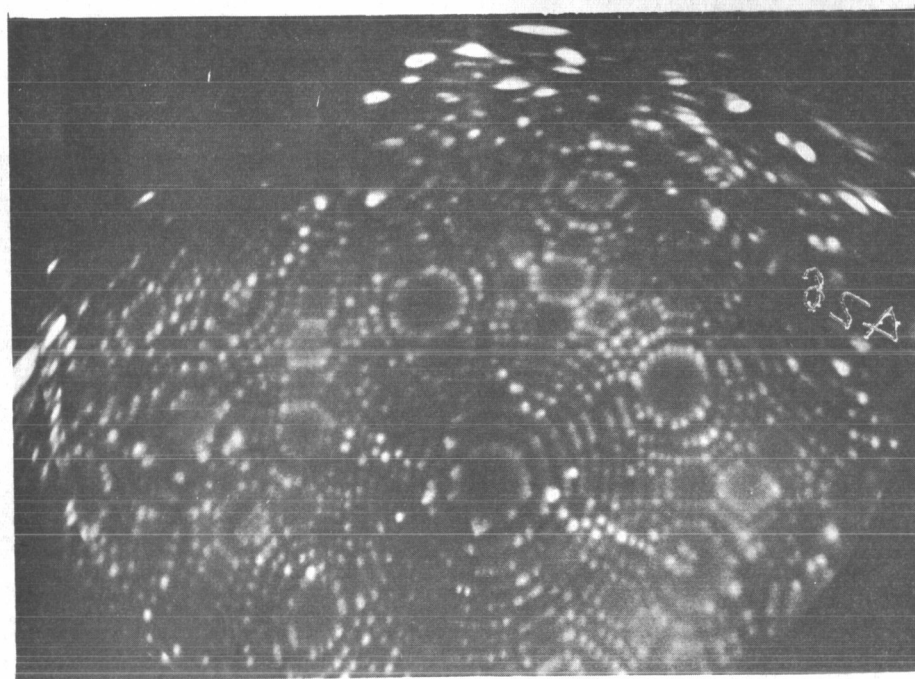


(b)

Figure 29.  The W surface of Figure 28(b) after the removal of (a) one (211) layer, and (b) two (211) layers.
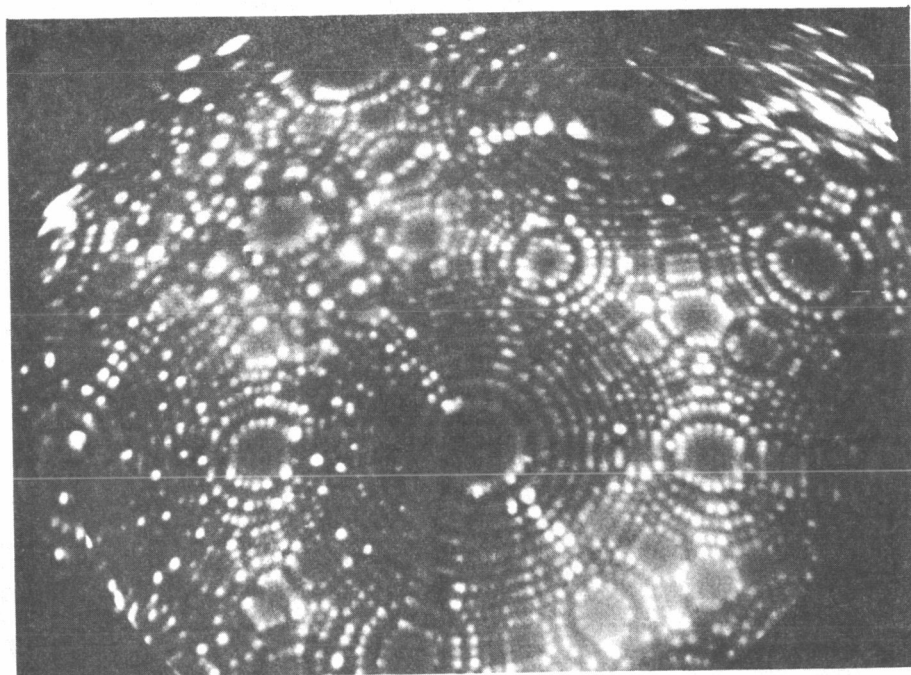
(a)
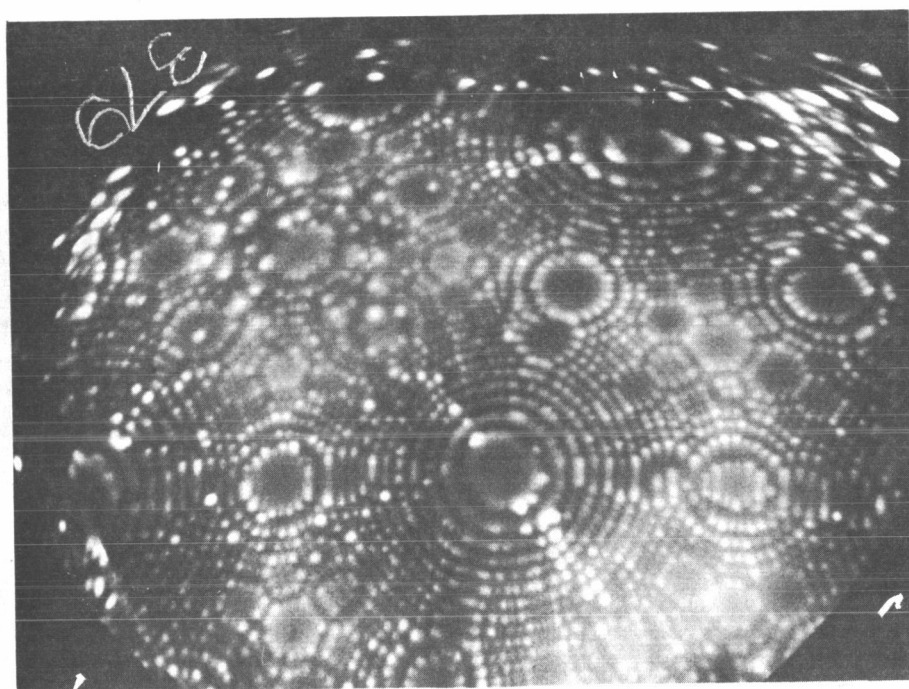


(b)

Figure 30. Field ion patterns of W after bombardment by $0.4 \times 10^{14}$ ions/cm$^2$ of He ions. Ion energy: (a) 1 keV, (b) 500 eV. The ion beam is incident on the left side.

Figure 31.  Field ion pattern of W after bombardment by $0.4 \times 10^{14}$ ions/cm$^2$ of 100-eV ions.  The ion beam is incident on the left side.

missing atoms decreases as the ion energy decreases. in the energy range investigated. Also, as would be expected, the depth of damage decreases with decreasing energy. Over the energy range investigated, most of the damage appears on the beam-incident side of the tip; in contrast, for 100 eV Xe ion bombardment of W most of the damage appeared on the far side of the tip in the form of missing atoms.[3,50]

The number of displaced and missing atoms in different regions of the sputtered patterns were determined by direct count, using Müller's two-color technique[58] to distinguish between the moved and the undisturbed atoms. Atom counts were performed on the sputtered patterns at all He ion energies except 4 keV, for which the surface damage was so extensive, involving several hundred events per pattern, that an accurate count was difficult if not impossible. Even at lower energies some events may not have been counted, especially missing atoms which are sometimes difficult to locate. However, the number of such missed events is probably small compared to the total number counted, and thus would not significantly affect the results. Tables IX to XII summarize some of the important features of the atom count data.

In Table IX are given the results of atom counts from a sequence of ion patterns for bombardment by 1 keV ions. The first column gives the approximate number of ions that have hit the target between successive patterns; the second column (added atoms) gives the number of atoms that have moved more than one lattice site; the third column (displaced atoms) is the number of atoms that have moved only one lattice site; the fourth column is the number of missing atoms; the fifth column is the difference between the second and fourth columns and is the net interchange of atoms between the visible portion of the target and the rest of the target and its environment; the sixth column (number of sputtering events) is the total of columns two, three and four. These data exhibit several features of the sputtering process. First, the ratio of sputtering events to bombardment ions decreased with increasing number of ions. This was also observed at other ion energies. Second, the number of atoms lost to the environment is a small fraction of the total number of sputtering events

at all the ion energies investigated. However, for 1 keV ion bombardment the number lost (32) is in good agreement with the yield extrapolated from Rosenberg and Wehner's data for these conditions.[56] Finally, there are large fluctuations in any one column, related to the statistical nature of the ion impact.

TABLE IX

Number of Sputtering Events on W as a Function of
Number of Bombarding 1 keV He Ions

| Approximate Number of Ions | Added Atoms | Displaced Atoms | Missing Atoms | Net Difference | Number of Sputtering Events |
|---|---|---|---|---|---|
| 450 | 43 | 29 | 42 | -1 | 114 |
| +450 | 35 | 27 | 54 | 19 | 116 |
| +450 | 32 | 11 | 30 | -2 | 73 |
| +450 | 19 | 9 | 19 | 0 | 47 |
| +450 | 13 | 6 | 29 | 16 | 48 |
| Total | | | | | |
| 2250 | 142 | 82 | 174 | 32 | 398 |

In Table X the number of sputtering events in a region of the target lying between the two angles of incidence listed are given as a function of the angle of incidence for different ion energies. The number of sputtering events does not seem to be a strong function of the angle of incidence for the side of the target exposed to the ion beam; a slight shift in the maximum number toward lower angles incidence as the bombarding ion energy is increased can be noted. However, there is a surprising number of sputtering events occurring on the side of the target where no ions can hit directly. The percentage of events occurring on the back side of the target was 8% for 50 eV ion bombardment, 12% for 100 eV ions, 14% for 500 eV ions, and 18% for 1 keV ions. These events are not just atoms that have migrated from the beam-incident

88

side; of the 33 events beyond 110 degrees for 1 keV ion bombardment, 22
are missing or displaced atoms.

TABLE X

Number of Sputtering Events on W as a Function of Angle of
Incidence for He Ion Bombardment

| Angles | 50 eV | 100 eV | 500 eV | 1 keV |
|---|---|---|---|---|
| 30-50 | 53 | 54 | 77 | 121 |
| 50-70 | 64 | 63 | 92 | 99 |
| 70-90 | 65 | 65 | 84 | 96 |
| 90-110* | 12 | 19 | 29 | 37 |
| 110-130* | 2 | 5 | 8 | 22 |
| 130-150* | 3 | 2 | 5 | 11 |

* These regions are on the side of the target opposite the ion beam.

Table XI lists a normalized sputtering event density as a function of the
crystallographic region of the target for the various bombardment ion energies
for which atom counts were taken. Since the portion of the target visible in
the ion pattern is essentially hemispherical, all of the crystallographic direc-
tions associated with the bulk crystal structure are exposed, and comparisons
can be made among the various crystallographic regions. The normalized
sputtering event density is obtained by dividing the number of events on a
particular type of crystallogrpahic region by the total area of that type of
region over the visible portion of the target and by the total number of events
at the particular ion energy. For the major planes ( {110}'s, {100}'s, {211}'s,
{111}'s) the area includes only the uppermost atom layer on each plane in a
given family of planes. The other regions were chosen as those lying between
two major planes (for example, the {310-210} regions lie between the {100}
and the {110} planes, etc.). The uncertainty in the sputtering event density
is obtained from the square root of the number of events on each type of region.
From the data of Table XI the crystallographic regions are ranked in Table XII

89

in order of decreasing sputtering event density.

TABLE XI

Normalized Sputtering Event Density as a Function of W Crystallographic
Region for He Ion Bombardment

| Family of Regions or Planes | 50 eV | 100 eV | 500 eV | 1000 eV |
|---|---|---|---|---|
| {110} | 0(0) | 0(0) | $2 \pm 1(2)$ | $6 \pm 2(8)$ |
| {100} | $13 \pm 9(2)$ | $10 \pm 4(5)$ | $17 \pm 6(8)$ | $13 \pm 4(9)$ |
| {211} | $13 \pm 3(17)$ | $10 \pm 3(13)$ | $9 \pm 2(19)$ | $10 \pm 2(23)$ |
| {111} | $20 \pm 10(4)$ | $24 \pm 10(6)$ | $19 \pm 6(9)$ | $9 \pm 5(4)$ |
| {310-210} | $13 \pm 2(55)$ | $8 \pm 1(42)$ | $10 \pm 1(77)$ | $14 \pm 1(102)$ |
| {311} | $14 \pm 2(49)$ | $16 \pm 2(54)$ | $17 \pm 2(74)$ | $15 \pm 2(82)$ |
| {221} | $9 \pm 3(12)$ | $10 \pm 3(16)$ | $8 \pm 2(18)$ | $10 \pm 2(18)$ |
| {431-321} | $7 \pm 1(47)$ | $8 \pm 1(54)$ | $7 \pm 1(68)$ | $11 \pm 1(127)$ |
| {433-322} | $11 \pm 3(15)$ | $14 \pm 3(21)$ | $11 \pm 2(26)$ | $11 \pm 2(25)$ |
| Total Number of Events | 201 | 211 | 301 | 398 |

The numbers in parentheses are the total number of events occurring on
that family of planes or regions.

90

# TABLE XII

### Ranking of Crystallographic Planes and Regions
### in Order of Decreasing Sputtering Event Density

| 50 eV | 100 eV | 500 eV | 1 keV |
|---|---|---|---|
| {111} | {111} | {111} | {311} |
| {311} | {311} | {311} | {310-210} |
| {100} | {433-322} | {100} | {100} |
| {211} | {100} | {433-322} | {433-322} |
| {310-210} | {211} | {310-210} | {431-321} |
| {433-322} | {211} | {211} | {211} |
| {221} | {310-210} | {221} | {221} |
| {431-321} | {431-321} | {431-321} | {111} |
| {110} | {110} | {110} | {110} |

Although the uncertainties are large, some tentative conclusions can be drawn from the data of Tables XI and XII. At low ion energies the sputtering event density is highest on the {111} planes. At 1 keV ion energy the ranking of the {111} planes drops from first to next to last, not due particularly to a change in the number of events occurring on the {111} planes, but because more events are occurring on other planes. The {311} regions, which lie between the {211} and the {100} planes have the next highest sputtering event density at low ion energies and the highest sputtering event density at 1 keV ion energies. It can be seen from Table XII that the {100} planes and their surrounding regions (the {311} and the {310-210} regions) become relatively more important as the bombardment ion energy increases. The sputtering event density is least on the {110} planes throughout the ion energy range investigated. However, as the bombarding ion energy is increased, the differences between the various crystallographic regions become less; this has been observed previously in ejected sputtered atom patterns.

Platinum. - An attempt was made to use a platinum needle as the sputtering target, in order to investigate the sputtering of a metal with a fcc crystal structure. We were not successful in obtaining a good ion pattern of the Pt target, which was held at a temperature of $77^{\circ}$K. At this temperature the best image voltage for He imaging was above the Pt desorption voltage; thus a stable image was not obtained. The Pt surface was imaged with $H_2$ gas, but the many-faceted endform typical of He imaging at liquid hydrogen temperature [48] was not obtained. Liquid hydrogen cooling was not tried because it was not available to us at the time of this work.

He ion bombardment of Ir. - Since iridium is a fcc metal that is more refractory than platinum, and at $77^{\circ}$K has a He best image voltage below its field desorption voltage, it was used as a target for He ion bombardment. We had difficulty in obtaining Ir needles sharp enough for field ion microscopy. The dc drop-off method of etching tips, described elsewhere, was used; the zone-melted Ir metal was so soft that usually the needle blank dropped off too soon, leaving a tip too dull for ion microscopy, or bent, producing work-damage in the tip, such as is seen in the field ion pattern of Figure 32 (a).

The Ir target shown in Figure 32 (a) was bombarded by 100 eV He ions and a sequence of four ion patterns taken, the last of which is Figure 32 (b). A total of 75 sputtering events were counted in the four ion patterns; the Ir target had been bombarded by one-half the number of He ions that caused 211 sputtering events on the W target. According to Rosenberg and Wehner[56] the sputtering yield of Ir and W bombarded by 100 eV He ions are approximately the same; these results are in rough agreement. Because of the multiple crystal boundaries and other defects in the Ir target, no attempt was made to correlate the number of sputtering events with crystallographic regions or angle of incidence. Of the 75 sputtering events counted, 15 (20%) were on the side of the target away from the ion beam. Considering the number of defects in the target, it is surprising that so much energy is channeled through.

An Ir target that was free of crystal boundaries and most other defects was produced (Figure 33) and used as a target for 500 eV He ion bombardment.
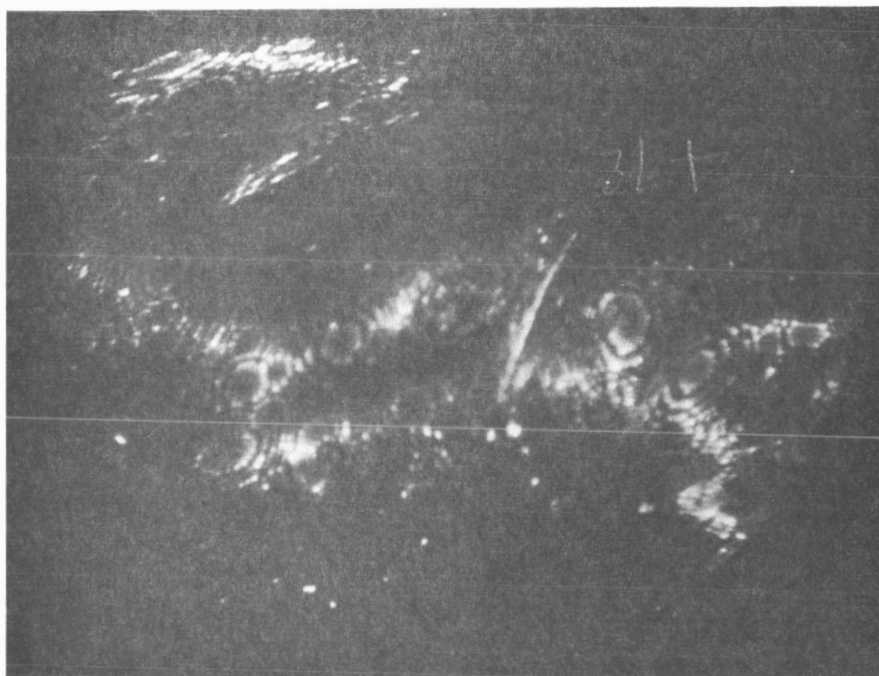
(a)
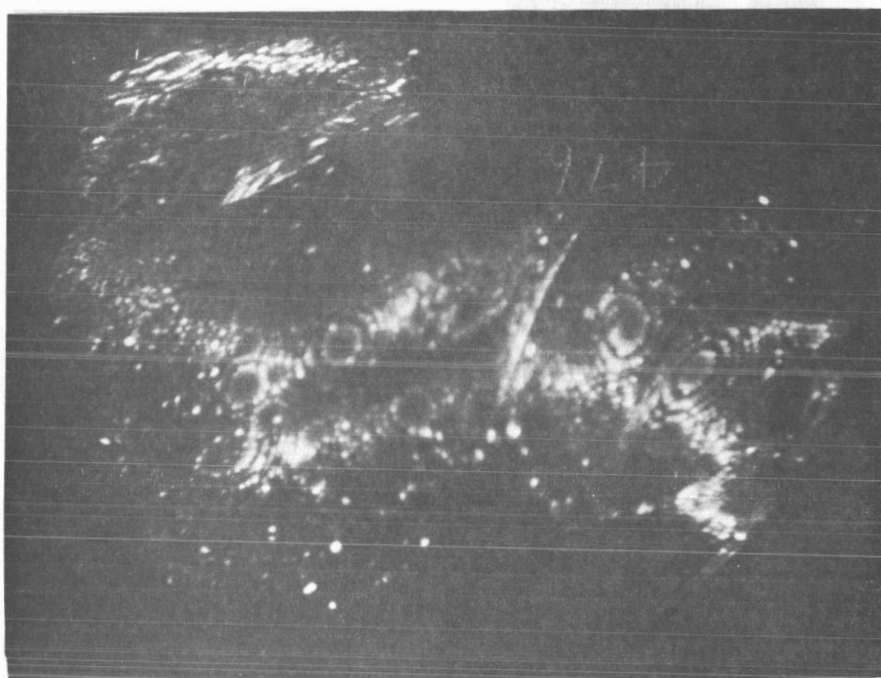


(b)

Figure 32. (a) Field ion pattern of a clean Ir surface containing several crystal boundaries and other defects.

(b) The Ir surface of (a) after bombardment by approximately $2 \times 10^{13}$ ions/$cm^2$ 100-eV He ions. The ion beam is incident on the left side.

93
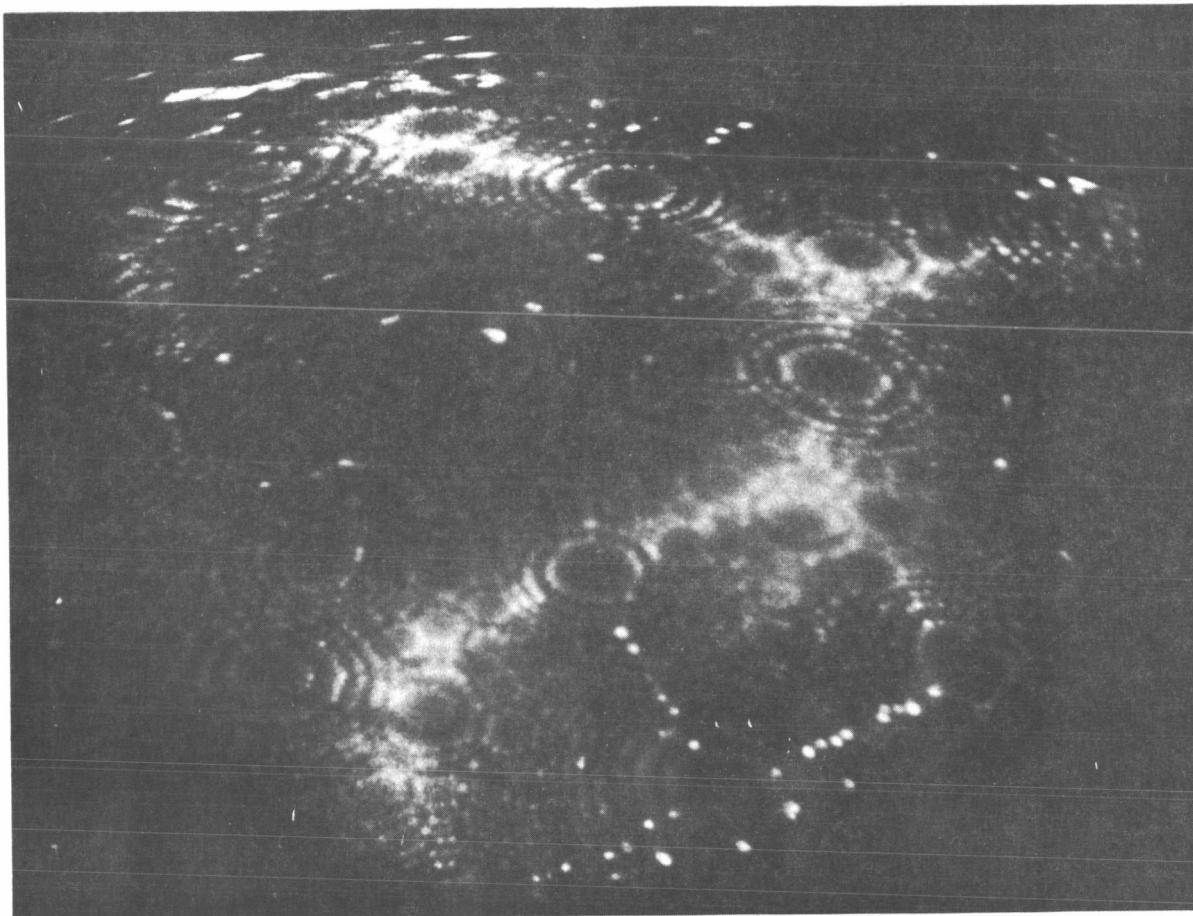
Figure 33. Field ion pattern of clean and nearly defect-free Ir surface.

Unfortunately the best image voltage for this sequence was misjudged, allowing some field desorption of the surface during the photographing of the ion patterns and thus changing the sputtering results. No further results were obtained in this area.

## FEM STUDIES OF CS ION BOMBARDMENT OF W

A preliminary study of Cs ion bombardment of W has been reported;[3] in that study the ion density striking the target and direction were not known. In the present study the ion beam is monoenergetic, unidirectional and of measured density.

### Experimental Tube and Techniques

FEM sputtering tube design. - The tube used in this investigation is shown in Figure 34; it contained an ion gun to form a unidirectional ion beam, a FEM arrangement to determine the changes in the target due to sputtering, and an ion collector assembly to measure the ion beam current density. The cesium ion source consisted of cesium aluminosilicate , described in an earlier section, coated onto a resistively heated Pt-13% Rh filament. The ion gun potentials were so chosen that to the emitter and ion collector assembly the ion beam appeared to be coming from a point source situated at the ion source. The target, in the form of a field emitter, was mounted on a filament connected to a four-wire press, so that the target temperature could be controlled and monitored.

Procedure. - In order to establish first the effect of cesium ion bombardment on the surface of clean tungsten, the following procedure was followed:
(1) The emitter was first cleaned and smoothed by flashing it to approximately $2400^{\circ}K$ (the resulting field emission pattern is shown in Figure 35 (a), and the current-voltage characteristic of the clean target determined. (2) The emitter was then bombarded by cesium ions of known energy and amount (resulting in a pattern of which (Figure 35 (b) is typical). (3) Cesium adsorbed on the emitter during bombardment was removed by field desorption at $77^{\circ}K$, resulting in a clean but roughened tungsten surface (Figure 35 (c),

95
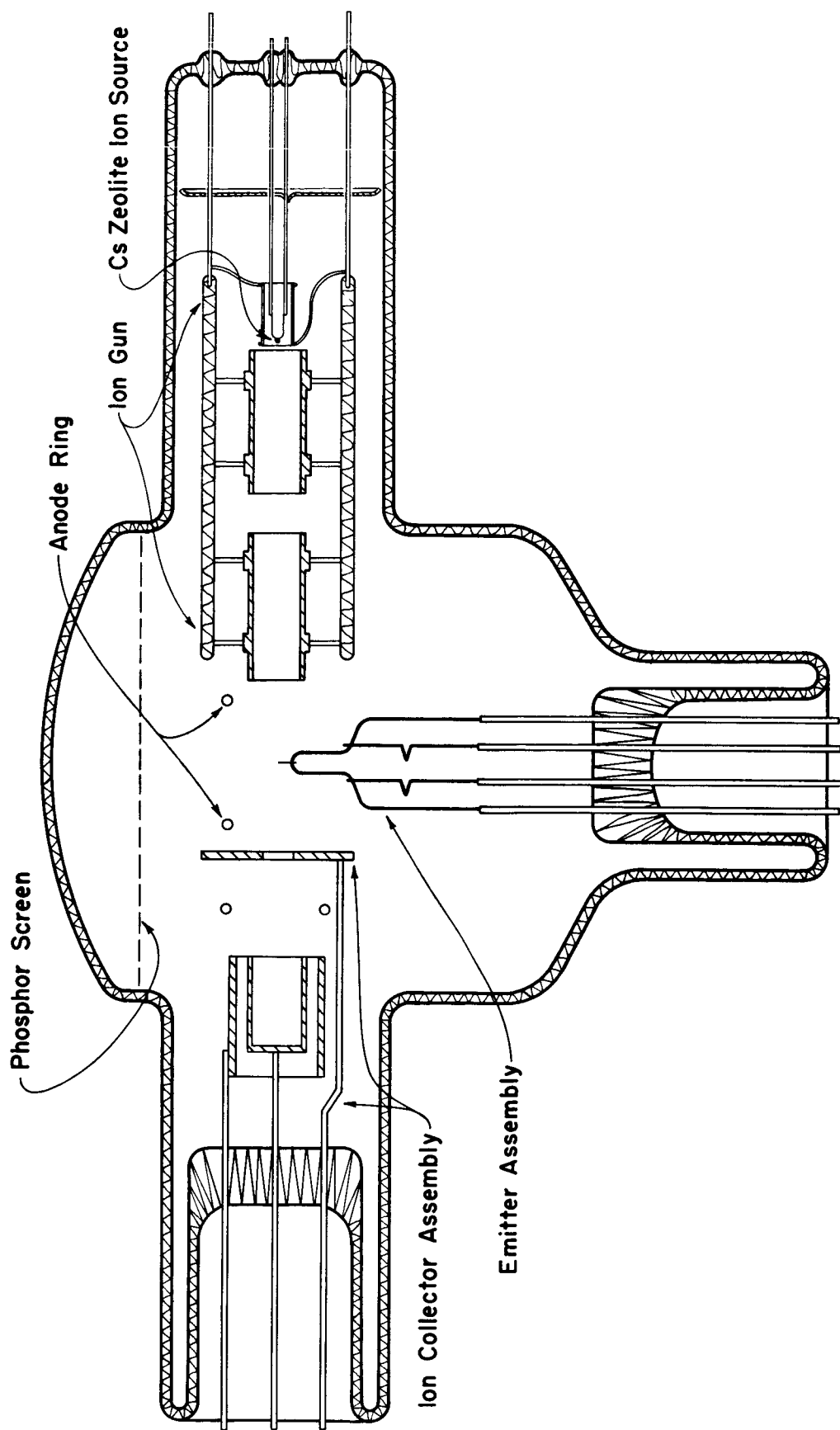
Figure 34.  Diagram of FEM sputtering tube used for the study of Cs ion bombardment of W.

96
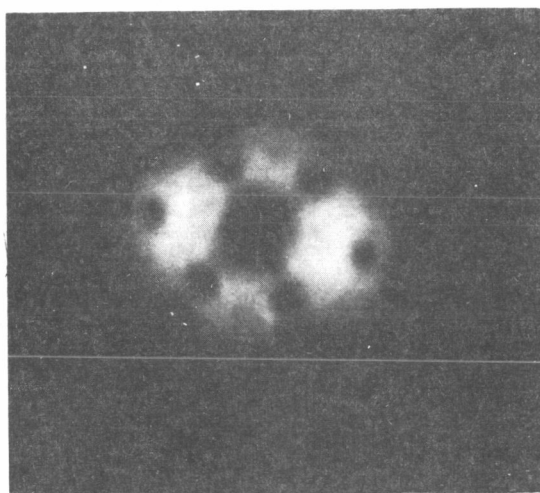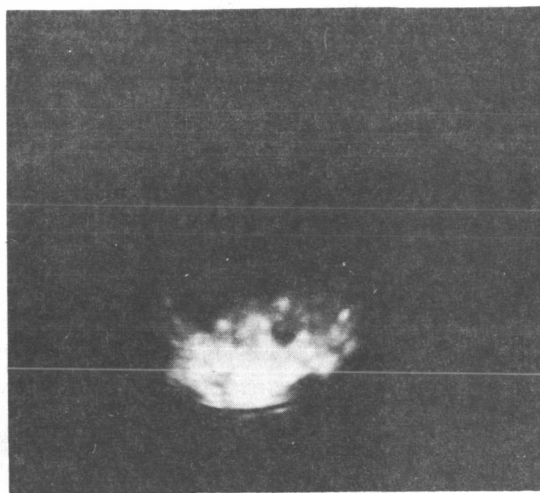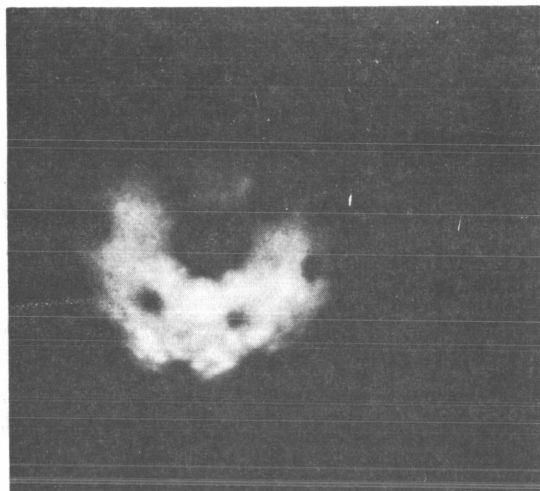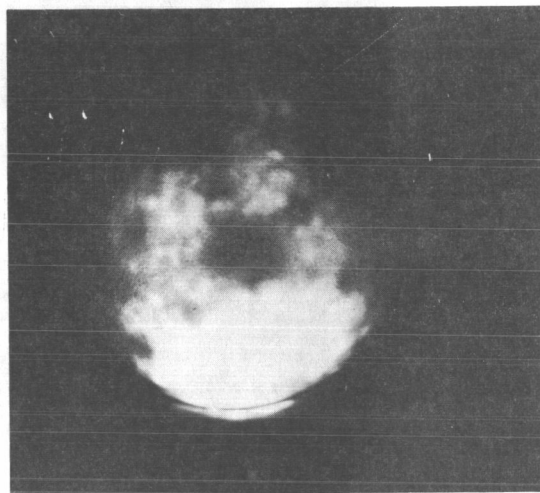
(a)   (b)   (c)   (d)

Figure 35.  Field emission pattern changes associated with the sputtering of
clean W by $7.3 \times 10^{14}$ ions/cm$^2$ of 500-eV Cs ions incident upon
the lower side of the emitter:  (a) clean W;  (b) after ion bombard-
ment of the emitter;  (c) after field desorption of Cs from the
emitter;  (d) same surface as in (b) at a higher viewing voltage to
show backscattered Cs in the upper portion of the pattern.

97

of which the current voltage characteristic was then determined. (4) After removing the resulting damage by annealing the emitter at $1900^\circ$K for 1 minute, the above steps were repeated at a different ion energy or ion density.

Field emission current is an exponential function of the emitter shape and thus a sensitive detector of projections on the emitter that are a few angstroms in height. The change in the emitter surface geometry due to ion bombardment may be monitored by either the increase in the ratio of emission current $I_s$ due to ion bombardment over the current $I_o$ for smooth emitter surface at a fixed applied voltage, or by a change in the geometrical factor $\beta$ as determined from the change in slope of a Fowler-Nordheim plot (Equation (9)). Since the changes in surface shape monitored here were small, the first method, which is the more sensitive, was used.

<u>Surface roughening as a function of ion energy and density.</u> -The pattern changes shown in Figure 35 correspond to bombardment of clean tungsten by $7.3 \times 10^{14}$ ions/cm$^2$ density of 500 eV cesium ions. As expected, most of the pattern change was on the beam-incident side of the emitter (Figure 35 (b)), and was due primarily to cesium deposited by the ion beam. However, when the viewing voltage was increased, some cesium would be seen on the side of the emitter away from the beam (Figure 35 (d)); this was probably due to cesium backscattered by the ion beam from nearby electrodes, principally the plate of the ion collector assembly. All of the cesium was removed from the surface by applying a field of approximately 60 Mv/cm. Figure 35 (c) shows that the damage resulting from bombardment by 500 eV ions was confined to the beam-incident side of the emitter. The damage seems more pronounced on the low index planes, a result in agreement with that obtained for 500 eV xenon ion bombardment of tungsten in the field ion microscope.[3, 50]

The ratio of emission currents before and after sputtering, $I_s/I_o$, is plotted in Figure 36 as a function of Cs ion density for ion energies between 100 eV and 3.8 keV. From the graph it can be seen that in general the amount of roughening increases with increasing ion density and with increasing ion energy. However, the amount of roughening increases less rapidly with the
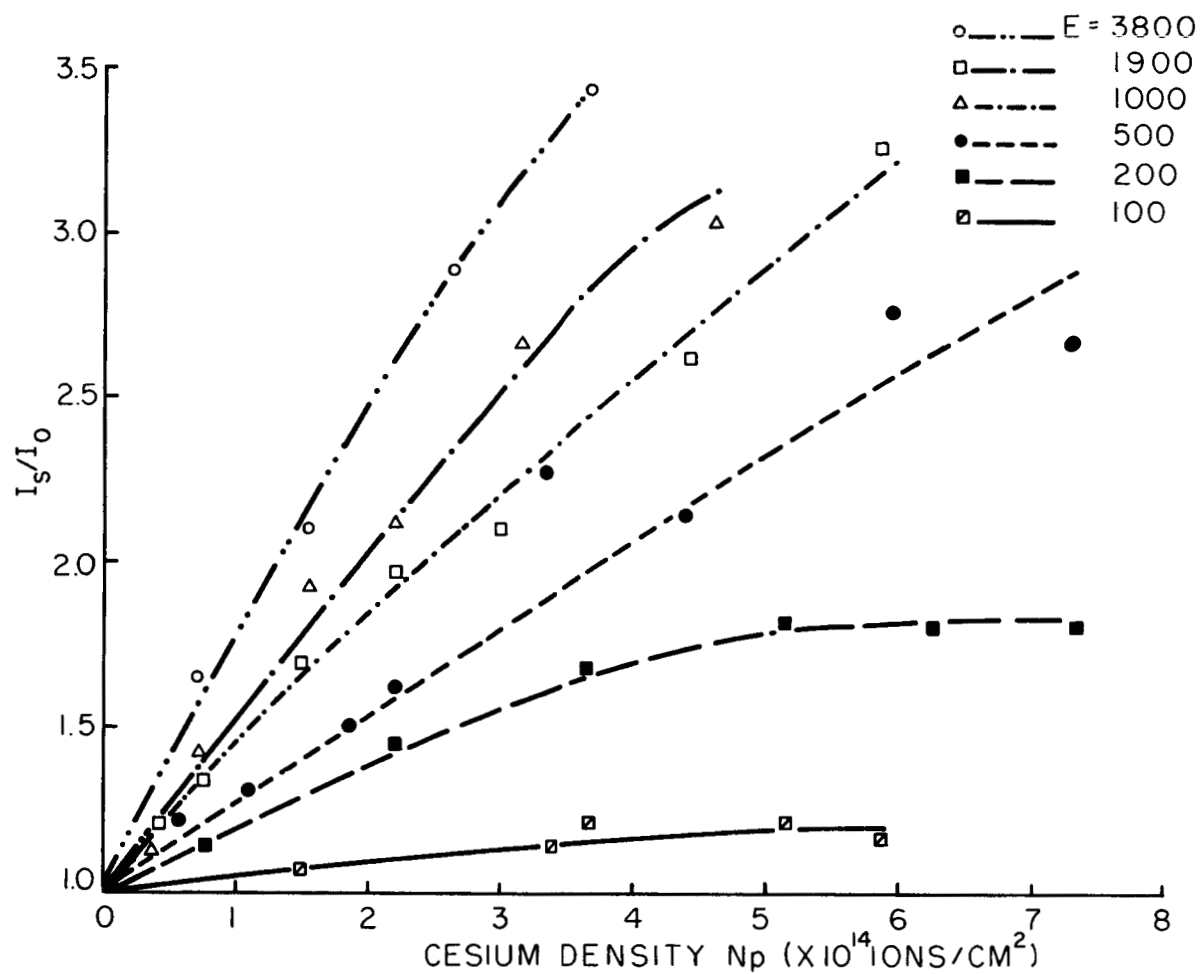
Figure 36. Ratio of W emission current after Cs ion bombardment to emission current before bombardment at a fixed tube voltage, $I_s/I_o$, as a function of Cs ion density for several ion energies.

higher ion densities than with the lower ion densities, probably due to the sputtering away of new projections as they are formed. It is interesting to note that, as ion energy is increased, this effect occurs at higher amounts of roughening but at lower ion densities.

In Figure 37 the current ratio $I_s/I_o$ is plotted as a function of Cs ion energy at constant ion density. Extrapolation of the resulting curve to a current ratio of 1 yields a threshhold energy of approximately 30 eV, about the same as the sputtering threshhold value of 30 eV measured by Stuart and Wehner for Xe ion bombardment of W.[59]

Temperature effects. - To investigate the annealing of surface damage, the emitter was bombarded by 3800 eV ions with the emitter at $77^{\circ}$K. It was then heated for 60 second intervals to successively higher temperatures and the resulting changes in the current ratio $I_s/I_o$ noted. The results are plotted in Figure 38. Surprisingly, some of the damage is removed at a temperature of $100^{\circ}$K, and all of the damage is removed at a temperature below $800^{\circ}$K. Since interstitial atoms in the bulk can anneal out to the surface at approximately $85-95^{\circ}$K,[49] the surface damage is related to the bulk damage, thus suggesting that the bulk damage is annealed at $800^{\circ}$K.

The temperature dependence of the surface roughening due to ion bombardment was investigated by measuring the change in $I_s/I_o$ as a function of the temperature to which the target had been heated during bombardment. The resulting data for ion energies 3014 eV and 534 eV are plotted in Figure 39. The surface roughness decreases with increasing temperature. However, as shown in Figure 39, the results are essentially the same when the target is bombarded at $77^{\circ}$K and then annealed at the elevated temperature for a time equal to the bombardment time. This implies that the decrease in surface roughness at higher temperatures is just due to the annealing that is taking place during bombardment. Thus sputtering at higher temperatures is from a more ordered surface than at lower temperatures.
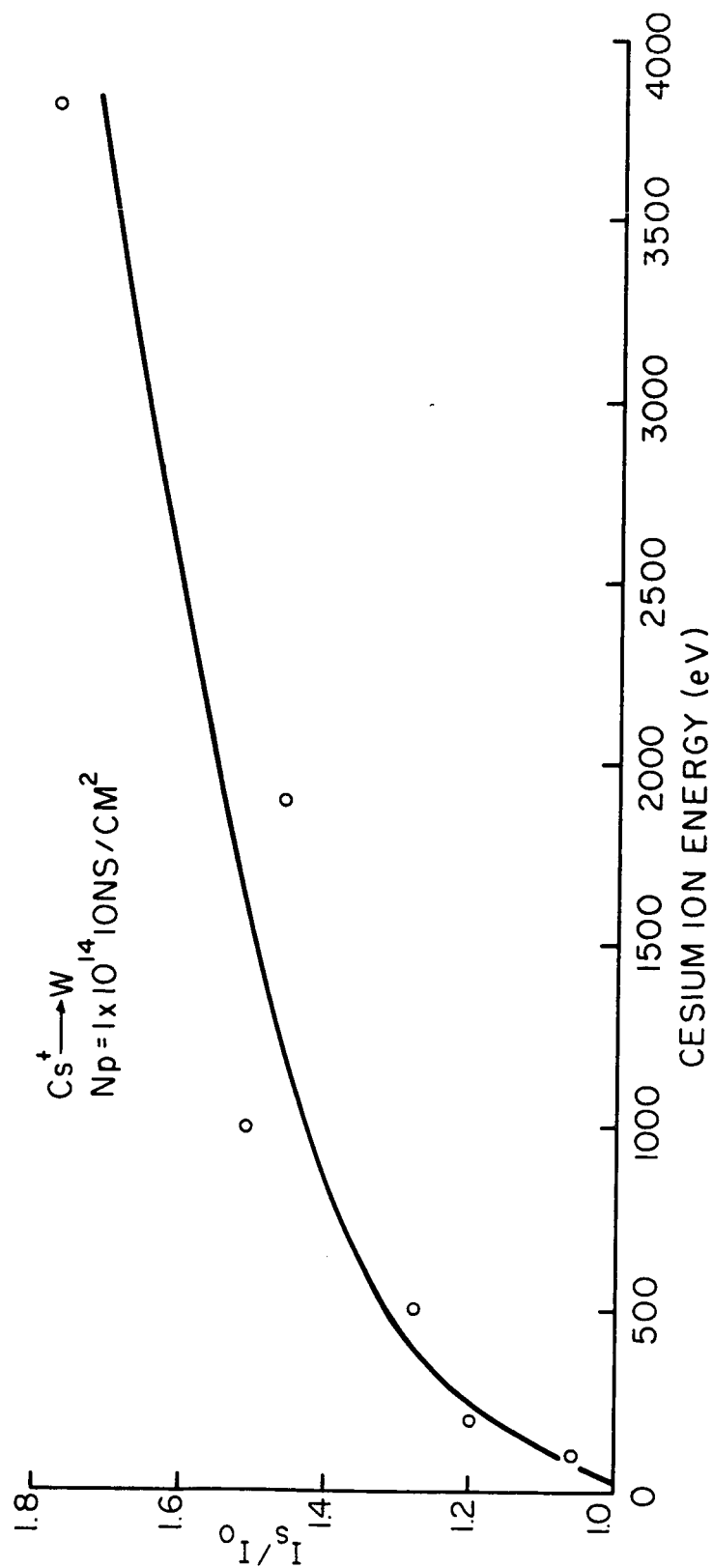
Figure 37.  The current ratio $I_s/I_o$ as a  function of Cs ion energy for an ion.
density of $1 \times 10^{14}$ ions/$cm^2$ for Cs ion bombardment of W.

101
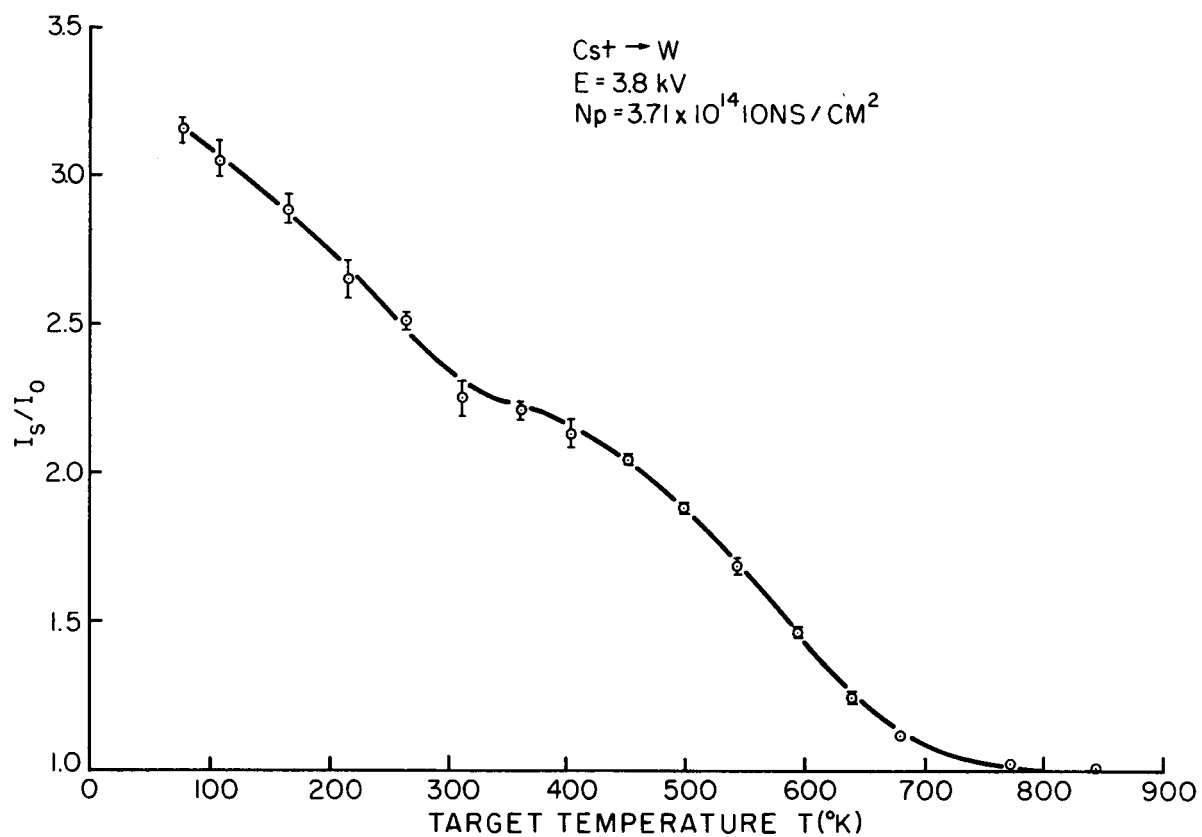
Figure 38. The current ratio $I_s/I_o$ as a function of the temperature to which the W emitter had been heated for successive 60 second heating periods, after the emitter had been bombarded by $3.71 \times 10^{14}$ ions/ $cm^2$ of 3800-eV Cs ions.
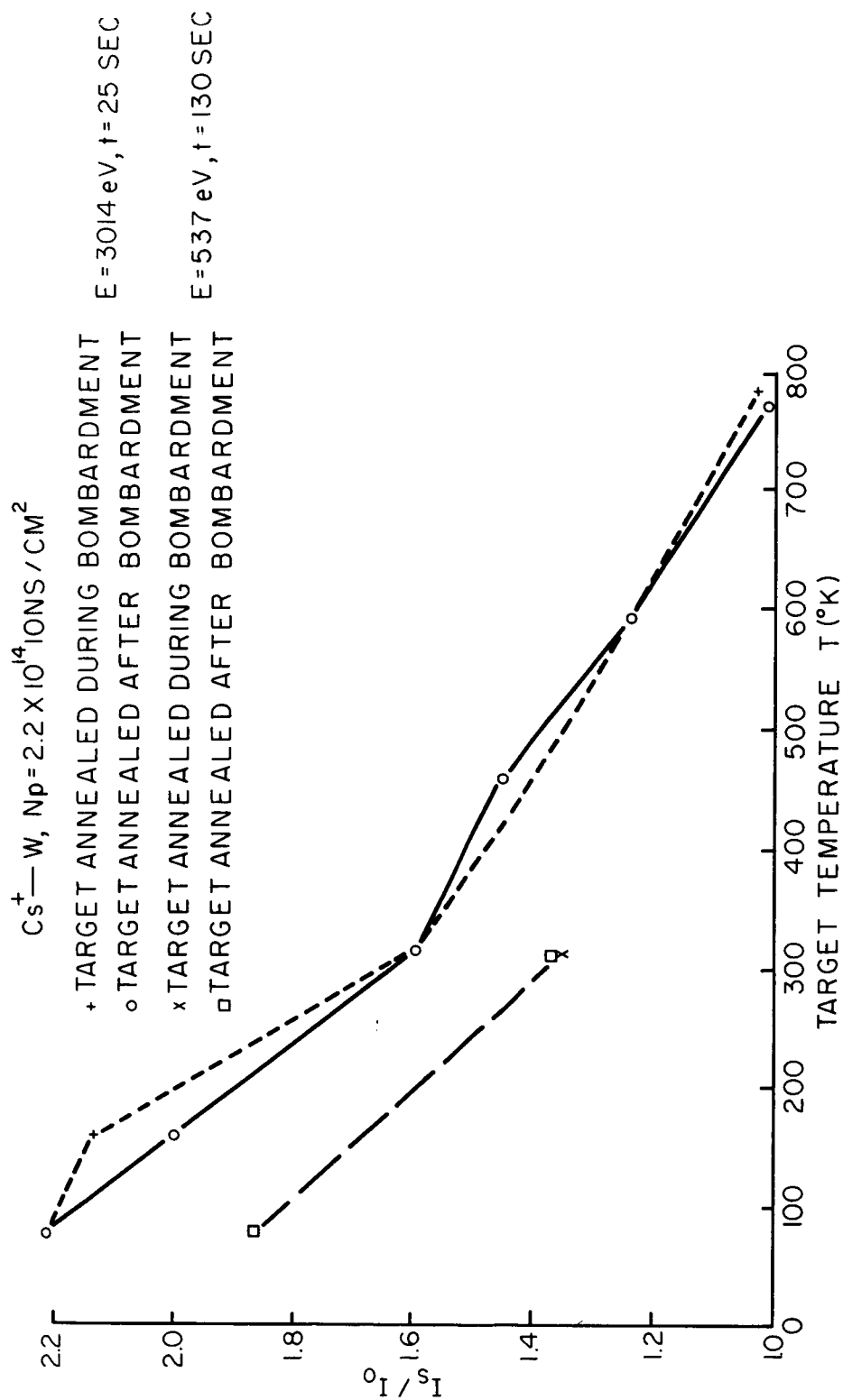
Figure 39. The current ratio $I_s/I_o$ as a function of W target temperatures for annealing either during or after Cs ion bombardment.

103

# DISCUSSION AND CONCLUSIONS

## Comparison of Helium and Xenon Ion Sputtering Results

The field ion patterns for both He and Xe ion bombardment show rearrange-
ment of surface atoms as well as true sputtering in the sense of a net atom
removal from the surface. For 500 eV and 1 keV He ions the number of
surface events are much larger than the number of atoms lost; for the same
energy Xe ions the reverse is true. At any given energy the total number of
sputtering events is much greater for Xe than for He, in agreement with the
results of other investigators.[56, 39] The ratio of sputtering events on the back
side of the target to those on the beam-incident side, which in general is
greater for Xe than for He ion bombardment, is greater than one for the 100 eV
energy; for He the ratio is always a small fraction. The depth of damage is
not as great for He as for Xe ion bombardment at a given energy. One reason
for these differences can be attributed to the difference in the fraction of ion
energy that can be transferred to an individual W atom. This fraction is given
by[39]

$$f = 4 M_i M_a / (M_i + M_a)^2, \qquad (30)$$

where $M_i$ is the mass of the bombarding ion and $M_a$ the mass of the target
atom, and is 0.97 for $Xe^+$ W and 0.083 for $He^+$ W. Thus the He ions are
much less efficient at transferring their energy to the W lattice than are the
Xe ions.

## Energy Transfer Along Silsbee Chains

Atom ejection patterns from single crystal sputtering show character-
istic spots corresponding to ejection along certain low-indexed crystallo-
graphic directions, an effect first observed by Wehner.[60] This effect has
been assumed by most authors to be direct experimental evidence that
momentum is focused into the close-packed directions of a crystal, as

first postulated by Silsbee.[61] Recently, however, a number of authors[45,62,63] have raised the question of the importance of the energy chain concept in the sputtering process. Harrison, et al.,[45] in a computer simulation study of Ar ion bombardment of Cu, obtained characteristic atom ejection patterns by following the detailed trajectories of individual sputtered atoms, and showed that the patterns were due to surface billiard collisions, and that the first four atomic layers contained all the events that led to sputtering, even for 10 keV bombardment energies. Directed sputtering is explained by Lehmann and Sigmund[62] on the basis of a collision cascade theory, in which the sputtered atoms are focused by neighboring atoms in the surface.

Although the above considerations may cast doubt upon the importance of Silsbee chains in the normal backward sputtering (i.e., sputtering on the beam-incident side of the target), it is still believed to play a role in other radiation damage processes.[43,44] Our results indicate that Silsbee chains are an important energy transfer mechanism for forward sputtering of thin targets or films. As suggested by the computer studies by Gibson, et al.,[43] the forward sputtering for both He and Xe ion bombardment is found to be a function of both ion energy and of the length of the collision chain within the crystal. The increase in the forward to backward sputtering ratio with increasing He ion energy suggests that the maximum ratio has not been reached at 1 keV ion energy; from consideration of the energy transfer ratio (Equation (30)) and the fact that the maximum sputtering ratio for Xe ion bombardment occurs around 100 eV, one would expect the maximum forward to backward sputtering ratio for He ions to occur in the low keV ion energy range.

## Temperature Dependence of Sputtering

The effect of temperature on sputtering has been confused by contradictory results due to polycrystalline targets and contaminated surfaces.[39,46] New interest in this topic has led to the measurement of the temperature dependence of sputtering on single crystal faces.[63-65] This interest is in part generated by the differing signs of the temperature dependence predicted

105

by various theoretical models proposed for sputtering.[61,66] For example, in the Silsbee chain mechanism the annealing of defects with increased temperature should lengthen the chains and increase the sputtering rate. Conversely, in the bombardment ion channeling mechanism, the primary effect of thermal annealing is the removal of interstitials in low index channels, thus reducing the sputtering rate by increasing the probability of ion penetration. The results of the FEM study performed here suggest another possibility. Since the surface roughness due to sputtering is reduced by annealing at higher temperatures, the probability of multistep sputtering is also reduced, thus reducing the overall sputtering rate.

## Conclusions

The following are the major conclusions reached during these studies:

(1) Sputtering in many instances is a multistep process.

(2) For low-energy, light ion bombardment, the number of surface rearrangement events is much larger than the number of atom removal events.

(3) The Silsbee energy chain concept is important in explaining the forward sputtering of thin targets.

(4) The dependence of sputtering upon crystallographic structure of the target decreases with increasing ion energy.

(5) The amount of energy transferred from the bombardment ions to the target atoms depends upon their relative masses.

(6) Increasing target temperature anneals some of the surface damage and reduces the probability of multistep sputtering.

# REFERENCES

1.  L. W. Swanson, et al. , Final Report for NASA Contract NASw-458 (Field Emission Corporation, 1963).

2.  L. W. Swanson, et al. , NASA CR-54106 (Field Emission Corporation, 1964).

3.  C. J. Bennette, et al. , NASA CR-54704 (Field Emission Corporation, 1965).

4.  R. W. Strayer, et al. , Final Report for NASA Contract NAS4-19 (Linfield Research Institute, 1962).

5.  A. Taylor and B. J. Kagle, Crystallographic Data on Metal and Alloy Structures (Dover Publications, New York, 1963).

6.  J. B. Taylor and I. Langmuir, Phys. Rev. **44**, 423 (1933).

7.  H. Shelton, Phys. Rev. **107**, 1553 (1957).

8.  L. D. Schmidt and R. Gomer, J. Chem. Phys. **43**, 2055 (1965).

9.  D. Lichtman, R. McQuistan, and T. Kirst, Surf. Sci. **5**, 120 (1966).

10. P. A. Redhead, Can. J. Phys. **42**, 886 (1964).

11. D. Menzel and R. Gomer, J. Chem. Phys. **41**, 3311 (1964).

12. R. E. Weber and L. F. Cordes, Proceedings of the 25th Annual Conference on Physical Electronics (Massachusetts Institute of Technology, Cambridge, Mass. , 1965) p. 378.

13. J. C. Riviere, Proc. Phys. Soc. **70B** , 676 (1957).

14. A. A. Holscher, Surf. Sci. **4**, 89 (1966).

15. R. Wortman, R. Gomer, and R. Lundy, J. Chem. Phys. **27**, 1099 (1957).

16. T. H. George and P. M. Stier, J. Chem. Phys. **37**, 1935 (1962).

17. E. E. Huber, Jr. and C. T. Kirk, Jr. , Surf. Sci. **5**, 447 (1966).

18. E. G. Brock, Phys. Rev. **100**, 1619 (1955).

19. V. S. Fomenko, Handbook of Thermionic Properties (Plenum Press Data Div. , New York, 1966).

20. P. J. Estrup, J. Anderson, and W. E. Danforth, Surf. Sci. **4**, 286 (1966).

21. L. W. Swanson and R. W. Strayer (to be published).

22. H. S. Carslaw and J. C. Jaeger, Conduction of Heat in Solids, second ed. (Clarendon Press, Oxford, 1959) p. 200.

23. A. Wehnelt, Ann. Phys. **14**, 425 (1964).

24. J. Langmuir, Phys. Rev. **2**, 11 (1913)

25.  D. E. Anderson, Advances in Electron Tube Techniques - 5th National Conference (Pergamon Press, 1961). Vol. 1, p. 84.

26.  W. G. Rudy, Advances in Electron Tube Techniques - 5th National Conference (Pergamon Press, 1961) Vol. 1, p. 94.

27.  B. Wolk, W. Watson and R. A. Wallace, Advances in Electron Tube Techniques - 5th National Conference (Pergamon Press, 1961) Vol. 1, p 161.

28.  W. R. Kerslake, NASA TN D-3818 (February, 1967).

29.  D. MacNair, Advances in Electron Tube Techniques - 6th National Conference (Pergamon Press, 1962) Vol. 2, p. 211.

30.  S. Garbe, 2nd International Symposium on Residual Gases in Electron Tubes 1, 810 (1963).

31.  A. Sandor, Intern. J. Electron. (1) 18, 349 (1965).

32.  W. B. Nottingham, Handbuch der Physik, ed. by S. Flugge (Springer-Verlag, Berlin, 1956) Vol. 21, p. 1.

33.  J. V. Florio, Advances in Electron Tube Techniques - 6th National Conference (Pergamon Press, 1962) Vol. 2, p. 241.

34.  D. Lichtman, J. Vac. Sci. Tech. 2, 70 (1965).

35.  Y. P. Zingerman and V. A. Ishchuk, Soviet Phys. -Solid State 7, 173 (1965).

36.  L. W. Swanson and E. C. Cooper, NIH Quarterly Report No. 3 for Contract PH 43-64-71 (Field Emission Corporation, 1965).

37.  J. M. Sellen, Jr. , Astronautics and Aeronautics, 4, 70 (1966).

38.  H. L. Garvin and R. G. Wilson, AIAA Journal 3, 1867 (1965).

39.  M. Kaminsky, Atomic and Ionic Impact Phenomena on Metal Surfaces (Academic Press, Inc. , New York, 1965) pp. 142-237.

40.  E. B. Henschke, J. Appl. Phys. 28, 411 (1957).

41.  D. E. Harrison, Jr. and G. D. Magnuson, Phys. Rev. 122, 1421 (1961).

42.  E. Langberg, Phys. Rev. 111, 91 (1958).

43.  J. B. Gibson, et al. , Phys. Rev. 120, 1229 (1960).

44.  W. L. Gay and D. E. Harrison, Jr. , Phys. Rev. 135, A1780 (1964).

45.  D. E. Harrison, Jr. , et al. , Appl. Phys. Letters 8, 33 (1966).

46.  E. Kay, Advances in Electronics and Electron Physics (Academic Press, Inc. , New York, 1962) Vol. 17, p. 245.

47.  E. W. Muller, Z. Physik 131, 136 (1951).

48.  E. W. Müller, Advances in Electronics and Electron Physics (Academic Press, Inc. , New York, 1960) Vol. 13, p. 83; also E. W. Müller, Science 149, 591 (1965).

49.  E. W. Müller, Direct Observations of Imperfections in Crystals, ed. by J. B. Newkirk and J. B. Wernick (Interscience Publishers, New York, 1962) p. 77.

50.  R. W. Strayer, et al. , Proceedings of the 25th Annual Conference on Physical Electronics (Massachusetts Institute of Technology, Cambridge, Mass. , 1965) p. 150.

51.  M. K. Sinha and E. W. Müller, J. Appl. Phys. 35, 1256 (1964).

52.  D. G. Brandon and M. K. Wald, Phil. Mag. 6, 1035 (1961).

53.  E. E. Martin, et al. , J. Appl. Phys. 31, 782 (1960).

54.  G. Ehrlich and F. G. Hudda, J. Chem. Phys. 30, 493 (1959).

55.  Mannfred von Ardenne, Tabellen der Elecktronenphysik, Ionenphysik und Ubermikroscopie (Veb Deutscher Verlag der Wissenschaften, Berlin, 1956).

56.  D. Rosenberg and G. K. Wehner, J. Appl. Phys. 33, 1842 (1962).

57.  R. R. Hasiguti, et al. , J. Phys. Soc. Japan 18, Suppl. III, 164 (1963).

58.  E. W. Müller, J. Appl. Phys. 28, 1 (1957).

59.  R. V. Stuart and G. K. Wehner, J. Appl. Phys. 35, 1819 (1964).

60.  G. K. Wehner, J. Appl. Phys. 25, 270 (1954).

61.  R. H. Silsbee, J. Appl. Phys. 28, 1246 (1957).

62.  Chr. Lehmann and P. Sigmund, Phys. Stat. Sol. 16, 507 (1966).

63.  J. B. Green, et al. , J. Appl. Phys. 37, 4699 (1966).

64.  C. E. Carlston, et al. , Phys. Rev. 138, A759 (1965).

65.  G. S. Anderson, J. Appl. Phys. 37, 2838 (1966).

66.  G. Liebfried, J. Appl. Phys. 30, 1388 (1959) ; 31, 117 (1960).

## LIST OF SYMBOLS

| SYMBOL | MEANING | PAGE | EQUATION |
|---|---|---|---|
| $A$ | Pre-exponential in Fowler-Nordheim equation | 8 | 8 |
| $A_i$ | Fowler-Nordheim pre-exponential corresponding to surface before electron bombardment, i. e., when $t = 0$ | 61 | 28 |
| $A_t$ | Fowler-Nordheim pre-exponential corresponding to surface after electron bombardment for a time, t. | 61 | 28 |
| $A_\infty$ | Fowler-Nordheim pre-exponential corresponding to surface after electron bombardment for a time, $t = \infty$. | 61 | 28 |
| $A_s$ | Fowler-Nordheim pre-exponential corresponding to the clean substrate. | 62 | 29 |
| $A_o$ | Pre-exponential constant in Fowler-Nordheim equation. | 61 | 27 |
| $A_R$ | Experimentally determined thermionic emission constant. | 55 | |
| $a_n$ | Positive roots of the Bessel function $J_o(ar_o)$. | 46 | 21 |
| $B$ | Defined as the logarithm of the ratio $A_s/A$. | 62 | |
| $B_i$ | Value of B when $t = 0$. | 62 | 29 |
| $B_t$ | Value of B at time t. | 62 | 29 |
| $B_\infty$ | Value of B at time $t = \infty$. | 62 | 29 |
| $b_j$ | Cross section for electron induced desorption. | 60 | 23 |
| $C$ | Pre-exponential term in Richardson equation. | 9 | 11 |

110

111

| SYMBOL | MEANING | PAGE | EQUATION |
|---|---|---|---|
| $I_o$ | Emission current for smooth surface before sputtering. | 98 | |
| $I_s$ | Emission current from sputtered surface. | 98 | 24 |
| $J$ | Current density. | 61 | 21 |
| $J_o$ | Bessel function of order zero. | 46 | 21 |
| $J_1$ | Bessel function of order one. | 46 | 21 |
| $J_c$ | Collector current density in RPT. | 9 | 11 |
| $J_e$ | Emitter current density in RPT. | 9 | 11 |
| $j$ | State of adsorbed species. | 60 | |
| $k$ | Boltzmann constant. | 6 | 1 |
| $k_1$ | Constant in empirical formula. | 39 | 18 |
| $k_2$ | Constant in empirical formula. | 39 | 18 |
| $M$ | Particle mass. | 7 | 3 |
| $M_a$ | Mass of target atom. | 104 | 30 |
| $M_i$ | Mass of bombarding ion. | 104 | 30 |
| $m$ | Slope of Fowler-Nordheim plot. | 8 | 9 |
| $m_1$ | Slope of Fowler-Nordheim plot for clean surface. | 9 | 10 |
| $N_e$ | Number of electrons. | 60 | 23 |
| $N_j$ | Number of species in state j. | 61 | 25 |
| $N_p$ | Number of ions. | 102 | |
| $P$ | Pressure | 6 | 1 |

LIST OF SYMBOLS (Cont'd)

| SYMBOL | MEANING | PAGE | EQUATION |
|---|---|---|---|
| RPT | Retarding potential triode. | | |
| r | Radial direction. | 46 | 20 |
| $r_o$ | Radius of crystal. | 46 | 21 |
| T | Temperature. | 6 | 1 |
| $T_d$ | Desorption temperature. | 47 | |
| $T_{eq}$ | Equilibration temperature. | 12 | |
| t | Time. | 7 | 6 |
| V | Voltage. | 8 | 8 |
| $V_b$ | Positive bias voltage on the emitter in the RPT. | 9 | 11 |
| $\alpha$ | Effective adsorbate polarizability. | 36 | 15 |
| $\alpha_s$ | Sticking coefficient. | 7 | 3 |
| $\beta$ | Ratio of electric field to applied voltage. | 8 | 9 |
| $\theta$ | Relative coverage. | 32 | |
| $\theta_m$ | Coverage at minimum work function. | 32 | |
| $\theta_f$ | Final coverage. | 44 | |
| $\mu_o$ | Zero coverage dipole moment. | 36 | 13 |
| $\mu_p$ | Kinetic impingement rate. | 6, 7 | 3 |
| $\nu$ | Pre-exponential term in rate equation. | 7 | 2 |
| $\sigma$ | Surface atom density. | 6 | |
| $\sigma_c$ | Constant surface atom density. | 46 | 21 |

| SYMBOL | MEANING | PAGE | EQUATION |
|---|---|---|---|
| $\sigma_f$ | Final surface atom density. | 7 | 6 |
| $\sigma_i$ | Initial surface atom density. | 7 | 6 |
| $\sigma_j$ | Surface atom density of species j. | 60 | 23 |
| $\sigma_j(0)$ | Surface atom density of species j at t = 0. | 61 | 24 |
| $\sigma_j(t)$ | Surface atom density of species j at time t. | 61 | 24 |
| $\sigma_m$ | Surface atom density at the minimum work function. | 22 | |
| $\sigma_o$ | Surface atom density at coverage where work function change becomes independent of coverage. | 31 | |
| $\sigma_{OW}$ | Underlying oxygen atom density. | 13 | |
| $\Delta\sigma$ | Change in coverage. | 8 | |
| $\emptyset$ | Work function. | 2 | |
| $\emptyset_c$ | Work function of collector in RPT. | 9 | 11 |
| $\emptyset_e$ | Work function of emitter in RPT. | 9 | 11 |
| $\emptyset_{eff}$ | Effective work function corresponding to regions of substrate where desorption is taking place. | 42 | 19 |
| $\emptyset_i$ | Work function at t = 0. | 61 | 26 |
| $\emptyset_m$ | Work function minimum. | 2 | |
| $\emptyset_R$ | Thermionic work function. | 55 | |
| $\emptyset_s$ | Substrate work function. | 25 | |
| $\emptyset_o$ | Work function at $\sigma = \sigma_o$ | 31 | |

LIST OF SYMBOLS (Cont'd)

| SYMBOL | MEANING | PAGE | EQUATION |
|---|---|---|---|
| $\emptyset_t$ | Work function at time t. | 61 | 26 |
| $\emptyset_1$ | Work function of clean substrate. | 9 | 10 |
| $\emptyset_{OW}$ | Work function of oxygenated surface. | 2 | |
| $\emptyset_\infty$ | Work function at $t = \infty$. | 61 | 25 |
| $\Delta\emptyset$ | Change in work function. | 6 | |
| $\Delta\emptyset_m$ | Maximum work function change on adsorption. | 2 | |

REPORT DISTRIBUTION LIST FOR
CONTRACT NO. NAS3-8900


National Aeronautics and Space Administration
Washington, D. C. 20546
Attn: RNT/James Lazar                                                                    (1)


National Aeronautics and Space Administration
Washington, D. C. 20546
Attn: RRM/Ralph R. Nash                                                                  (1)


NASA-Lewis Research Center
21000 Brookpark Road
Cleveland, Ohio 44135
Attn: Spacecraft Technology Procurement
      Section (M.S. 54-2)                                                                (1)


NASA-Lewis Research Center
21000 Brookpark Road
Cleveland, Ohio 44135
Attn: Technology Utilization Office
      (M.S. 3-19)                                                                        (1)


NASA-Lewis Research Center
21000 Brookpark Road
Cleveland, Ohio 44135
Attn: Technical Information Division
      (M.S. 5-5)                                                                         (1)


NASA-Lewis Research Center
21000 Brookpark Road
Cleveland, Ohio 44135
Attn: Library
      (M.S. 60-3)                                                                        (2)


NASA-Lewis Research Center
21000 Brookpark Road
Cleveland, Ohio 44135
Attn: Spacecraft Technology Division
      C. C. Conger (M.S. 54-3)                                                           (1)

NASA-Lewis Research Center
21000 Brookpark Road
Cleveland, Ohio 44135
Attn: Spacecraft Technology Division
     R. R. Nicholls (M.S. 54-3)           (6)

NASA-Lewis Research Center
21000 Brookpark Road
Cleveland, Ohio 44135
Attn: H. R. Hunczak (M.S. 54-3)           (1)

NASA-Lewis Research Center
21000 Brookpark Road
Cleveland, Ohio 44135
Attn: Spacecraft Technology Division
     T. Riley (M.S. 54-3)           (1)

NASA-Lewis Research Center
21000 Brookpark Road
Cleveland, Ohio 44135
Attn: R. M. Williams
     Space Power Systems Division
     (M.S. 500-309)           (1)

NASA-Lewis Research Center
21000 Brookpark Road
Cleveland, Ohio 44135
Attn: Electric Propulsion Laboratory
     W. Moeckel (M.S. 301-1)           (1)

NASA-Lewis Research Center
21000 Brookpark Road
Cleveland, Ohio 44135
Attn: Electric Propulsion Laboratory
     H. R. Kaufman (M.S. 301-1)           (1)

NASA-Lewis Research Center
21000 Brookpark Road
Cleveland, Ohio 44135
Attn: Electric Propulsion Laboratory
     John R. Smith (M.S. 302-1)           (1)

NASA-Lewis Research Center
21000 Brookpark Road
Cleveland, Ohio 44135
Attn: Electric Propulsion Laboratory
     John Ferrante (M. S. 302-1)                      (2)

NASA-Lewis Research Center
21000 Brookpark Road
Cleveland, Ohio 44135
Attn: Electric Propulsion Laboratory
     R. Breitwieser (M. S. 302-1)              (1)

NASA-Lewis Research Center
21000 Brookpark Road
Cleveland, Ohio 44135
Attn: Electric Propulsion Laboratory
     W. Rayle (M.S. 301-1)                   (1)

NASA-Lewis Research Center
21000 Brookpark Road
Cleveland, Ohio 44135
Attn: Electric Propulsion Laboratory
     E. Richley (M. S. 301-1)                (1)

NASA-Lewis Research Center
21000 Brookpark Road
Cleveland, Ohio 44135
Attn: Electric Propulsion Laboratory
     L. Tower (M. S. 302-1)                 (1)

NASA-Lewis Research Center
21000 Brookpark Road
Cleveland, Ohio 44135
Attn: Report Control Office
     (M.S. 5-5)                          (1)

NASA Scientific and Technical Information Facility
P.O. Box 33
College Park, Maryland 20740
Attn: NASA Representative RQT-2448        (6)

NASA-Marshall Space Flight Center
Huntsville , Alabama 35812
Attn: Ernest Stuhlinger (M-RP-DIR)                          (1)


NASA-Marshall Space Flight Center
Hutsville, Alabama 35812
Attn: I. Dalins                                            (1)


Research and Technology Division
Wright-Patterson AFB, Ohio 45433
Attn: AFAPL (APIE-2)
      R. F. Cooper                                         (1)


AFWL
  Kirtland AFB, New Mexico 87417
  Attn: WLPC/Capt. C. F. Ellis                             (1)


Aerospace Corporation
P.O. Box 95085
Los Angeles, California 90045
Attn: Library/Technical Documents Group                    (1)


Jet Propulsion Laboratory
4800 Oak Grove Drive
Pasadena, California 91103
Attn: J. W. Stearns                                        (1)


Hughes Research Laboratories
3011 Malibu Canyon Road
Malibu, California 90265
Attn: R. C. Knechtli                                       (1)


Electro-Optical Systems, Inc.
300 North Halstead
Pasadena, California 91107
Attn: R. C. Speiser                                        (1)


Westinghouse Astronuclear Laboratories
Electric Propulsion Laboratory
Pittsburgh, Pennsylvania 15234                             (1)

TAPCO, A Division of TRW Inc.
New Product Research
23555 Euclid Avenue
Cleveland, Ohio 44117
Attn: R. T. Craig                                          (1)

General Electric Company
Space Flight Propulsion Laboratory
Cincinnati, Ohio 45215
Attn: M. L. Bromberg                                       (1)

Hiram College
Department of Physics
Hiram, Ohio 44234
Attn: Professor L. Shaffer                                 (1)

General Dynamics/Convair
P.O. Box 1128
San Diego, California 92101
Attn: G. D. Magnuson                                       (1)

New England Materials Laboratory, Inc.
35 Commercial Street
Medford, Massachusetts 02155
Attn: Allan S. Bufferd                                     (1)

Varian Associates
611 Hansen Way
Palo Alto, California 94304
Attn: Yale E. Strausser                                    (1)

Varian Associates
611 Hansen Way
Palo Alto, California 94304
Attn: Technical Library                                    (1)

NASA-Ames Research Center
Moffett Field, California 94035
Attn: Library                                              (1)

Astro Met Associates, Inc.
500 Glendale-Milford Road
Cincinnati, Ohio 45215
Attn: J. W. Graham                                         (1)

United Aircraft Corporation
Research Laboratories
East Hartford, Connecticut 06108
Attn:  R.  G.  Meyerand,  Jr.                                              (1)

NASA-Langley Research Center
Langley Field Station
Hampton, Virginia 23365
Attn:  Technical Library                                                   (1)

Colorado State University
Fort Collins, Colorado 80521
Attn:  L.  Baldwin                                                         (1)

Colorado State University
Fort Collins, Colorado 80521
Attn:  W.  Mickelsen                                                       (1)

NASA Goddard Space Flight Center
Greenbelt, Maryland 20771
Attn:  Library                                                            (1)

United States Air Force
Office of Scientific Research
Washington, D. C. 20025
Attn:  M.  Slawsky                                                         (1)

Case Institute of Technology
10900 Euclid Avenue
Cleveland, Ohio 44106
Attn:  Eli Reshotko                                                       (1)

Metals Reaction Section
Metallurgy Division
National Bureau of Standards
Washington, D. C. 20546
Attn:  W. J.  Ambs                                                         (1)

University of Pennsylvania
Philadelphia, Pennsylvania
Attn:  Dr.  Michael Kaplit                                                 (1)

National Bureau of Standards
Washington, D. C. 20546
Attn: Dr. T. Madey                                                    (1)

National Bureau of Standards
Washington, D. C. 20546
Attn: Dr. R. Young                                                    (1)

Naval Ordinance Test Station
China Lake, California
Attn: Dr. E. Bauer                                                    (1)

Niagara University
Niagara Falls, New York 14109
Attn: Prof. William L. Boeck
      Asst. Professor of Physics                                      (1)

Yale University
Josiah Willard Gibbs Research labs.
Department of Biophysics
New Haven, Connecticut
Attn: Dr. H. Pollock                                                  (1)

Applied Science Division of Litton Ind.
2003 Hannegin Avenue
Minneapolis, Minnesota 55413
Attn: G. K. Werner                                                    (1)

University of Missouri
Materials Research Center
Rolla, Missouri
Attn: James R. Wolfe                                                  (1)

National Inst. for Research in Nuclear Science
Rutherford High Energy Laboratory
Chilton, Didcot, Berks.
Great Britain
Attn: P. A. Chatterton                                                (1)

Institute for Plasma Physics
8046 Garching
Munich, Germany
Attn: Dr. L. Johannsen                                                (1)

National Research Corporation
70 Memorial Dr.
Cambridge, Massachusetts 02142
Attn:  Dr.  Robert M.  Ohman                                    (1)